DESIGN OF AN IMPROVED MICROSTRIP ANTENNA FOR MIMO RADAR

CONCEPTION D'UNE ANTENNE MICRORUBAN AMÉLIORÉE POUR RADAR MIMO

A Thesis Submitted to the Division of Graduate Studies
of the Royal Military College of Canada
by

Caroline Archambault
Major

In Partial Fulfillment of the Requirements for the Degree of
Master of Applied Science in Electrical Engineering

October, 2026

© This thesis may be used within the Department of National Defence
but copyright for open publication remains the property of the author.

Acknowledgements

This thesis was made possible with the support and guidance of my supervisors, Dr. Yahia Antar and Dr. Bray. Their knowledge of antennas, beamforming, and MIMO radar provided the background necessary to conduct this research. Dr. Joey Bray provided knowledge and guidance on using the anechoic chamber. I want to thank Mr. Pier Drouin, a member of the Electrical and Computer Engineering Department Technical Support Staff, for his invaluable contribution to the fabrication of the antennas presented in this thesis.

Abstract

Multiple-Input Multiple-Output (MIMO) radar systems employ multiple transmit (TX) and receive (RX) antennas to enhance spatial resolution, target detection, and signal-to-noise ratio, while enabling wide-area coverage with a limited number of pulses. However, the overall performance of such systems is often constrained by the characteristics of the antenna elements, including their bandwidth, radiation pattern, polarization purity, and mutual coupling. This is particularly critical in sub-6 GHz MIMO radar applications, where lower carrier frequencies inherently limit operational bandwidth and impose physical integration challenges.

This thesis describes the design, improvement, and experimental validation of microstrip antenna elements developed for the Royal Military College of Canada's (RMC) monostatic MIMO radar platform. The work begins with a review of recent advances in microstrip antenna and array design, focusing on microstrip antenna characteristics such as impedance bandwidth, radiation patterns, and mutual coupling. A review of microstrip antenna and feed-network designs was conducted to identify suitable configurations for the radar system. Based on their potential to satisfy the radar requirements, a circular patch antenna and a proximity-coupled, series-fed subarray were selected as the foundation for the design.

A proximity-coupled series-fed circular patch was designed for used in the TX subarray and improved using full-wave electromagnetic simulations to meet the radar operational requirements within the $5.25 - 5.925$ GHz radar frequency band and a 200 MHz bandwidth BW, including broad azimuth coverage and a narrow elevation beamwidth. The simulated subarray achieved a frequency of 5.75 GHz, a 180 MHz BW, a peak gain of 9.2 dBi in the E-plane and 9.6 dBi in the H-plane, with measured half-power beamwidths $HPBWs$ of approximately 67.4° and 40.0°, respectively. Although the achieved bandwidth was slightly below the target requirement, it resulted in a small decrease in range resolution.

The antenna satisfied the desired radiation characteristics for the intended

radar application. Therefore, three improved subarrays were fabricated and experimentally characterized, and the measured results agreed well with the simulations. The best fabricated antenna achieved a measured frequency range of $5.66 - 5.875$ GHz, corresponding to an impedance bandwidth of 215 MHz, with a resonance frequency of 5.736 GHz. The antenna achieved a peak gain of 9.2 dBi in the E-plane and 9.6 dBi in the H-plane, with measured $HPBWs$ of approximately 50.9° and 33.6°, respectively. The measured radiation patterns exhibited broad azimuthal coverage and a narrower elevation response, with no distinct sidelobes identified in either plane.

The improved subarray was subsequently integrated into an eight-subarray, forming the two-dimensional (2D) planar array RX antenna. The resulting array achieving resonant frequencies between 5.719 and 5.728 GHz, impedance bandwidths between 164 and 189 MHz, adjacent-element mutual coupling below -18 dB, peak gains of at least 17.8 dBi, and front-to-back ratios greater than 26 dB. While the impedance bandwidth remained below the 200 MHz target, the array achieved the required frequency, mutual-coupling, and radiation-performance characteristics, making it suitable for sub-6 GHz MIMO radar applications.

Résumé

Les systèmes radar à entrées multiples et sorties multiples (MIMO) utilisent plusieurs antennes d'émission (TX) et de réception (RX) pour améliorer la résolution spatiale, la détection des cibles et le rapport signal/bruit, tout en permettant une couverture étendue avec un nombre limité d'impulsions. Cependant, les performances globales de ces systèmes sont souvent limitées par les caractéristiques des éléments d'antenne, notamment leur bande passante, leur diagramme de rayonnement, leur pureté de polarisation et leur couplage mutuel. C'est particulièrement critique dans les applications radar MIMO inférieures à 6 GHz, où les fréquences porteuses plus basses limitent intrinsèquement la bande passante en impédance et posent des défis d'intégration physique.

Cette thèse valide la conception, l'amélioration et la validation expérimentale d'éléments d'antenne à microruban adaptés à la plateforme radar MIMO monostatique du Collège militaire royal du Canada (CMR). Le travail commence par une revue des avancées récentes en matière de conception d'antennes à microruban et de réseaux d'antennes, en mettant l'accent sur leurs caractéristiques, notamment la bande passante en impédance, les diagrammes de rayonnement et le couplage mutuel. Une analyse des conceptions d'antennes à microruban et de réseaux d'alimentation a été menée afin d'identifier les configurations adaptées au système radar proposé. Compte tenu de leur capacité à répondre aux exigences du radar, une antenne microruban circulaire et un sous-réseau à couplage de proximité et à alimentation en série ont été choisis comme base de la conception.

Une antenne microruban circulaire à alimentation en série et à couplage de proximité a été conçue pour être utilisée dans le sous-réseau émetteur (TX) et améliorée à l'aide de simulations électromagnétiques en onde complète afin de répondre aux exigences opérationnelles du radar dans la bande de fréquences $5.25 - 5.925$ GHz et avec une largeur de bande de 200 MHz, notamment une large couverture azimutale et une largeur de faisceau étroite en élévation. Le sous-réseau simulé a atteint une fréquence de 5,75 GHz, une largeur de bande de 180 MHz, un gain maximal de 9.2 dBi dans le plan E et de 9.6

dBi dans le plan H, avec des largeurs de faisceau à demi-puissance ($HPBWs$) mesurées d'environ 67.4° et 40.0°, respectivement. Bien que la largeur de bande obtenue ait été légèrement inférieure à l'exigence cible de 200 MHz, l'antenne répondait aux caractéristiques de rayonnement souhaitées pour l'application radar prévue. Par conséquent, trois sous-réseaux améliorés ont été fabriqués et caractérisés expérimentalement, et les résultats mesurés concordaient bien avec les simulations. La meilleure antenne fabriquée a atteint une plage de fréquences mesurée de $5.66 - 5.875$ GHz, correspondant à une largeur de bande d'impédance de 215 MHz, avec une fréquence de résonance de 5.736 GHz. L'antenne a atteint un gain maximal de 9.2 dBi dans le plan E et de 9.6 dBi dans le plan H, avec des $HPBWs$ mesurées d'environ 50.9° et 33.6°, respectivement. Les diagrammes de rayonnement mesurés présentaient une large couverture azimutale et une réponse en élévation plus étroite, sans lobes latéraux distincts identifiés dans aucun des deux plans.

L'antenne sous-réseau améliorée a ensuite été intégrée à un ensemble de huit sous-réseaux, formant ainsi l'antenne réceptrice à réseau plan bidimensionnel. L'antenne présente des fréquences de résonance comprises entre 5.719 et 5.728 GHz, des largeurs de bande d'impédance comprises entre 164 et 189 MHz, un couplage mutuel entre éléments adjacents inférieur à -18 dB, des gains maximaux d'au moins 17.8 dBi et des rapports avant-arrière supérieurs à 26 dB. Bien que la bande passante d'impédance soit restée inférieure à la valeur cible de 200 MHz, le réseau a atteint les caractéristiques requises en matière de fréquence, de couplage mutuel et de rayonnement, ce qui le rend adapté aux applications de radar MIMO dans la bande inférieure à 6 GHz.

Contents

Acknowledgements **ii**

Abstract **iii**

Résumé **v**

List of Tables **x**

List of Figures **xi**

1 Introduction **1**
1.1 Motivation 1
1.2 Statement of Deficiency 2
1.3 Thesis Statement 3
1.4 Methodology 3
1.5 Contributions 4
1.6 Organization 4

2 Literature Survey **6**
2.1 Microstrip Patch Antenna Characteristics 7
2.1.1 Input Reflection Coefficients 7
2.1.2 Impedance Bandwidth 9
2.1.3 Antenna Radiation Efficiency 9
2.1.4 Radiation Pattern 9
2.1.5 Beamwidth and Half-Power Beamwidth 11
2.1.6 Front-to-Back Ratio 12
2.1.7 Antenna Physical Size 12
2.1.8 Antenna Element Spacing and Mutual Coupling on a Microstrip Array 12
2.2 Feeding Method and Network 13

2.3 Antenna Array Theory 15
2.4 Phased Array and MIMO Radar Theory 17
2.5 MIMO Radar and Antennas Specifications 19
2.6 Antenna Design Requirements 22
2.6.1 Defining the Design Specifications 22
2.6.1.1 Selecting the Antenna Frequencies 23
2.6.1.2 Defining the Radiation Pattern of the TX Antenna 25
2.6.1.3 Antenna Spacing in MIMO Virtual Array . . . 26
2.6.2 Survey of Microstrip Patch Antennas from the Literature 28
2.6.2.1 Circular MPA with fan-shaped cells 29
2.6.2.2 Circular MPA with directional pattern 31
2.6.2.3 Rectangular versus Circular MPA 31
2.6.2.4 Comparison of the Antenna Designs 34
2.6.3 Survey of Array Network Design from the Literature . . 35
2.6.3.1 Series-Feed Array Network Design 36
2.6.3.2 Series-Feed Array Network Design with Matching-in-Step 38
2.6.3.3 Series-Feed Array Network with Coupling Branches Design 39
2.6.3.4 Comb-line Array Antenna 40
2.6.3.5 Corporate Feed Array Network 42
2.6.3.6 Comparison of the Feed Network Designs . . . 45

3 Proximity-Coupled Series-Fed Circular Patch Subarray Antenna 48
3.1 Subarray Antenna Geometry and Dimensions 48
3.2 Substrates 49
3.3 Circular Patch 52
3.4 Series-Fed Array Topology and Design 53
3.5 Overall Subarray Tuning Steps 55
3.6 Antenna Simulation Result and Discussion 58
3.7 Comparison of the subarray with the Taoglas antenna 61

4 2D Planar Array Antenna 64
4.1 Planar Antenna Geometry and Dimensions 64
4.2 4-Subarray Antenna Tuning Steps 66
4.3 Simulated Result of the 8-Subarray Planar Antenna 68

5 Experimental results 73

5.1 Fabrication Procedure 73
5.2 Experimental Set-up 76
5.3 Measurement Results and Discussion 77

6 Conclusion **84**

Bibliography **88**

Appendices **93**

A Matlab Code for Virtual Array Beam Pattern and HPBW Calculation **94**

List of Tables

2.1 Taoglas UWB FXUWB20 specifications 20
2.2 TX and RX Antennas performance targets for the MIMO radar application 24
2.3 Aperture sizes for different frequencies and beamwidths 27
2.4 Comparison of spacing configurations for an 8×8 MIMO linear array 27
2.5 Comparison of Antenna Designs 35
2.6 Comparison of candidate feed-network architectures for the TX subarray 45

3.1 Final antenna dimensions 51
3.2 Normalized excitation coefficients for a 3-element array at different sidelobe ratios 56
3.3 Comparison of simulated $|S_{11}|$ with design requirements 59
3.4 Comparison of simulated radiation pattern parameters with design requirements 61
3.5 Comparison between the existing Taoglas FXUWB20 antenna and the improved subarray antenna 62

4.1 Array planar antenna dimensions 65
4.2 Comparison of simulated $|S_{11}|$ for all subarrays of the planar antenna with the design spec and the simulated subarray 69
4.3 Comparison of simulated mutual coupling of each subarrays of the planar antenna 70
4.4 Comparison of the simulated radiation pattern parameters of the 8-subarray planar array antenna with the design specifications . . 72

5.1 Comparison of simulated, measured antennas and design requirements 79
5.2 Comparison of the design specifications, simulated results, and measured radiation characteristics of the fabricated antennas. . . . 83

6.1 Comparison of the Subarray with Antenna Designs from the literature 87

List of Figures

1.1 Rectangular MPA [5] 2

2.1 Representative shapes of microstrip patch elements [2] 7
2.2 $|S_{11}|$ responses versus frequency plot, adapted from [9] 8
2.3 An omnidirectional pattern (dBi) 10
2.4 Radiation pattern with back radiation sidelobes (dBi) [9] 11
2.5 Inter-element spacing on a microstrip array, adapted from [13] . . 13
2.6 Patch antenna feeding methods: (a) line feed, (b) probe-feed, (c) aperture-coupling, and (d) proximity-coupling [5] 14
2.7 Feed arrangements for microstrip patch arrays [5] 15
2.8 N-element linear array [5] 16
2.9 $M \times N$ planar array [5] 17
2.10 MIMO radar virtual array [15] 19
2.11 Taoglas Antenna $|S_{11}|$ measurement using the network analyzer [6] 21
2.12 Taoglas Antenna Radiation patterns at 3, 4 and 5 GHz: (a) the E-plane and (b) H-plane 21
2.13 Taoglas Antenna 3D radiation pattern [7] 22
2.14 Conceptual ideal radiation pattern with 180° azimuth and 30° elevation 26
2.15 Beam pattern for both configuration 28
2.16 Geometry of the circular patch with fan-shaped coupling patches antenna: (a) top, (b) side view [19] 29
2.17 $|S_{11}|$ of circular MPA with fan-shaped cells [19] 30
2.18 Pattern of Circular MPA at 3.5 GHz [19] 30
2.19 Geometry of the circular antenna [20] 31
2.20 $|S_{11}|$ of the circular patch 32
2.21 Radiation patterns of the circular patch 32
2.22 MPA (a) rectangular (b) circular 33
2.23 $|S_{11}|$of (a) rectangular MPA (b) circular MPA [21] 33
2.24 Radiation pattern of (a) rectangular MPA (b) circular MPA [21] . 34

2.25 1×5 linear array [23] 36
2.26 Simulated result of the 1×5 (a) reflection coefficient, (b) radiation pattern [23] 37
2.27 4×5 planar array configuration 37
2.28 Comb-Line matching-in-step design [25] 38
2.29 Comb-line matching-in-step design radiation pattern (a) E-plane (b) H-plane 39
2.30 $|S_{11}|$ simulated versus measured 39
2.31 (a) Geometry of the series-fed network (b) side view [14] 40
2.32 Tapered comb-line Array [26] 41
2.33 Comb-line Array with tapered feed line [26] 41
2.34 $|S_{11}|$ of the comb-line Array with tapered feed line 42
2.35 Radiation patterns of the comb-line Array with tapered feed line . 42
2.36 Antennas geometry [29] 43
2.37 Radiation pattern at 10 GHz [29] 44

3.1 TX antenna model exploded view 49
3.2 Antenna dimensions (a) top patches layer (b) feed network layer . 50
3.3 Effect of substrate thickness and dielectric constant on the impedance bandwidth ($VSWR < 2$) and radiation efficiency [30] 52
3.4 Series-fed with coupling branches 54
3.5 Array factor for 3-elements with different major-to-minor sidelobe ratio 56
3.6 Feed network and patch alignment 57
3.7 Simulated $|S_{11}|$ of the TX antenna 59
3.8 Simulated co-polarization of the TX antenna 60

4.1 8-array planar network feed layer 65
4.2 4-subarray planar array top layer 66
4.3 Planar array transparency 67
4.4 Input reflection coefficients 68
4.5 Simulated mutual coupling of each subarray of the planar antenna 70
4.6 Polar radiation pattern of the 8-subarray planar array antenna . . 71
4.7 Cartesian radiation pattern of the 8-subarray planar array antenna 72

5.1 Fabricated subarrays 74
5.2 Milling issues during fabrication 74
5.3 Bonding issues during fabrication 75
5.4 AUT and source positioners' coordinates 77
5.5 Simulated and measured $|S_{11}|$ of the subarrays 78

5.6 Measured co-polarization of antenna 1 79
5.7 Measured co-polarization of antenna 2 80
5.8 Simulated vs Measured co-polarization E-plane 81
5.9 Simulated vs Measured co-polarization H-plane 82

List of Acronyms

AF	Array Factor.
AUT	Antenna Under Test.
BW	Bandwidth.
CDM	Code Division Multiplexing.
CMR	Collège militaire royal du Canada.
dB	Decibel.
dBi	Decibels Isotropic.
FBW	Fractional Bandwidth.
F/B	Front-to-Back Ratio.
HFSS	High Frequency Structure Simulator.
HPBW	Half-Power Beamwidth.
IEEE	Institute of Electrical and Electronics Engineers.
MIMO	Multiple-Input Multiple-Output.
MPA	Microstrip Patch Antenna.
NR	Not Reported.
PCB	Printed Circuit Board.
PNA	Performance Network Analyzer.
PTFE	Polytetrafluoroethylene.
QWT	Quarter-Wave Transformer.
RF	Radio Frequency.
RMC	Royal Military College of Canada.
RX	Receiver.
SDR	Software-Defined Radio.
SGH	Standard Gain Horn.
SLL	Sidelobe Level.
SMA	SubMiniature version A.
S-parameters	Scattering Parameters.
TX	Transmitter.

2D	Two-Dimensional.
ULA	Uniform Linear Array.
URA	Uniform Rectangular Array.
UWB	Ultra-Wideband.
VSWR	Voltage Standing Wave Ratio.
ϵ_r	Relative Permittivity.
f_0	Operating Frequency.
λ_0	Wavelength in Free Space.
λ_g	Guided Wavelength.
$\tan\delta$	Loss Tangent.
Z_0	Characteristic Impedance.
Z_{in}	Input Impedance.

1 Introduction

A multiple-input multiple-output (MIMO) radar employs multiple transmitting and receiving antennas arranged in specific array configurations to improve radar performance through spatial diversity and virtual array processing. The characteristics of the antenna elements, including radiation pattern, polarization, impedance bandwidth, efficiency, and inter-element coupling, fundamentally influence the overall system performance. In particular, the antenna bandwidth directly determines the achievable range resolution, whereas the radiation characteristics of the antenna array, including beamwidth, gain, and sidelobe levels, govern angular resolution and clutter rejection performance [1]. Furthermore, mutual coupling between array elements can modify the excitation distribution and distort the radiation pattern, potentially reducing the ability to discriminate between closely spaced targets.

Microstrip patch antennas (MPA), shown in Fig. 1.1, are widely used in wireless communications due to their lightweight and low-cost planar structure and ease of integration with printed circuit board (PCB) technology [2–4]. However, these antennas often exhibit narrow bandwidth and low gain, which can limit a traditional radar system's capabilities, particularly in sub-6 GHz applications where bandwidth is constrained by lower carrier frequencies [2, 5].

To overcome these limitations, significant research has focused on wideband and multiband microstrip antenna designs for communication systems. Various techniques have been proposed to enhance bandwidth, reduce size, improve impedance matching, reduce mutual coupling, and improve array performance.

1.1 Motivation

This thesis aims to design a transmit (TX) subarray antenna with a directional radiation pattern, operating at sub-6 GHz frequencies with a 200 MHz bandwidth, to enhance MIMO radar performance. This subarray antenna will then be used to design a receive (RX) planar antenna array. This radar was first

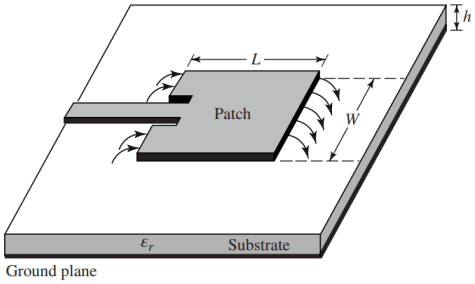


Figure 1.1: Rectangular MPA [5]

developed in 2021 and is used in the laboratory of the Royal Military College of Canada (RMC) [6]. The university's MIMO radar platform comprises software-defined radio (SDR) front ends with eight transmit and eight receive channels operating in the sub-6 GHz band. For laboratory experiments requiring a directional radiation pattern with a specified beamwidth, low sidelobe levels, and suppressed back radiation, antenna elements specifically designed to meet the radar platform's requirements are essential. These elements facilitate accurate radar calibration, improve the quality of the measured radar data, and support advanced processing techniques. This thesis aims to replace the ultra-wideband (UWB) elements originally purchased to enable basic radar operation. They currently introduce severe clutter because their omnidirectional radiation pattern radiates backward and toward the ground.

Developing a custom antenna design provides an opportunity to align the array's electromagnetic characteristics with the radar's signal-processing and requirements of the MIMO radar system. In particular, designing a compact antenna element with a 200 MHz bandwidth, a directional radiation pattern, and controlled mutual coupling across the operational frequencies would significantly enhance system performance.

1.2 Statement of Deficiency

The current laboratory MIMO radar system uses the Taoglas AccuraUWB FXUWB20, a commercially available antenna developed for short-range UWB communication systems. The Taoglas antennas are ultra-wideband (UWB) omnidirectional elements [7], offering wide impedance bandwidths of $3.1 - 5.0$ GHz $6.0 - 8.2$ GHz and $8.2 - 10.3$ GHz, high efficiency of ($\geq 75\%$), and peak gains of $4 - 5$ dBi, in a compact, ground-plane-independent form factor. While

these characteristics are advantageous for consumer communication devices, they do not meet the specific requirements of the RMC MIMO radar.

Collectively, these limitations indicate that the existing antenna system is not well matched to the radar's operational requirements. A purpose-designed antenna element with a directional radiation pattern and constrained bandwidth is therefore required to achieve the desired performance radiation characteristics, polarization, and mutual coupling, thereby enabling accurate and repeatable MIMO radar measurements in a laboratory environment.

1.3 Thesis Statement

A microstrip antenna array can be designed, fabricated, and tested to improve the radiation performance of a MIMO radar. The antenna element will provide a wide azimuthal and narrow elevation beamwidth with minimal back radiation, a linear polarization, while maintaining stable impedance across a constrained sub-6 GHz bandwidth. The desired performance will be achieved by balancing directional radiation characteristics, specific bandwidth requirements, and compact geometry, while accounting for the radar system's specified constraints.

1.4 Methodology

The antenna design methodology follows a structured process that progresses from requirements definition to experimental validation and system integration. Initially, the theoretical principles underlying microstrip patch antennas and antenna arrays for MIMO radar applications were investigated. Then, the antenna specifications were established based on the radar system's operating frequencies, the bandwidth limitations of the software-defined radio (SDR) platform, the desired array configuration, and practical laboratory constraints. A literature review was then conducted to identify suitable antenna element designs and array feed network architectures. For the antenna elements, designs exhibiting characteristics relevant to the radar application, including directional radiation patterns, compact size and narrowband performance, were examined. For the array feed networks, architectures that consider compactness, low implementation complexity, and fabrication simplicity requirements were considered. Following the selection of an antenna element design and an array feed network architecture, parametric studies and full-wave electromagnetic simulations were conducted. The antenna was modified and improved to meet the TX antenna's design specifications. This improved TX subarray antenna is subsequently incorporated eight times to form a 2D planar RX array The array

was simulated to evaluate its mutual coupling, radiation characteristics, and inter-element spacing requirements. The subarray design was then fabricated using available manufacturing processes, and experiments were conducted. The measured results were compared with simulation data to validate the design methodology and quantify performance improvements.

1.5 Contributions

The TX subarray antennas provide the following contributions:

- Improvement of a microstrip antenna design operating at 5.75 GHz. The design jointly satisfies the broad azimuth-beam, narrower elevation-beam radiation pattern and narrowband operating requirements, together with the physical spacing limitations imposed by the MIMO radar array architecture.
- Development of an improved series-fed network incorporating proximity-coupled branches, designed to distribute power and to achieve the desired excitation taper among the array patches.
- Implementation of a compact subarray at 5.75 GHz that can be integrated into a $1 \times N$ configuration to form a two-dimensional planar array, with an inter-subarray spacing of $\lambda/2 = 26.1$ mm.

1.6 Organization

This thesis is organized into six chapters, including this introduction chapter. Chapter 2 provides a comprehensive review of the relevant literature on microstrip antenna fundamentals, focusing on key antenna parameters, array theory, and MIMO radar concepts. It also establishes the antenna design requirements, based on the specifications of the RMC MIMO radar platform and current antenna specifications, thereby establishing the operational context and performance targets. Literature-based antenna and feed network designs are then evaluated against these requirements, and both an antenna and a network feed design configurations were selected as the starting point for further development and tuning steps.

Chapter 3 presents the design and improvement of the TX subarray antenna. Beginning with the selected antenna and network feed configurations, various techniques are applied to achieve the specified design requirements. The simulated electromagnetic performance of the improved subarray is also presented and analyzed with respect to the established design specifications.

Chapter 4 presents the design of the 2D planar antenna. The chapter begins by incorporating the subarray antenna configuration into a 2D planar RX array, followed by parametric studies of the array geometry's relevant design parameters. The resulting simulated antenna performance is then presented and evaluated against the design specifications.

Chapter 5 presents the fabrication process of the TX subarray antennas, measurement procedures, and corresponding measurement results. The measured results are compared with the corresponding simulation results to assess the performance of the fabricated antenna.

Chapter 6 summarizes the research findings and discusses potential directions for future work. The appendix provides supporting MATLAB code and analysis tools used for array simulations and beam pattern calculations discussed in Section 2.6.1.

2 Literature Survey

This chapter reviews the theoretical concepts relevant to the design of a microstrip patch antenna for a MIMO radar system. The objective of this review is to provide the theoretical foundation necessary to establish the antenna performance requirements, identify suitable antenna architectures from the literature, and support the design and tuning procedures presented in subsequent chapters.

In Section 2.1, the fundamental characteristics of microstrip patch antennas are introduced, including their radiation properties, impedance behaviour, bandwidth limitations, efficiency, and array integration considerations. In Section 2.2, common feeding techniques and feed network architectures are then reviewed, with emphasis on series-fed and corporate-fed structures suitable for compact antenna arrays. Next in Section 2.3, antenna array theory is presented to describe how multiple antenna elements can be combined to achieve desired radiation characteristics. The principles of phased-array and MIMO radar systems are discussed in Section 2.4, highlighting the relationship between antenna geometry, virtual array formation, angular resolution, and sidelobe performance. Section 2.5 specifies the antenna requirements imposed by the RMC MIMO radar platform and the limitations of the currently deployed antenna system. In Section 2.6, antenna performance targets are established based on these system requirements, including operating frequency, bandwidth, radiation pattern characteristics, mutual coupling constraints, and physical size limitations. Furthermore, representative microstrip patch antenna designs reported in the literature are reviewed and evaluated against these requirements. The most promising configurations are identified to serve as the starting point for the antenna development.

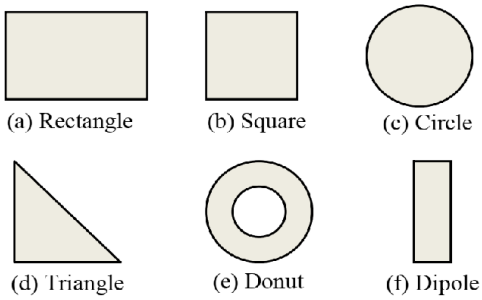


Figure 2.1: Representative shapes of microstrip patch elements [2]

2.1 Microstrip Patch Antenna Characteristics

As illustrated previously in Fig. 1.1, an MPA consists of a thin metallic patch element, typically made of copper, which can take any planar shape. A patch is placed on a dielectric substrate, which is mounted on a metallic ground plane. Fig. 2.1 shows some typical shapes of a patch, with the most common shapes for ease of design and analysis being square, rectangular, dipole and circle [2, 5]. Substrates commercially available have dielectric constants ϵ_r ranging from 2.2 to 12. Thicker substrates with lower ϵ_r are preferred since they provide a larger bandwidth and better radiation into free space [5, 8]; however, this comes at the cost of increased element size [5]. Various input parameters are available for antenna design, including its physical size and element spacing in a microstrip array. Output parameters, such as input impedance, impedance bandwidth and radiation efficiency, are used to evaluate the antenna performance.

2.1.1 Input Reflection Coefficients

Scattering parameters, or S-parameters for short, characterize an antenna's voltage reflection and transmission coefficients. For an N-port antenna system, the reflection coefficients at the individual ports are represented by $|S_{11}|$, $|S_{22}|$, ..., $|S_{ii}|$, where $|S|$ is the magnitude of the S-parameter and $_{ii}$ identifies the reflection coefficient at port i. $|S_{ii}|^2$ describes the proportion of signal power reflected at different ports, providing information about impedance matching. The voltage reflection coefficient of the antenna is defined as [5]:

$$|S_{11}| = \frac{Z_{in} - Z_0}{Z_{in} + Z_0} \tag{2.1}$$

where Z_{in} is the input impedance of the antenna, which varies as a function of

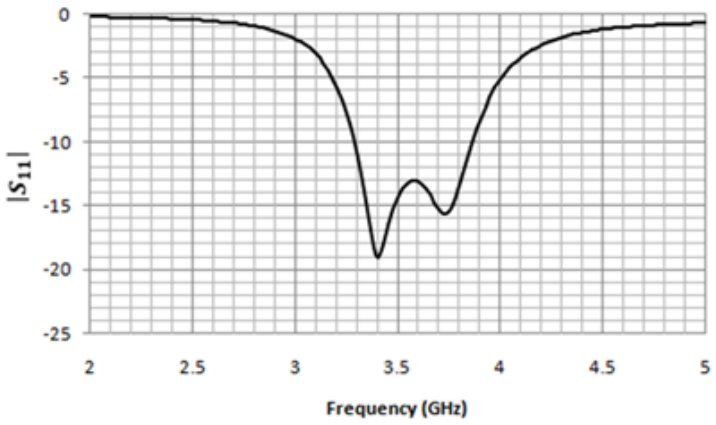


Figure 2.2: $|S_{11}|$ responses versus frequency plot, adapted from [9]

frequency, and Z_0 is the characteristic impedance of the feed line at the port. S-parameters are expressed in dB using this formula:

$$20 \log |S_{11}|. \tag{2.2}$$

When plotted against frequency, the $|S_{11}|$ curve evaluates the antenna's impedance matching to the feed line, specifying the amount of reflected signal, as shown in Fig. 2.2. A value close to 0 dB indicates poor impedance matching, leading to high reflection and minimal power transfer to the antenna. Conversely, an $|S_{11}|$ value of -10 dB or lower is the minimum acceptable threshold, implying that at least 90% of the power is coupled to the antenna [5].

Voltage Standing Wave Ratio $VSWR$ is a metric similar to $|S_{11}|$ that assesses the impedance mismatch between a patch antenna and its source. $VSWR$ is closely related to the reflection coefficient and is defined as [5]:

$$VSWR = \frac{1 + |S_{11}|}{1 - |S_{11}|}. \tag{2.3}$$

A $VSWR$ of one indicates a perfect match, indicating that the input impedance at the feed point equals the source impedance. A value of 2 or lower, which is equivalent to $|S_{11}|$ of -10 dB or lower, is considered acceptable for most applications.

2.1.2 Impedance Bandwidth

The IEEE Standard defines the antenna's bandwidth as "the range of frequencies within which the antenna's performance conforms to the specified standard with respect to some characteristic" [10]. The impedance bandwidth BW is the range of frequencies for which the $VSWR$ or S-parameter falls within a specified range. When the reflection coefficient is plotted against the frequency, the curve within the acceptable $|S_{11}|$ range of -10 dB or lower, or $VSWR$ below 2, defines the antenna's impedance bandwidth. The BW can be expressed as a percentage of the center frequency f_0, called fractional bandwidth FBW and is expressed as:

$$FBW = \frac{f_2 - f_1}{f_0} \times 100\% \tag{2.4}$$

where f_2 is the upper frequency and f_1 is the lower frequency of the bandwidth.

2.1.3 Antenna Radiation Efficiency

The IEEE Standard defines radiation efficiency as "the ratio of the total power radiated by an antenna to the net power accepted by the antenna from the connected transmitter" [10]. This ratio is often expressed as a percentage, where a higher percentage indicates greater antenna efficiency in converting the net power accepted into radiated electromagnetic signals. Conductive and dielectric losses lower the efficiency.

2.1.4 Radiation Pattern

The IEEE Standard defines a radiation pattern as "the spatial distribution of a quantity that characterizes the electromagnetic field generated by an antenna" [10]. A microstrip patch is usually designed to produce maximum radiation in the broadside direction, meaning the electromagnetic waves propagate perpendicular to the patch. For a conventional microstrip patch, this radiation characteristic is primarily achieved by selecting the appropriate excitation mode beneath the patch, which determines the electromagnetic field distribution [5]. For this thesis, the antenna radiation pattern is taken in the far-field region, where the observation point is far enough from the antenna that the angular distribution of the radiated fields becomes independent of radial distance.

The radiation pattern describes the spatial variation of the radiated electromagnetic field or power as a function of direction and is commonly represented using a polar plot, as shown in Fig. 2.3. In such a plot, the angular coordinate specifies the direction of observation, usually expressed in degrees, while the

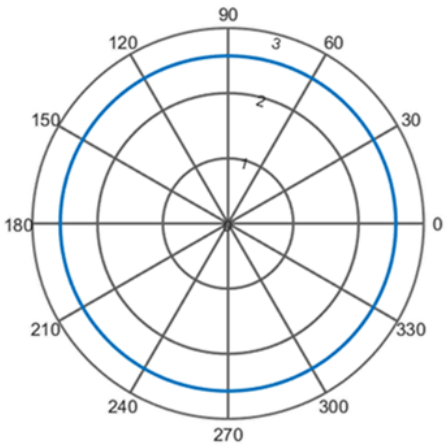


Figure 2.3: An omnidirectional pattern (dBi)

radial coordinate represents the magnitude of the radiated quantity, typically expressed as an absolute or normalized value. When antenna gain is referenced to an isotropic radiator, it is expressed in decibels isotropic (dBi). Depending on the antenna design, the radiation pattern may exhibit different characteristics. For example, an omnidirectional antenna produces approximately uniform radiation in all directions within a specified plane, as illustrated in Fig. 2.3.

Another example is a directional radiation pattern; it produces a more focused pattern characterized by a strong main lobe and weaker sidelobes, as shown in Fig. 2.4. The strongest lobe, observed as the peak on the radiation pattern, indicates the direction of maximum radiation, also known as the main lobe. This direction can be described by the main-lobe angle and its corresponding peak gain. When the radiation pattern reaches the center of the polar plot, corresponding to a radius of (0), the plotted radiation quantity has a null in that direction, indicating where the antenna does not radiate. Smaller lobes, observed as peaks in directions other than the main lobe, are called sidelobes and are generally undesirable because they represent radiation in directions other than the intended main-beam direction. In a MIMO radar, high sidelobes can cause clutter and angular ambiguity caused by strong scatterers located in the sidelobes instead of the main lobe. The relative peak of the largest sidelobe with respect to the main lobe peak is commonly quantified using sidelobe level (SLL), defined as:

$$SLL(dB) = P_{sidelobe}(dBi) - P_{mainlobe}(dBi) \tag{2.5}$$

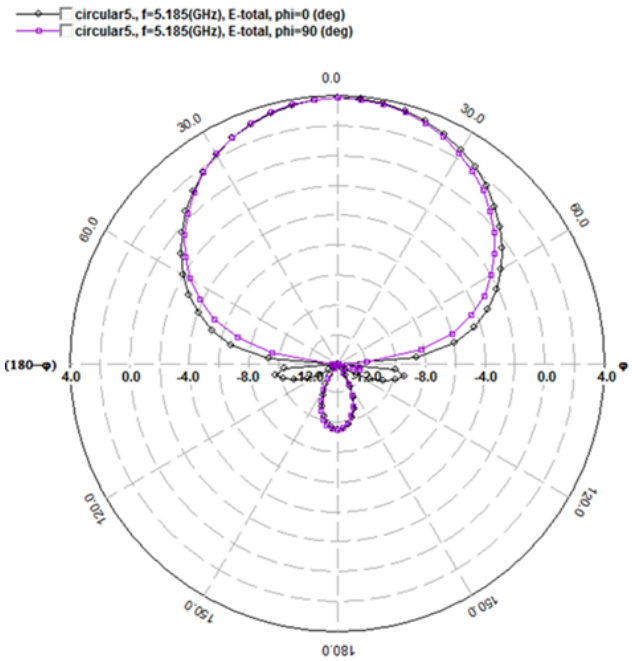


Figure 2.4: Radiation pattern with back radiation sidelobes (dBi) [9]

where $P_{sidelobe}$ is the peak power of the highest sidelobe and $P_{mainlobe}$ is the peak power of the main lobe. A more negative SLL indicates better suppression of unwanted radiation.

2.1.5 Beamwidth and Half-Power Beamwidth

Beamwidth is the general angular width of an antenna's main radiation lobe. Half-Power Beamwidth $HPBW$ is a standardized measure defined by the IEEE Standard as "the angle between the two directions in which the radiation intensity is one-half the maximum value" [10]. Equivalently, these directions correspond to the -3 dB (half-power) points relative to the peak radiation intensity. For a uniform linear array (ULA), the $HPBW$ at boresight is therefore defined as the angular separation between the two -3 dB points θ_{3dB}, given in radians by [11]:

$$\theta_{3dB} \approx \frac{0.88\lambda}{L} \tag{2.6}$$

where L is the aperture length in wavelengths and λ is the wavelength in meters. The aperture length L represents the physical extent of the antenna

array in one dimension, which determines the beamwidth of the main lobe in the same plane.

2.1.6 Front-to-Back Ratio

The front-to-back (F/B) ratio is defined as the ratio of the maximum radiation intensity in the main-lobe direction to the radiation intensity in the rearward direction [10]. It quantifies the antenna's ability to suppress radiation behind the antenna relative to the intended forward direction and is typically expressed in decibels (dB). A higher F/B ratio reduces unwanted interference from behind the antenna.

2.1.7 Antenna Physical Size

Typically, compact antennas are lower-cost and offer greater adaptability, including the ability to be integrated into antenna arrays, such as MIMO arrays. Reducing the antenna's size can lead to reduced bandwidth and gain [12]; however, various techniques exist to mitigate these effects to some extent. The spacing requirements between elements for antenna arrays and MIMO arrays are discussed in Sections 2.3 and 2.4, respectively.

2.1.8 Antenna Element Spacing and Mutual Coupling on a Microstrip Array

In some microstrip antenna designs, the antenna consists of multiple radiating patches to achieve the desired characteristics. In a uniform array, the physical spacing d between radiating elements remains constant, as shown in Fig. 2.5, but as the frequency increases, the electrical spacing, measured in wavelengths λ, increases. This change affects the array's radiation pattern and mutual coupling. In an array, $|S_{ij}|$ represents the transmission coefficient from port j to port i, indicating the amount of signal received at port i when transmitted from port j. This is referred to as mutual coupling, which evaluates the electromagnetic interactions between an antenna and another antenna. Due to the reciprocity of mutual coupling between antennas $|S_{ij}|$ equals $|S_{ji}|$. Mutual coupling is usually undesirable because it changes the current distribution on the antenna, thereby changing its radiation pattern. Mutual coupling can also introduce additional reflections into the feed lines, potentially interfering with other antennas. Therefore, the value of the mutual coupling must be kept as low as possible.

When the inter-element spacing d is greater than 0.5λ, the radiation pattern becomes susceptible to grating lobes, with visible grating lobes always occurring

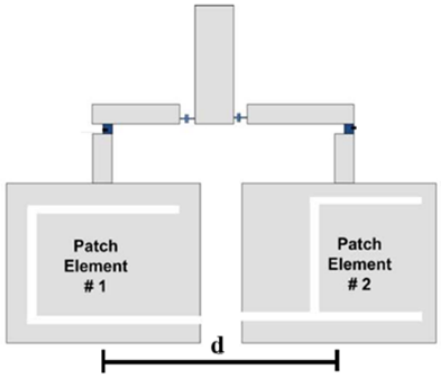


Figure 2.5: Inter-element spacing on a microstrip array, adapted from [13]

if $d \geq \lambda$ [5]. Grating lobes are unwanted radiation pattern maxima in directions other than the main lobe [4, 5]. These grating lobes introduce clutter and reduce the overall radiation of the main lobe located in the desired direction of propagation [5]. Therefore, the distance between elements $d < 0.5\lambda$ can be seen as the limit for preventing grating lobes.

2.2 Feeding Method and Network

A feeding method defines how electromagnetic power is transferred from an input port, typically with a 50 Ω characteristic impedance, to the microstrip patch elements. The choice of feeding method directly influences the antenna's impedance matching, bandwidth, polarization purity, fabrication complexity, cost, and size. Consequently, selecting an appropriate element excitation technique is a critical step in microstrip patch antenna design. The feeding methods, shown in Fig. 2.6, are (a) microstrip line feed, (b) coaxial probe feed, (c) aperture-coupled feed, and (d) proximity-coupled feed.

In the coaxial feed method, the outer conductor of the coaxial cable is connected to the ground plane, and the inner conductor is connected to the patch through a via in the substrate. The microstrip line feed is a conducting strip narrower than the patch, fabricated on the same substrate and connected to the patch's edge. The proximity-coupled feed consists of a feed line placed between two dielectric substrates. The patch is located on top of the upper substrate, enabling electromagnetic power coupling transfer and reducing the spurious radiation from the feed [2]. The aperture-coupled feed is a metallic ground plane with an aperture slot between two dielectric substrates. Under

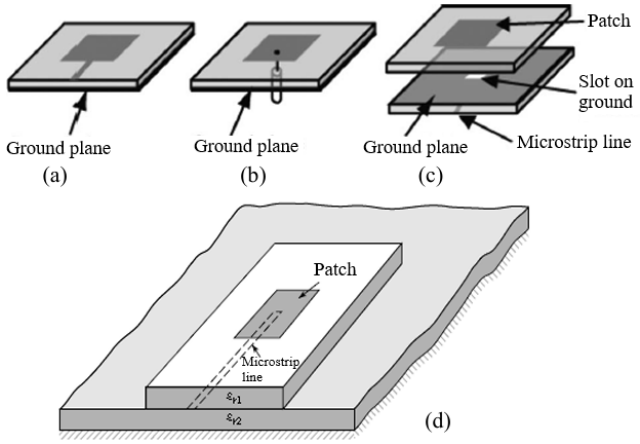


Figure 2.6: Patch antenna feeding methods: (a) line feed, (b) probe-feed, (c) aperture-coupling, and (d) proximity-coupling [5]

the ground plane, the line feed is perpendicular to the aperture slot, providing electromagnetic power coupling between the line feed and the microstrip patch on top where the slot is located. Among the feeding techniques discussed, proximity coupling generally provides a BW approaching 13%, whereas the remaining methods typically achieve BWs on the order of 5% or less [2].

While the feeding method determines how power is delivered to the radiating elements, the feed network governs how power is distributed among multiple elements in an antenna array. The feed network establishes the amplitude and phase excitation of each element, thereby controlling key array characteristics such as gain, directivity, beam shape, sidelobe levels, and scanning performance. Proper feed network design is therefore essential to ensure efficient power transfer, achieve the desired radiation characteristics, and minimize energy reflection back to the source. However, trade-offs exist among impedance matching, antenna size, fabrication complexity, and achievable radiation-pattern characteristics, such as gain and directivity, as determined by the feed-network configuration. They may be implemented using series-fed, parallel-fed (corporate-fed), or hybrid feed structures.

In a series-fed array, shown in Fig. 2.7(a), the first patch extracts a portion of the input power, while the remaining power continues along the feed line to excite subsequent elements through progressive coupling [14]. When all patches in a series-fed array are identical, a natural phase progression still occurs along the structure because the excitation is derived from a travelling wave on the feed line. Consequently, the phase of the coupled excitation varies with the electrical

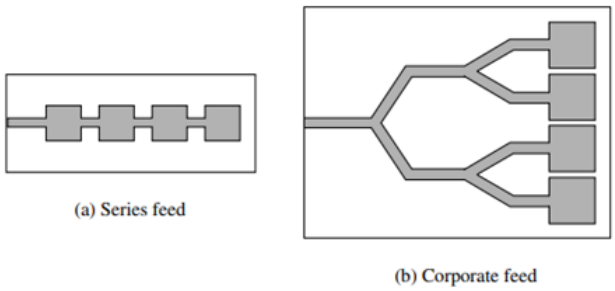


Figure 2.7: Feed arrangements for microstrip patch arrays [5]

distance from the input port, resulting in a progressive phase shift between adjacent elements. The current amplitude distribution is established through distributed coupling, whereas the phase distribution is primarily determined by the electrical distance between successive coupling points. Consequently, amplitude and phase excitations are inherently coupled, making independent control more challenging than in corporate-fed architectures.

A corporate feed array is shown in Fig. 2.7(b). Power dividers split a single input signal into multiple paths to feed different antenna elements in an array. The corporate feed network is designed by controlling the impedance transformation and branch dimensions at each junction to achieve the desired power distribution and current amplitude taper across the array. Furthermore, because each element is supplied through an independent feed path, the phase excitation can be controlled by adjusting the electrical length of the corresponding transmission lines. A quarter-wavelength transformer can be used within the coupling branches to provide impedance matching to the common feed line. However, the increased complexity of the corporate feed network could result in a larger overall antenna size and reduced compactness.

2.3 Antenna Array Theory

A single antenna often cannot meet the requirements of a specific radiation pattern or scan a specific field of view. By combining multiple individual antenna elements, a desirable radiation beam pattern is created in space [15]. The spacing of each transmitting antenna or each receiving antenna forms an array, where its radiation patterns can be shaped using these controls: the configuration of the antenna array, spacing between antennas, phase, amplitude and pattern of the individual antennas [5]. The antenna array can be configured

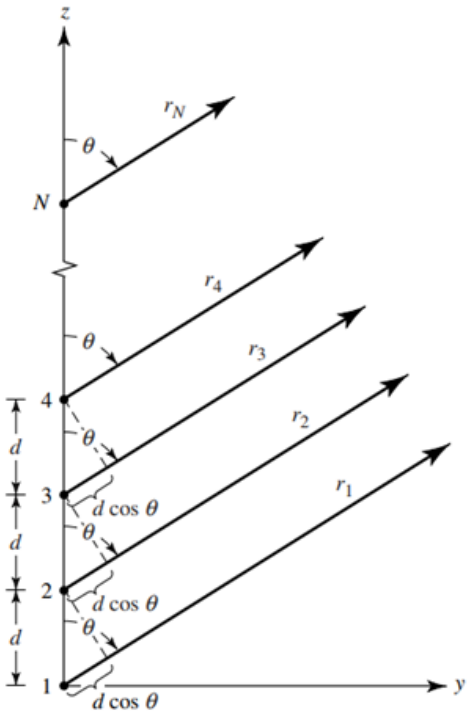


Figure 2.8: N-element linear array [5]

as a uniform linear array (ULA) or a planar array. In a ULA, identical elements are arranged in a line, enabling beam steering in only one plane. An N-element linear array is shown in Fig. 2.8, where d is the distance between elements.

The array factor is determined by the array geometry, and the relative phases and amplitudes. As a result, the array's influence can be analyzed independently of the element radiation pattern by representing each element as an isotropic point source [5]. Then, the total field is obtained by multiplying the individual antenna's field (pattern) and its array factor AF. This product is also called pattern multiplication for arrays of identical elements. This total field is defined as [5]:

$$\overrightarrow{E}_{Total} = \overrightarrow{E}_{Individual\ element} \times AF_{Isotropic\ sources} \tag{2.7}$$

A two-dimensional (2D) Uniform Rectangular Array (URA) is an example of a planar array formed by arranging M-elements along the x-axis and N-elements along the y-axis, resulting in a total of $M \times N$ elements, as shown in Fig.

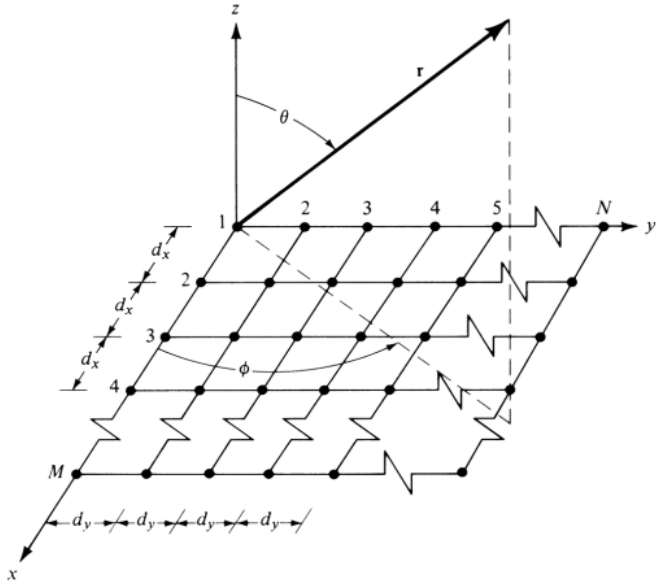


Figure 2.9: $M \times N$ planar array [5]

2.9. This configuration extends radiation pattern control to two dimensions, namely the azimuth and elevation planes, enabling full 2D beamforming. The total AF is obtained by separating the array into its x- and y-direction components and multiplying the resulting two AFs. To suppress the formation of grating lobes in both x-z and y-z planes, the inter-element spacing in the x- and y- directions must be properly constrained [5]. The element spacing is selected to be less than half a wavelength, such that $d_x < 0.5\lambda$ and $d_y < 0.5\lambda$, where d_x and d_y denote the spacing between adjacent elements along the x- and y- direction, respectively.

2.4 Phased Array and MIMO Radar Theory

Phased array radar consists of multiple antenna elements arranged in an array configuration, allowing for electronic beam steering without physically moving the antenna. To do so, amplitude and phase shift weighting are applied to shape and steer the beam [16]. The phase shift applied to each element determines the steering angle θ, as shown in Fig. 2.8 [16]. In contrast, the shape of the beam depends on the antenna element, the scan angle, the spacing between each element and the amplitude applied to each element, as the beamwidth generally

increases at larger scan angles [16]. This technique enables constructive and destructive interference, creating and directing a focused beam toward a desired angle.

MIMO radar usually has dedicated, spatially separated transmit (TX) and receive (RX) arrays, enabling the receive processor to construct the pattern [16]. A radar exhibits a two-way radiation pattern, which is the product of the one-way transmit and one-way receive patterns. The two-way beam pattern is usually narrower than the one-way pattern because the aperture encompasses both transmit and receive elements. MIMO radar has two configurations. In the first, the transmitters and receivers are located at the same site, typically within a few meters of each other, and are referred to as monostatic radar. In the second, the transmitters and receivers are located at different sites, often separated by several kilometres, and are referred to as distributed radar. This survey paper focuses on monostatic MIMO radar operating at frequencies below 6 GHz.

In Code Division Multiplexing (CDM), each of the MIMO radar's radiating antennas transmits unique independent orthogonal waveforms simultaneously [16]. Because of the different phase shifts associated with the various propagation paths between the antennas and targets, the MIMO receiving elements gather a wide range of spatially diverse copies of both transmitted and reflected signals. Since the transmitted waveforms are orthogonal to each other, MIMO radar can distinguish waveforms from each transmit/receive path using matched filters, allowing for separate identification and processing of waveforms that have travelled unique paths between each transmit and receive antenna [16]. Each matched filter is designed to correspond to only one of the transmitted waveforms. Advanced signal processing techniques are used to process all transmit/receive signal path combinations for demultiplexing and beamforming at the receiver [16].

In a radar, the spatial convolution of the TX array and RX array antenna locations creates a so-called virtual array, which illustrates all of the available unique paths between the TX and RX antennas [16]. An array of M transmitting elements and N receiving elements has a corresponding virtual array of up to MN elements; MN paths are established for the return signal originating from the target. A MIMO radar virtual array with a 2-element TX array separated by a distance of $4d$ and a 4-element RX array separated by a distance of d is shown in Fig. 2.10 [15]. For a target assumed to be at an azimuth angle θ, the phase of the received signal will consist of a linear progression at the receiver elements, with the phase shift received from TX1 being 0, φ, 2φ, and 3φ. Since TX2's signal travels a distance four φ units greater than TX1, its phase progression at the same receiver is 4φ, 5φ, 6φ

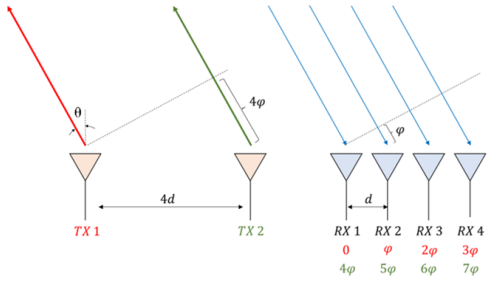


Figure 2.10: MIMO radar virtual array [15]

and 7φ. Concatenating the received signals yields the same configuration as a uniform linear array with one TX and eight RX antennas [15]. Since the incident angle of the wavefront θ (rad) is measured from the boresight, the phase shift φ between adjacent antennas can be expressed as [15, 16]:

$$\varphi \;=\; \beta d \;\sin\; \theta \tag{2.8}$$

where $\beta = 2\pi/\lambda$; λ is the wavelength (in meters) and d is the distance between the RX antenna elements (in meters) [15].

2.5 MIMO Radar and Antennas Specifications

The initial work focused on the design, fabrication, and experimental validation of a MIMO Radar at the Royal Military College of Canada (RMC) in April 2021 [6]. The MIMO radar operates over a frequency range of 3 MHz to 6 GHz and incorporates eight TX and eight RX channels. Each channel supports a bandwidth of 200 MHz.

The existing radar employs Taoglas Accura Ultra-Wideband (UWB) FX-UWB20 antennas, selected for its operational frequency of $f_0 = 5$ GHz and the use of the complete 200 MHz bandwidth of the radar channel [6]. Table 2.1 summarizes the principal antenna parameters relevant to the radar application, including the operational frequency range, peak gain, and radiation coverage for each band. Band 1 covers $3.1 - 5.0$ GHz, band 2 $6.0 - 8.2$ GHz and band 3 $8.2 - 10.3$ GHz. Across these bands, it provides peak gains between $4 - 5$ dBi and exhibits an omnidirectional radiation pattern.

To assess the Taoglas antenna for operation near the radar f_0, a network analyzer was used to measure the antenna response over a frequency sweep from 4 to 6 GHz. The measured reflection coefficient exhibits a value of

Table 2.1: Taoglas UWB FXUWB20 specifications

Parameter	**Band 1**	**Band 2**	**Band 3**
Operational Frequency (GHz)	$3.1 - 5.0$	$6.0 - 8.2$	$8.2 - 10.3$
Peak Gain (dBi)	5	4	5
Radiation coverage	omnidirectional	omnidirectional	omnidirectional

$|S_{11}| = -12.92$ dB at $f_0 = 5$ GHz, as shown in Fig. 2.11 [6]. The measured response indicates that the antenna is impedance matched near 5 GHz, although the matching deteriorates toward the upper edge of the $3.1 - 5.0$ GHz operating band. The Taoglas antenna has a rejection band for 5.8 GHz to suppress WiFi bands [7]. In the measured response, this rejection band appears as an increase in $|S_{11}|$ between $5 - 6$ GHz.

The radiation characteristics are illustrated in Fig. 2.12, which presents the E-plane and H-plane patterns at 3, 4, and 5 GHz, and in Fig. 2.13, which shows the three-dimensional omnidirectional radiation pattern at 6.5 GHz [7].

Several deficiencies are present in the existing antenna configuration. First, the antenna exhibits an omnidirectional radiation pattern, causing signals received from behind the radar to appear as clutter on the opposite bearing within the field of view. To counter this problem, antenna elements were placed on a radar-absorbing backplane; however, this results in a loss of approximately half of the radiated power due to back radiation, thereby reducing the radar's range and often introducing additional pattern distortions. Additionally, mutual coupling was not provided. The close placement of omnidirectional elements can lead to high mutual coupling, which adversely affects channel isolation and array calibration. Moreover, although the antennas are inherently ultra-wideband, the radar's constrained channel bandwidth prevents full exploitation of this range. As a result, the achievable range resolution is limited by the system bandwidth rather than the antenna's full bandwidth.

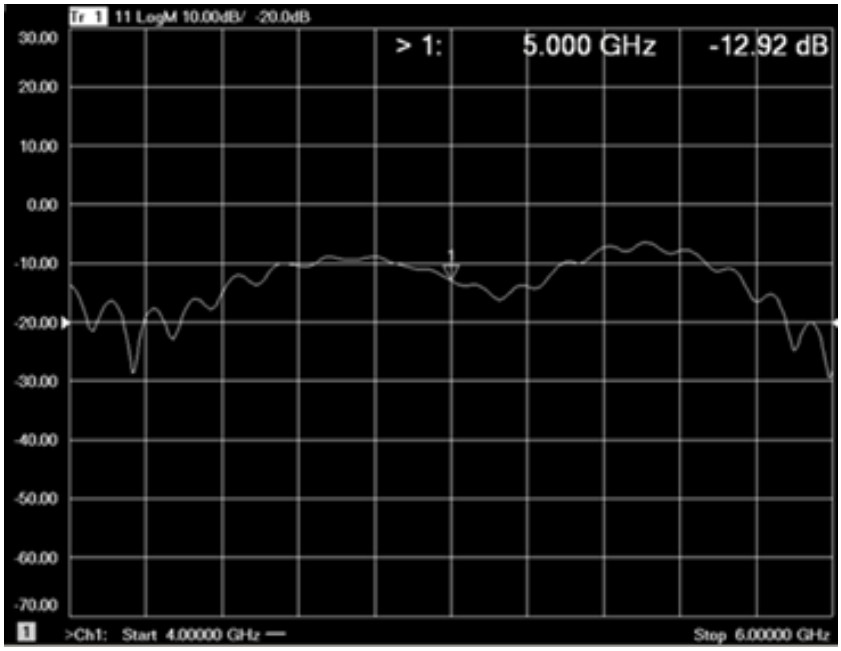


Figure 2.11: Taoglas Antenna $|S_{11}|$ measurement using the network analyzer [6]

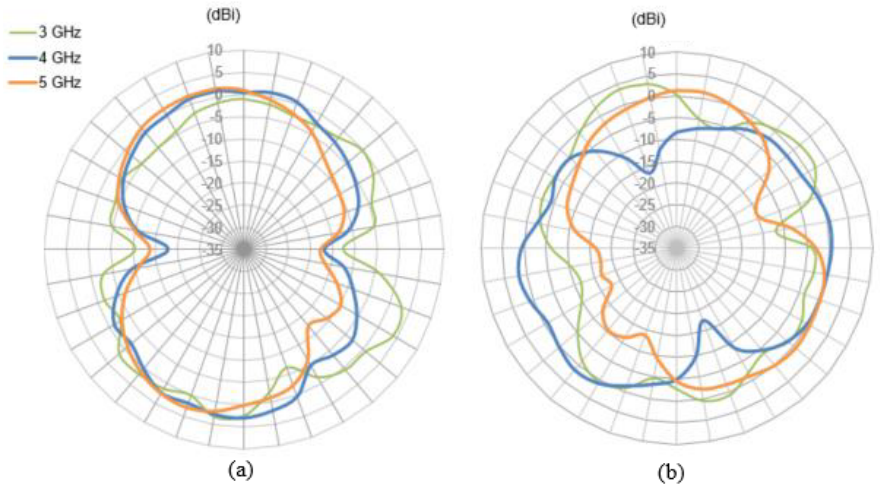


Figure 2.12: Taoglas Antenna Radiation patterns at 3, 4 and 5 GHz: (a) the E-plane and (b) H-plane

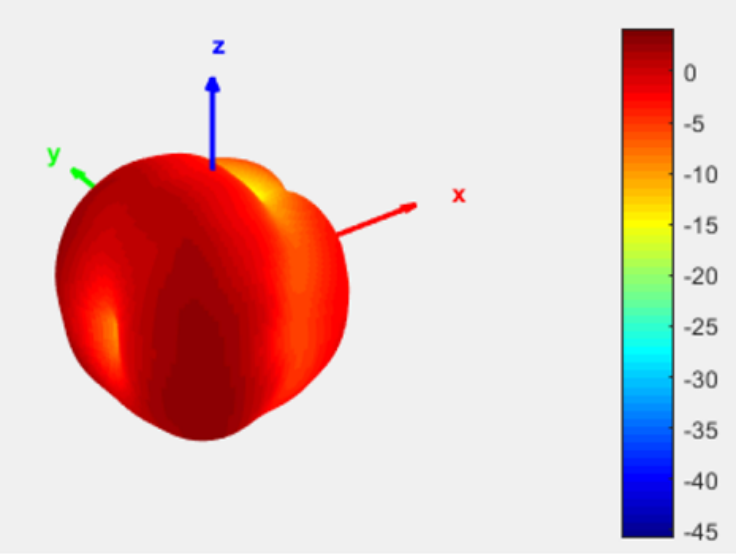


Figure 2.13: Taoglas Antenna 3D radiation pattern [7]

2.6 Antenna Design Requirements

This section presents the antenna design requirements used for developing the MIMO radar antenna and comprises two subsections. First, the key antenna specifications derived from the system requirements are defined. Second, relevant microstrip patch antenna configurations and array network designs reported in the literature have been reviewed and evaluated against these specifications. Based on this assessment, a suitable antenna design and array network design were identified and selected as the starting point for further design refinement and improvement.

2.6.1 Defining the Design Specifications

This section establishes the operating frequency, array constraints, and desired radiation characteristics. Two antenna configurations are designed: a subarray antenna for TX and a 2D planar array for RX. The planar array consists of 8 subarrays on a single finite ground plane. For this section, the design requirements apply to both antennas unless specifically noted.

First, the operational frequency was set to approximately 5.75 GHz, with a target bandwidth of 200 MHz. Section 2.6.1.1 discusses the rationale for this selection. Another key requirement is that the TX antenna elements remain

sufficiently compact to allow integration into an 8 $TX \times 8$ RX array without excessive mutual coupling. Two preferred inter-element spacings have been retained for the array design: $TX = 4\lambda,\ RX = 0.5\lambda$ and $TX = 4\lambda,\ RX = 0.8\lambda$. These configurations represent a trade-off among antenna element size, grating-lobe control, and virtual array aperture. The TX subarray antenna must be designed with one of these spacing configurations to allow integration into the RX planar antenna, while maintaining the specified performance targets, as further discussed in Section 2.6.1.3.

The desired radiation pattern of the TX subarray antenna is directional, with sidelobe levels ≤ -15 dB and low back radiation, with a preferred front-to-back ratio of ≥ 20 dB. In the azimuth plane, a wide forward-looking beamwidth of up to 180° and a narrower beam in the elevation plane, $25° - 75°$ is preferred. For further discussion, refer to Section 2.6.1.2. Since the azimuth and elevation beamwidths are general terms, the standardized parameters of peak gain, peak angle and $HPBWs$ will be used to compare simulated and measured values.

These targets, summarized in Table 2.2, serve as benchmarks for evaluating candidate designs and identifying the modifications required to meet the radar's operational needs. Based on these specifications, antenna designs from the literature have been selected for further investigation. Each candidate is assessed for its potential to satisfy the required frequency band, radiation characteristics, and physical constraints.

2.6.1.1 Selecting the Antenna Frequencies

A conventional microstrip patch antenna exhibits limitations such as narrow impedance bandwidth, low gain, and relatively large physical size at lower operating frequencies [2, 5]. These characteristics directly influence radar system performance, particularly in terms of range resolution and array integration. The range resolution is the ability to separate between closely spaced objects. The range resolution of a radar system is inversely proportional to the antenna's operational bandwidth. It is defined as [17]:

$$range\ resolution = \frac{c}{2 * BW} \tag{2.9}$$

where c is the speed of light in m/s, and BW is the bandwidth in Hz.

For example, a conventional MPA with a bandwidth of around 1% at 6 GHz would achieve a range resolution of approximately 2.5 m; with 10% BW the range is 0.25 m. Achieving finer range resolution requires a wider antenna bandwidth, motivating the development of a wideband design for MIMO radar. However, the radar system has only a 200 MHz BW per channel, corresponding

Table 2.2: TX and RX Antennas performance targets for the MIMO radar application

Parameter	**Target Value**	**Notes**
Radar Frequency Band	$5.25 - 5.925$ GHz	Preferred for compact Size
Operational Frequency	5.75 GHz	Preferred for compact size
Bandwidth	≈ 200 MHz (3.5%)	Matches SDR channel BW limit
S-parameters $\lvert S_{ii}\rvert$	≤ -10 dB	Across operational band for all antennas
Width of element and array feed network	Compact for 2D planar array	Suitable for 8×8 array
Polarization	Linear	
TX Sidelobe Level	≤ -15 dB in azimuth and elevation	Suppress clutter
TX Azimuth $HPBW$	between $40° - 80°$ at boresight	Forward coverage
TX Elevation $HPBW$	between $15° - 60°$ at boresight	Avoid floor/ceiling clutter
TX F/B Ratio (optional)	maximize, optimal$\geq$ 10 dB	Minimize back radiation
RX Mutual Coupling $\lvert S_{ij}\rvert$	≤ -15 dB	Between adjacent elements in the RX planar antenna
RX F/B Ratio (optional)	maximize, optimal$\geq$ 20 dB	Minimize back radiation

to a range resolution of 75 cm, which is the finest range resolution available. Designing an antenna with a bandwidth significantly larger than 200 MHz will not improve range resolution, but it remains crucial that the antenna exhibits good impedance matching, radiation characteristics, and polarization performance across the radar's entire operational band. The operating frequency of a microstrip antenna is inversely related to its physical size. For a rectangular patch, the resonant length L of the antenna is approximately half the guided wavelength λ_g:

$$L \approx \frac{\lambda_g}{2} = \frac{c}{2f_r\sqrt{\varepsilon_r}} \tag{2.10}$$

where f_r is the resonant frequency and ε_r is the relative permittivity of the substrate. For example, a microstrip patch antenna at 6 GHz has a length of approximately 25 mm, whereas at 1 GHz, the length increases to approximately 150 mm. So, antennas operating at lower frequencies require larger patches, which may impose integration constraints in compact radar arrays. Conversely, higher frequencies allow for smaller elements, simplifying integration into compact MIMO arrays, though maintaining a wide impedance bandwidth becomes more challenging.

The selection of the operational frequency band must also comply with Canadian frequency allocations. For a ground-based radiolocation radar, the allocated frequency bands from 3 MHz to 6 GHz are: $3.23 - 3.4$ MHz, $430 - 438$ MHz, $1215 - 1390$ MHz, $2.3 - 3.1$ GHz, $3.1 - 3.3$ GHz and $5.25 - 5.925$ GHz [18]. Considering antenna size constraint, SDR bandwidth limitations, and range-resolution requirements, the preferred radar operational band for this MIMO radar is $5.65 - 5.85$ GHz, with an operational frequency of 5.75 GHz. This frequency range enables compact antenna elements suitable for an 8×8 array while providing sufficient operational bandwidth for sub-meter range resolution and regulatory compliance.

2.6.1.2 Defining the Radiation Pattern of the TX Antenna

The desired radiation pattern of the subarray antenna is directional, with sidelobe levels ≤ -15 dB, to reduce interference between adjacent elements and minimize clutter returns. Radiation toward the back plane must be suppressed to ensure a high F/B ratio, with a preferred ratio of ≥ 10 dB. This means that the antenna radiates strongly toward the desired forward coverage area while reducing interference and unwanted reflections from objects behind the antenna (e.g., walls, equipment).

In the azimuth plane, a wide forward-looking angular coverage of up to 180° is required to provide full coverage of the radar's field of view. In the

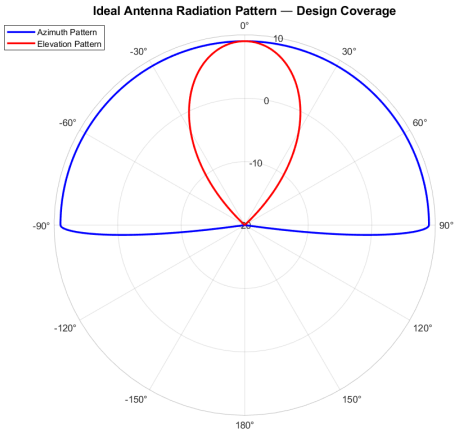


Figure 2.14: Conceptual ideal radiation pattern with 180° azimuth and 30° elevation

elevation plane, a narrower angular coverage of at least 25° and at most 75° is preferred to limit illumination of undesired areas, such as the ceiling and floor. This helps reduce elevation-extent clutter and multipath effects within the indoor laboratory environment. An example of the conceptualized ideal radiation pattern is shown in Fig. 2.14, featuring a 180° forward-looking angular coverage in the azimuth plane and a narrower 30° angular coverage in the elevation plane.

As established in Section 2.1.5, the aperture length and beamwidth are inversely related, as expressed by the $HPBW$ ($\theta_{3\text{dB}}$) equation. Thus, the desired elevation $HPBW$ range of $25° - 75°$ can be used to estimate the corresponding aperture length required at each operating frequency. In general, increasing the aperture length produces a narrower beamwidth, higher directivity, and improved angular resolution. This relationship provides a basis for selecting an appropriate antenna aperture while balancing elevation coverage and angular resolution. Table 2.3 summarizes the aperture lengths calculated for the target elevation $HPBW$ range over the operating frequency band.

2.6.1.3 Antenna Spacing in MIMO Virtual Array

In a MIMO radar system, the inter-element spacing of the TX and RX arrays determines the structure of the virtual array and directly influences angular resolution and sidelobe performance. For a linear array with $N_{TX} = 8$ and

Table 2.3: Aperture sizes for different frequencies and beamwidths

Frequency (GHz)	L **for** 25° **beam (mm)**	L **for** 75° **beam (mm)**
5.25	115.2	38.4
5.75	105.2	35.1
5.925	102.1	34.0

Table 2.4: Comparison of spacing configurations for an 8×8 MIMO linear array

Parameter	**Config. A**	**Config. B**
$TX \times RX$ Elements	8×8	8×8
Spacing TX	4λ	4λ
Spacing RX	0.5λ	0.8λ
Number of Virtual Elements	64	64
Number of Unique Virtual Elements	64	43
$HPBW$	1.583°	1.570°
First SLL Peak	-13.25 dB	-13.98 dB
First SLL Angle	$\pm 2.56^\circ$	$\pm 2.54^\circ$
Highest SLL Peak	-13.25 dB	-13.77 dB
Highest SLL Angle	$\pm 2.56^\circ$	$\pm 14.32^\circ$

$N_{RX} = 8$, two TX/RX spacing configurations were retained as shown in Table 2.4, where d (λ) is the distance between each antenna. Their radiation patterns are shown in Fig. 2.15. The patterns incorporate the effects of overlapping virtual elements and their corresponding amplitude weights. The MATLAB code, provided in Appendix A, generates the radiation patterns and extracts key metric parameters.

A spacing $> 0.5\lambda$ provides greater physical separation that may facilitate the implementation of the antenna elements and their feed networks. While this decreases the number of individual virtual elements, the $HPBW$ is narrower and, consequently, improves the ability to distinguish targets with small angular separations [1]. Configuration B produces a smaller $HPBW$ of approximately 0.009% compared with configuration A, slightly improving angular resolution.

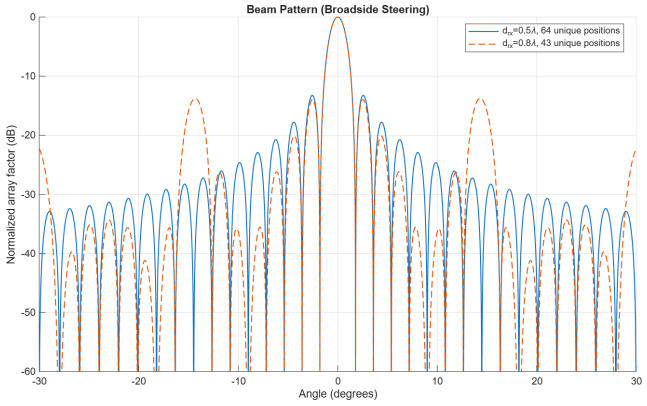


Figure 2.15: Beam pattern for both configuration

For a maximum operating frequency of 6 GHz, $\lambda_0 \approx 50$ mm and with 0.5λ spacing, the inter-element spacing is approximately 25 mm. At 6 GHz with 0.8λ spacing, the inter-element spacing is approximately 40 mm.

When the RX element spacing is increased from 0.5λ to 0.8λ, the number of unique virtual elements decreases because the convolution of the transmit and receive arrays produces overlapping virtual positions. At the same time, the larger element spacing increases the physical and effective array apertures, narrowing the main beam and therefore, improving angular resolution. It also provides additional space for the array feed network and facilitates the implementation of dual-polarized or broadband patch elements. However, this benefit comes at the expense of a higher susceptibility to grating lobes, increased sidelobe levels, a reduced unambiguous field of view and a greater risk of angular ambiguities. Conversely, denser inter-element spacing provides better spatial sampling, enlarges the unambiguous field of view, reduces the likelihood of angular ambiguities and reduces the risk of grating lobes, although it imposes stricter physical constraints on the antenna elements and feed network designs. Therefore, the selected inter-element spacing represents a trade-off among angular resolution, unambiguous field of view, sidelobe performance, and antenna implementation constraints.

2.6.2 Survey of Microstrip Patch Antennas from the Literature

The antenna specifications defined in Section 2.6.1 serve as the evaluation criteria for selecting antenna designs reported in the literature. Candidate

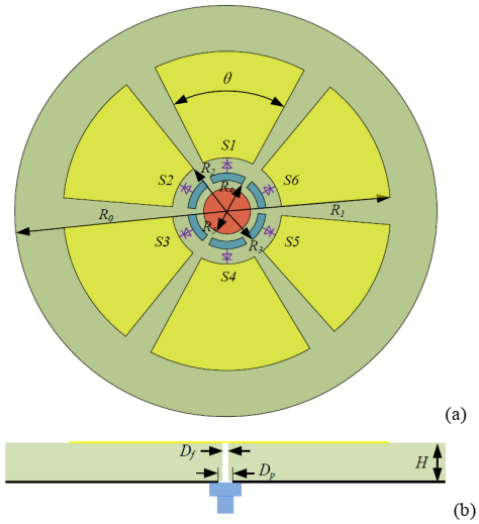


Figure 2.16: Geometry of the circular patch with fan-shaped coupling patches antenna: (a) top, (b) side view [19]

antennas were assessed according to their operating frequency, bandwidth, radiation characteristics, compactness, and suitability for integration into a 2D planar array. In this work, the term compact refers to minimizing the transverse width of the antenna such that it can be integrated within the constrained inter-element spacing of the MIMO RX array. This requirement is particularly important in MIMO systems, where multiple antennas including their feed networks must be integrated within constrained element spacing while minimizing their impact on mutual coupling and radiation characteristics.

2.6.2.1 Circular MPA with fan-shaped cells

A circular patch antenna with fan-shaped cells is shown in Fig. 2.16. The red region is used for connecting a 50 Ω coaxial cable [19]. The blue and yellow regions are six fan-shaped coupling and radiation cells, respectively. Between the blue and yellow regions, six RF switches are used to connect or disconnect the coupling and radiation cells, thereby changing by a few dB the impedance bandwidth or radiation pattern peak gain. This antenna is fabricated on a FR4 substrate having a thickness of 3 mm and $\epsilon_r = 4.3$ [19].

This antenna has a resonant frequency of 4 GHz. The $|S_{11}|$ of the slotted circular patch antenna with S1 and S2 switched on is plotted against the frequency in Fig. 2.17. The antenna exhibits a -10 dB BW of 125 MHz or

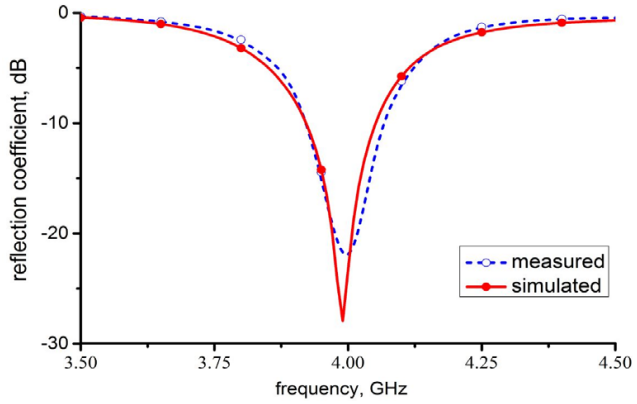


Figure 2.17: $|S_{11}|$ of circular MPA with fan-shaped cells [19]

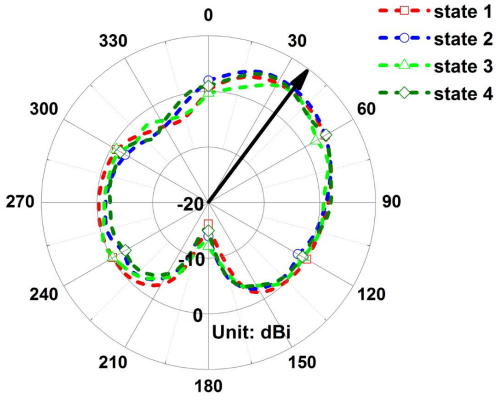


Figure 2.18: Pattern of Circular MPA at 3.5 GHz [19]

3.5%. The patch radius $R_1 = 20.5$ mm corresponds to a diameter of 0.55λ at 3.48 GHz, which is compact enough to be placed in a 2D planar array with 0.8λ spacing between elements.

Fig. 2.18 presents the E-plane radiation patterns for the four antenna states. All states exhibit a stable directional radiation characteristic with the main beam oriented approximately at 40°. The antenna provides a broad forward coverage. The estimated front-to-back ratio exceeds $20 - 25$ dB, indicating effective suppression of backward radiation. Only minor variations are observed among the four states, demonstrating that the reconfiguration mechanism has minimal impact on the overall radiation characteristics and radiation efficiency.

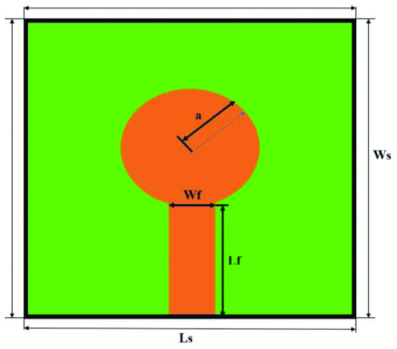


Figure 2.19: Geometry of the circular antenna [20]

2.6.2.2 Circular MPA with directional pattern

A circular patch antenna with a microstrip feed line is illustrated in Fig. 2.19. The antenna is fabricated on a Rogers RT 5880 substrate having $\epsilon_r = 2.2$ and a height of 0.6 mm [20].

This antenna was reproduced in ANSYS HFSS and has a center frequency at 28.6 GHz and a patch radius of 3.8 mm. The array footprint is 15.3 mm long by 7.6 mm wide, corresponding to $L_s = 1.45\lambda$ by $W_s = 0.362\lambda$, which is compact enough to be integrated into a 2D planar array with 0.8λ spacing between elements. Fig. 2.20 shows the $|S_{11}|$ of the circular patch antenna plotted against the frequency. The antenna exhibits a -10 dB BW of 2.1 GHz or 7.3%. Its operating frequencies are substantially higher than the desired radar band. Therefore, the geometry would require redesign to operate within the target radar frequency range of $5.25 - 5.925$ GHz.

Fig. 2.21 shows E-plane in green and the H-plane in red. The E-plane exhibits a dual-lobe radiation pattern with peak gains of ≈ 6 dBi at $-52°$ and $52°$ with a low front-to-back ratio of 11 dB. The H-plane presents a wide broadside radiation pattern with peak of 3.36 dBi at $28°$ and a low front-to back ratio of 8.7 dB.

2.6.2.3 Rectangular versus Circular MPA

Rectangular and circular microstrip patch antennas (MPAs) are two commonly used configurations. A comparative study of these geometries at 10 GHz was presented in [21]. Both antennas were fabricated on RT5880 substrates with a thickness of 1.588 mm and a relative permittivity of $\epsilon_r = 2.2$, and were excited using microstrip-line feeds. The antenna geometries are shown in

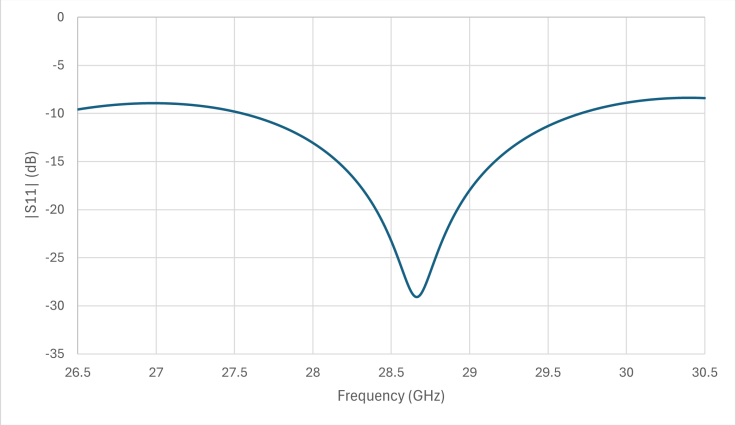


Figure 2.20: $|S_{11}|$ of the circular patch

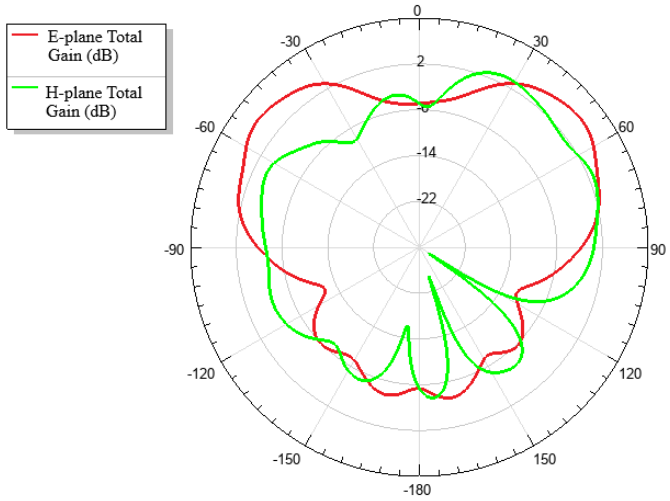


Figure 2.21: Radiation patterns of the circular patch

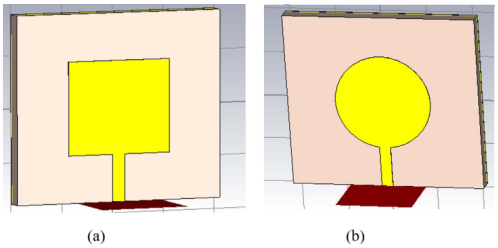


Figure 2.22: MPA (a) rectangular (b) circular

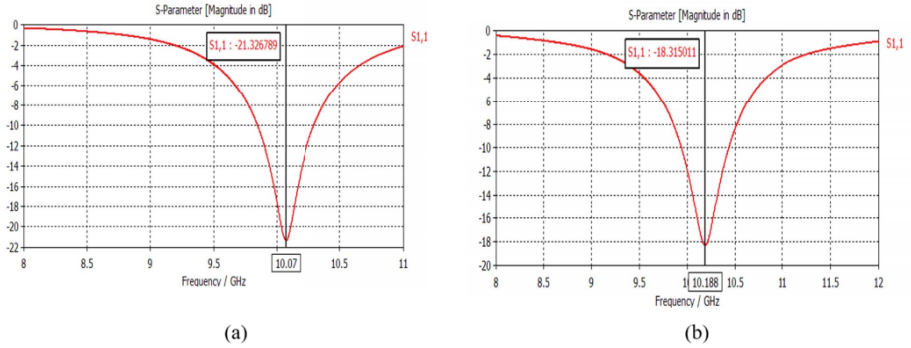


Figure 2.23: $|S_{11}|$of (a) rectangular MPA (b) circular MPA [21]

Fig. 2.22. In terms of physical dimensions, the rectangular MPA occupies a footprint of 13.2×10 mm, whereas the circular MPA occupies a footprint of 9.7×10.5 mm. These dimensions correspond to approximately $0.45\lambda \times 0.34\lambda$ and $0.33\lambda \times 0.35\lambda$, respectively. The circular geometry therefore provides a smaller physical footprint, which may be advantageous when integrating multiple elements into a compact antenna array.

The rectangular MPA resonates at 10.1 GHz, with a bandwidth of 453 MHz, corresponding to approximately 4.49% of its resonant frequency. The circular MPA resonates at 10.2 GHz, with a bandwidth of 488 MHz, corresponding to approximately 4.78%. The reflection-coefficient responses of both antennas are presented in Fig. 2.23, allowing their impedance-matching characteristics and operating bandwidths to be compared.

The E-plane radiation patterns of the two antennas are compared in Fig. 2.24. Both antennas shows directional radiation pattern. The circular MPA exhibits an $HPBW$ of 75.8°, which is 1.8° wider than that of the rectangular MPA, indicating a slightly broader main beam. In addition, the circular

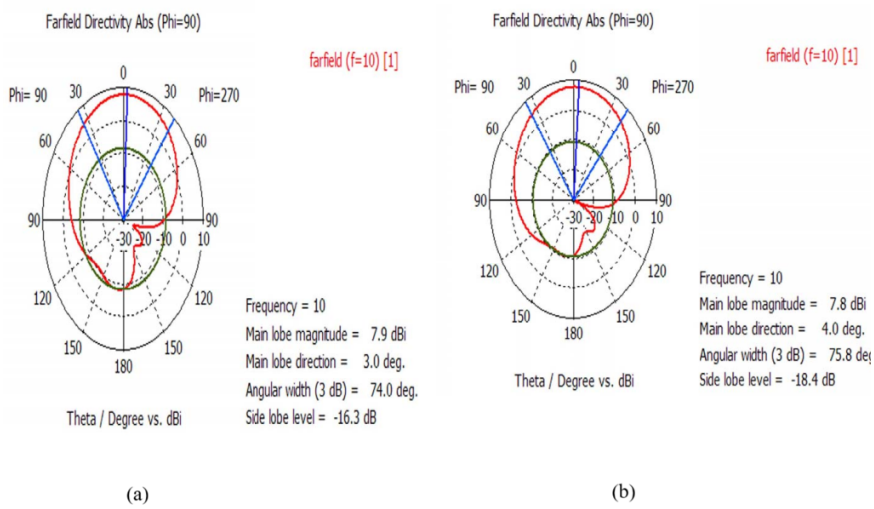


Figure 2.24: Radiation pattern of (a) rectangular MPA (b) circular MPA [21]

MPA achieves a sidelobe level of −18.4 dB, compared with −16.3 dB for the rectangular MPA, representing an improvement of 2.1 dB in sidelobe suppression. Therefore, the circular MPA offers a smaller footprint, a slightly wider main beam, and better sidelobe suppression than the rectangular MPA, based on the reported results.

2.6.2.4 Comparison of the Antenna Designs

Table 2.5 summarizes the key characteristics of the antenna designs selected for evaluation. The pattern-reconfigurable circular patch provides directional radiation and pattern-reconfiguration capability but requires a relatively complex implementation involving RF switches and a feeding structure that may complicate array integration. The circular patch operating at 28.5 GHz offers the largest bandwidth and highest reported efficiency, but its frequency is substantially higher than the target radar band and would require redesign.

The rectangular and circular MPAs reported in [21] provide a more direct comparison of conventional patch geometries. Although both exhibit similar bandwidths and directional radiation characteristics, the circular MPA offers a smaller footprint, a slightly wider beamwidth, and lower sidelobe levels than the rectangular MPA. These characteristics are advantageous for integration into a compact MIMO radar array where element spacing is constrained. Based on compactness, directional radiation capability, sidelobe suppression, and ease

Table 2.5: Comparison of Antenna Designs

Antenna Design	**Substrate**	**Element Size $L \times W$**	f_0 **(GHz)**	BW	**Radiation Pattern and Efficiency**
Circular MPA with fan-shaped cells 2.16	FR4 ($\varepsilon_r = 4.3$)	41×41 mm ($0.55\lambda \times 0.55\lambda$)	4	$\approx 3.5\%$	Directional; broad forward beam, F/B ratio > 20 dB; efficiency not specified
Circular Patch with directional pattern [19]	Rogers RT5880 ($\varepsilon_r = 2.2$)	15.3×7.6 mm ($1.45\lambda \times 0.73\lambda$)	28.5	$\approx 7.3\%$	Directional broadside pattern; 94% efficiency
Rectangular MPA [21]	RT5880 ($\varepsilon_r = 2.2$)	13.2×10.0 mm ($0.45\lambda \times 0.34\lambda$)	10.1	$\approx 4.5\%$	Directional pattern; $HPBW \approx 74^\circ$; sidelobe level -16.3 dB
Circular MPA [21]	RT5880 ($\varepsilon_r = 2.2$)	9.7×10.5 mm ($0.33\lambda \times 0.35\lambda$)	10.2	$\approx 4.8\%$	Directional pattern; $HPBW \approx 76^\circ$; sidelobe level -18.4 dB

of integration into an antenna array, the circular patch geometry was selected as the starting point for the antenna design.

2.6.3 Survey of Array Network Design from the Literature

To achieve the required elevation coverage, the array must use amplitude and phase tapers as discussed in Section 2.3. Therefore, feed network architectures in the literature were assessed based on their power-distribution characteristics, including amplitude tapering and phase-control capabilities, their compactness for integration into an array and their fabrication simplicity. For the purposes of this thesis, both single-port series-fed networks and compact corporate-feed

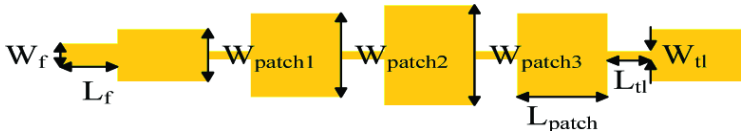


Figure 2.25: 1×5 linear array [23]

networks were investigated.

2.6.3.1 Series-Feed Array Network Design

A series-fed array employs a feed network in which adjacent patch elements are connected sequentially along a single transmission line, forming a continuous daisy-chain structure. As the electromagnetic wave propagates along the feed line, each element extracts a portion of the available power while the remaining power continues to subsequent elements. The amplitude distribution can be adjusted by modifying the patch widths. The excitation phase of each element is determined by the electrical length of the transmission line between adjacent patches. By appropriately selecting these inter-element transmission-line lengths, a desired phase distribution can be achieved across the array. However, this approach does not account for mutual coupling effects or the influence of element spacing on the array radiation characteristics. In practice, these effects can modify the excitation amplitudes and phases of the elements, leading to deviations from the intended radiation pattern, increased sidelobe levels, and the occurrence of grating lobes when the element spacing becomes excessively large [22].

A 1×5 series-fed patch array operating at 62 GHz is shown in Fig. 2.25. Each patch has a length of approximately $\lambda_g/2$, where λ_g is the guided wavelength within the substrate. The transmission lines between elements are approximately $\lambda_g/4$ long [23], introducing a progressive phase shift between elements that tilts the main beam in the radiation pattern. To further shape the aperture amplitude distribution, the patch widths are tapered, with the central element being the widest and the outer elements progressively narrower. The array footprint is 14.96 mm long by 1.8 mm wide, corresponding to 3.09λ by 0.37λ, which is compact enough for array integration.

2.26(a) shows that the antenna operates at 62 GHz and achieves an impedance bandwidth of approximately 9.7%. Fig. 2.26(b) shows the simulated E-plane radiation with a peak gain of 9.3 dBi at 29° from broadside. The wide bandwidth and inherent beam steering capability demonstrate the effectiveness of the series-fed travelling-wave architecture.

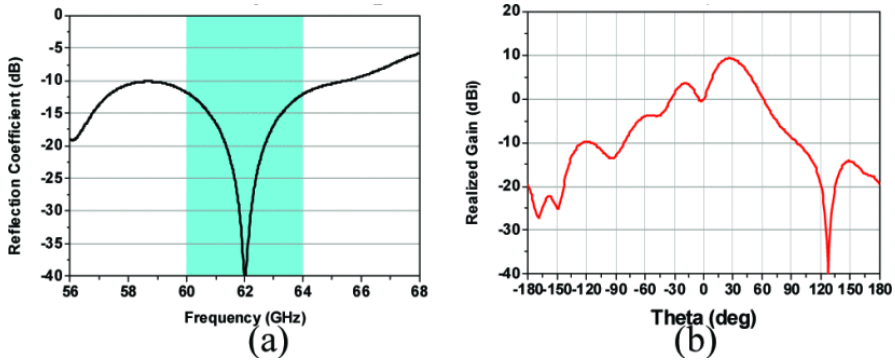


Figure 2.26: Simulated result of the 1×5 (a) reflection coefficient, (b) radiation pattern [23]

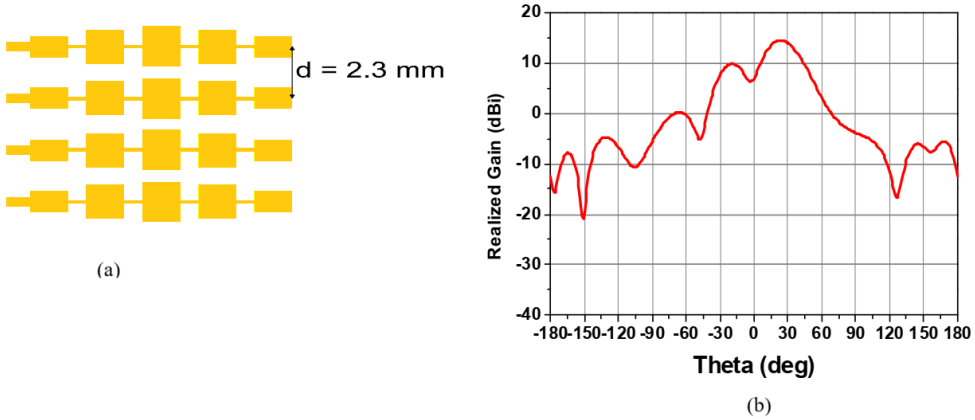


Figure 2.27: 4×5 planar array configuration

To increase gain and extend the detection range, four identical 1×5 linear arrays are combined to form a 4×5 planar array as illustrated in Fig. 2.27. The linear arrays are spaced by 2.3 mm, corresponding to approximately 0.5λ at 62 GHz. This arrangement increases the effective aperture area while maintaining acceptable grating-lobe performance. Simulated results indicate that the maximum gain increases from 9.3 dBi to 14.4 dBi. The main beam remains tilted, shifting slightly to approximately 27°, demonstrating that the planar configuration preserves the desired beam direction while providing substantial gain.

Achieving in-phase excitation in a conventional series-fed array may require

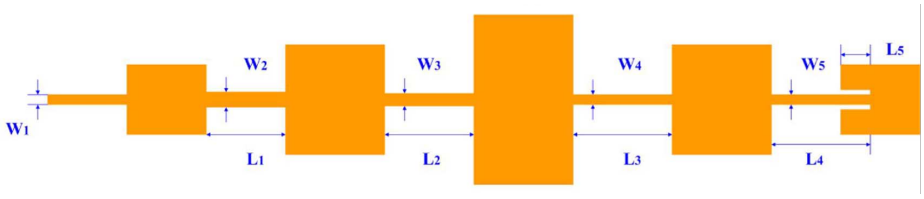


Figure 2.28: Comb-Line matching-in-step design [25]

positioning the elements at equivalent voltage points along the feed line, resulting in an inter-element spacing of approximately λ_g [22]. Although this simplifies the phase relationship, the resulting spacing affects mutual coupling, array size, and grating-lobe performance. Alternatively, modelling the square patch as a loaded two-port element allows adjusting the feed-line lengths so the phase distribution is in phase, while maintaining a centre-to-centre spacing closer to 0.5λ [24]. This approach reduces the array size and mitigates the risk of grating lobes but requires joint tuning of the patches, feed sections, and mutual coupling. Quarter-wave impedance transformers may be introduced before each patch to suppress reflections on the feeding line [22]. However, this reduces the bandwidth, consumes extra space and introduces additional design variables.

2.6.3.2 Series-Feed Array Network Design with Matching-in-Step

Fig. 2.28 shows a microstrip antenna array with a matching-in-step feed-line design operating at 5 GHz. The patches are spaced λ apart. The patches and transmission lines are approximately 0.5λ long. The feed lines connecting consecutive patch elements have varying step widths. These steps act as an integrated impedance transformer, matching the patch's impedance to the feed line and minimizing power reflection. Furthermore, the terminal radiating patch is designed as an insert-fed patch to lower its input resistance and match the feed-line impedance. The array footprint is 192.32 mm long by 34.4 mm wide, corresponding to 3.21λ by 0.57λ, which is compact enough for array integration.

Fig. 2.29(a) illustrates that the E-plane sidelobe level is approximately -14 dB relative to the main beam. Because the array is series-fed, the power coupled to each successive element decreases along the feed path, naturally tapering the amplitude distribution. This sidelobe suppression is achieved through the non-uniform excitation of the array elements due to the series-fed architecture, yielding a tapered excitation that contributes to the observed sidelobe level.

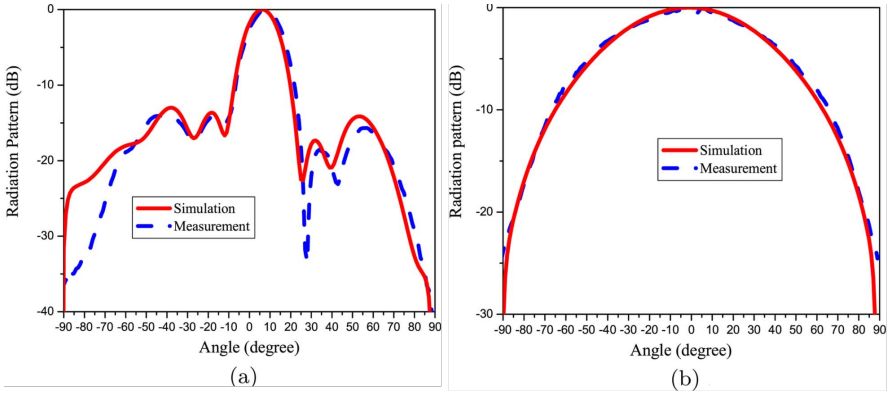


Figure 2.29: Comb-line matching-in-step design radiation pattern (a) E-plane (b) H-plane

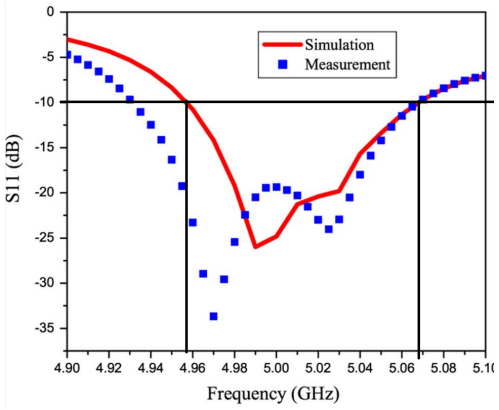


Figure 2.30: $|S_{11}|$ simulated versus measured

Fig. 2.29(b) shows that the H-plane pattern exhibits a single broad main lobe, indicating good broadside radiation characteristics and smooth aperture illumination. This antenna has a simulated BW of 2.2% and a measured BW of 2.8%, as shown in Fig. 2.30.

2.6.3.3 Series-Feed Array Network with Coupling Branches Design

A 1×4 series-fed square patch antenna array employing aperture coupling is shown in Fig. 2.31. The ground plane is located between two substrates with apertures shown as green slots in Fig. 2.31 and the feed network is

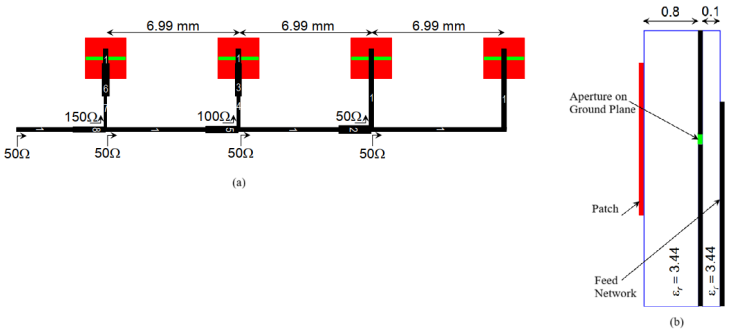


Figure 2.31: (a) Geometry of the series-fed network (b) side view [14]

located under the second substrate. Electromagnetic energy is coupled from the feed lines to the radiating patches via slots etched in the ground plane. This configuration improves isolation between the feed and the patch while reducing spurious radiation from the feed line. The series-fed aperture-coupled network offers a compact feeding architecture because power is distributed along a single main feed line. The desired current-amplitude distribution is achieved through the coupling branches and quarter-wavelength transformer sections [14]. Furthermore, the coupling apertures are positioned such that each patch is excited at the same electrical distance from the feed network. Consequently, all antenna elements are excited with equal electrical phase, resulting in in-phase radiation in the desired direction.

The antenna resonates at 26 GHz, with the array having a BW of ≈ 4 GHz (14%). The array footprint is ≈ 36 mm long by ≈ 5.1 mm wide, corresponding to 3.12λ by 0.44λ, which is compact enough for array integration. In addition, the aperture-coupled configuration requires precise alignment of the radiating patches, coupling slots, and feed network during fabrication. Misalignment between layers can degrade impedance matching, coupling efficiency, and radiation performance, increasing manufacturing complexity compared with single-substrate microstrip-fed designs. Unlike the corporate-feed architecture, which requires multiple power-divider stages, the series-fed network distributes power through a single feed path, reducing routing complexity and occupied area. The radiation pattern of the 1×4 array is not shown.

2.6.3.4 Comb-line Array Antenna

In a traditional comb-line array, the radiating elements are implemented as stubs branching alternately on opposite sides of the feed line, where each single

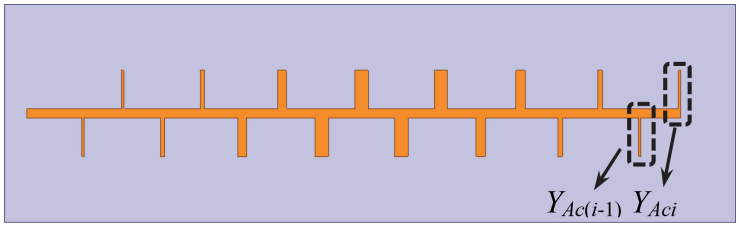


Figure 2.32: Tapered comb-line Array [26]

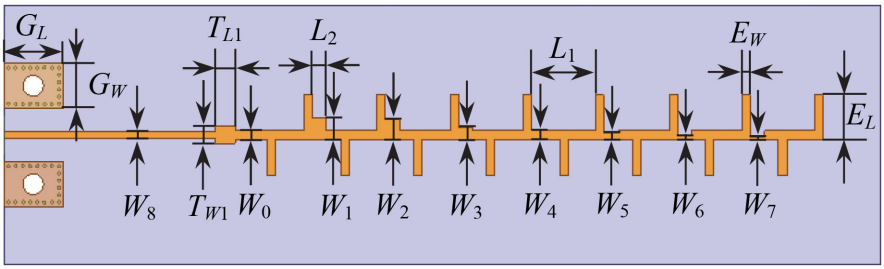


Figure 2.33: Comb-line Array with tapered feed line [26]

comb stub is considered as an antenna element. The excitation amplitude distribution can be controlled by varying comb-stub width. Fig. 2.32 illustrate a 1×12 comb-line antenna array. Adjusting the stub widths changes the amount of power coupled from the main feed line to each radiating element, thereby enabling amplitude tapering across the array aperture [26]. The excitation phase distribution is primarily determined by the electrical spacing between adjacent stubs along the feed line. Suppressing reflections is critical, as unwanted reflections can build up along the line, degrading the impedance matching. Many designs use reflection-canceling slits or stub-integrated elements to counteract this effect.

Alternatively, the amplitude distribution can be controlled by varying the main feed line width while keeping the stub width constant. A 1×8 comb-line antenna array at 24 GHz employing microstrip feed line is shown in Fig. 2.33. For this design, an antenna element is comprised of a pair of adjacent short strips spaced $\lambda_g/2$ between each other, reducing the number of amplitude tapers to half of a traditional comb-linear array [26]. The array footprint is ≈ 135 mm long by ≈ 4.34 mm wide, corresponding to 10.8λ by 0.35λ, which is compact enough for array integration.

Fig. 2.34 illustrates that the BW is only shown partially and corresponds

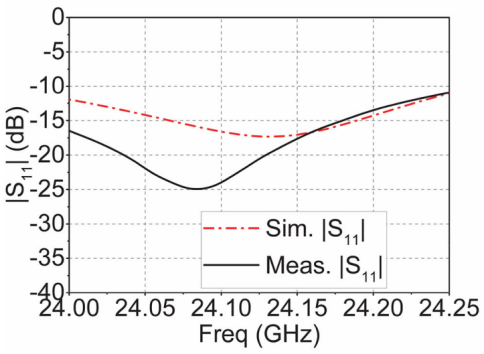


Figure 2.34: $|S_{11}|$ of the comb-line Array with tapered feed line

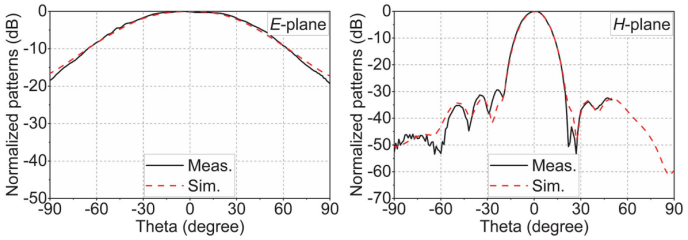


Figure 2.35: Radiation patterns of the comb-line Array with tapered feed line

to at least 250 MHz (1%). Fig. 2.35 shows the E-plane and H-plane radiation pattern. The E-plane exhibits a broad beam, closely centered at boresight with low sidelobe levels. The H-plane displays a narrow beam coverage centered at boresight, with a low SLL of -28.2 dB. These radiation characteristics are well suited to the radar requirements, providing broad angular coverage in the E-plane and narrow angular coverage with strong sidelobe suppression in the H-plane, which can help reduce unwanted clutter and interference while maintaining directional sensitivity.

2.6.3.5 Corporate Feed Array Network

Corporate feed networks have been extensively investigated in the literature due to their ability to provide precise amplitude and phase control of array elements. Implementations have been reported using microstrip-line insert-fed rectangular patch arrays [27, 28] as well as aperture-coupled configurations [29]. Among these, the four-element corporate-fed rectangular patch array

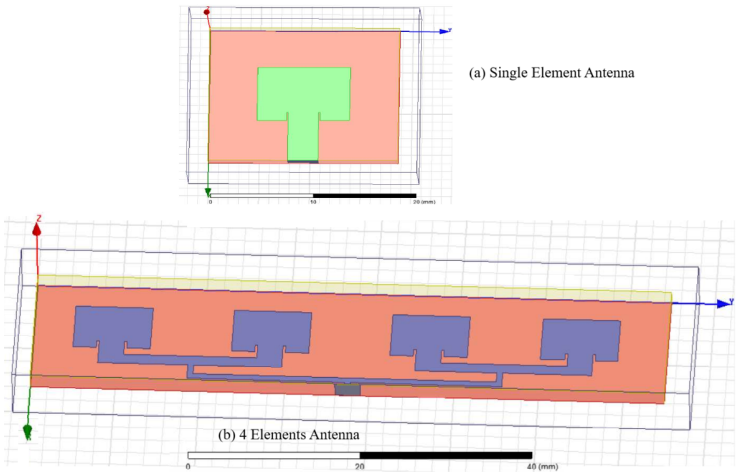
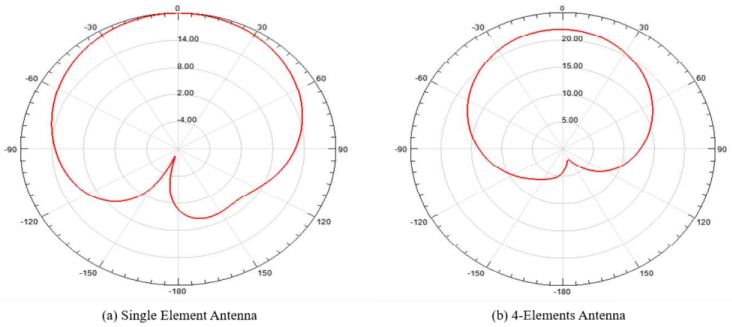


Figure 2.36: Antennas geometry [29]

reported in [29] was selected for detailed evaluation because sufficient design and performance information was provided to assess its suitability for the MIMO radar system.

A single rectangular element measuring 6.42 mm in width and 9.13 mm in length was first designed using a microstrip line feed as shown in 2.36(a). This element was subsequently replicated to form a 1×4 linear array antenna fed by a corporate network, as illustrated in 2.36(b). In a corporate-fed array, the input power is distributed to each radiating element through a hierarchical network of power dividers. For this four-uniform-element array, the feed network consists of two stages of power dividers [29]. The input signal is first divided into two equal-power branches. Then each branch is further divided, yielding four equal-amplitude outputs that excite the antenna elements. The feed paths are designed to have equal electrical lengths, ensuring that all elements are excited in phase. Consequently, each element receives approximately one-quarter of the input power, resulting in a uniform amplitude and phase distribution across the array. A key advantage of this architecture is the ability to control the excitation amplitude of each element, thereby tailoring the radiation pattern to specific requirements. This is achieved by adjusting the dimensions of the power-divider branches, which determine the power delivered to each antenna element, while the excitation phase can be controlled by modifying the electrical lengths of the feed lines. Consequently, corporate-feed networks offer a high degree of flexibility for array pattern synthesis compared with series-fed structures.



(a) Single Element Antenna (b) 4-Elements Antenna

Figure 2.37: Radiation pattern at 10 GHz [29]

The 1×4 antenna has an operational frequency of 8.2 GHz and a BW of 1.2 GHz 15%. The compactness of the feed network is a critical consideration for integration into the MIMO radar array [29]. The rectangular patch element has a width of 6.42 mm (0.18λ); however, the dimensions of the feed lines are not reported in the original work, limiting accurate reproduction of the design. Based on the published antenna layout, the overall width of the four-element array can be approximated as 11 mm (0.48λ). This dimension satisfies the spacing constraints of integration into the MIMO RX array. Nevertheless, the original design employs an edge-mounted feed, which would require modification to a coaxial-probe feed to meet the fabrication requirements of the corporate network MIMO RX array.

The radiation pattern at 10 GHz of the single patch antenna exhibited a relatively broad radiation pattern with moderate directivity, shown in Fig. 2.37(a), while the array produced a narrower main beam and higher gain due to the increased effective aperture, illustrated in (b). Both radiation pattern presents a broadside peak main beam centered at $\approx 0°$.

The $|S_{11}|$ simulation results showed that the addition of the 1×4-elements corporate-feed network array altered the single element antenna characteristics, reducing the resonant frequency from 13.96 GHz to 8.22 GHz and increased the impedance bandwidth from 1.16 GHz to 1.2 GHz for the single element and array, respectively. Since the patch dimensions remained unchanged between the single-element and array configurations, these shifts demonstrate that the feed network, element loading, and mutual coupling substantially affect the complete array response. Although the corporate-feed architecture provides excellent amplitude and phase control, its multiple power-divider stages increase physical complexity and occupied area compared with series-fed alternatives. Nevertheless, the estimated width of approximately 0.48λ suggests that the

design remains sufficiently compact for integration in an array.

2.6.3.6 Comparison of the Feed Network Designs

For the subarray antenna for the MIMO radar, the patch and feed network footprint is particularly important because the subarray will be integrated into a 2D planar antenna. At the same time, sufficient control of the amplitude and phase distributions is required to obtain the desired directional radiation pattern and sidelobe performance. The design needs to be able to be modified to 5.75 GHz with 200 MHz BW. The comparison therefore indicates that the selection of the feed architecture involves a trade-off between feed-network compactness, excitation control, impedance matching and fabrication simplicity. Table 2.6 summarizes these principal characteristics of the candidate feed-network architectures considered for the subarray antenna.

Table 2.6: Comparison of candidate feed-network architectures for the TX subarray

Network	f_0 **(GHz)**	**Array footprint** $L \times W$ **(mm)** $(\lambda \times \lambda)$	BW **(GHz)**	**Amplitude and phase control**
1×5 series-fed [23]	62	14.96×1.8 $(3.09\lambda \times 0.37\lambda)$	9.7% (6 GHz)	Patch-width tapering and inter-element feed-line lengths
1×5 matching-in-step [25]	5	192.32×34.4 $(3.21\lambda \times 0.57\lambda)$	2.8% (0.14 GHz)	Stepped feed widths and inter-element feed-line lengths
1×4 series-fed with branches [14]	26	36×5.1 $(3.12\lambda \times 0.44\lambda)$	14% (4 GHz)	Coupling branches, quarter-wave transformers, and equal electrical path lengths
1×12 and 1×8 comb-line [26]	24	135×4.34 $(10.8\lambda \times 0.35\lambda)$	$> 1\%$ (> 0.25 GHz)	Stub- or feed-line-width tapering and longitudinal element spacing
1×4 corporate-fed [29]	8.22	NR×11 (NR×0.48)	15% (1.2 GHz)	Power-divider ratios and individual feed-path lengths

NR: not reported.

In this comparison, fabrication simplicity is assessed based on the number of substrate layers, required layer-alignment accuracy, number of feed-network

features and junctions, and sensitivity of critical dimensions to manufacturing tolerances. The conventional series feed offers the simplest physical implementation because all elements are connected sequentially by a single continuous transmission-line path. It requires fewer branches, junctions and matching sections. Conversely, the aperture-coupled architecture presents the greatest fabrication sensitivity since it requires two substrate layers and accurate alignment of the feed network, coupling apertures, and radiating patches. The matching-in-step and corporate-fed architectures occupy an intermediate position, with the former requiring several precisely dimensioned matching sections. The latter requires accurate fabrication of the power-divider line widths and feed-path lengths to maintain the intended impedance, power division, and phase distribution.

The corporate-fed architecture offers the greatest design flexibility for independent amplitude and phase control because the power-divider ratios and feed-path lengths can, in principle, be designed separately. Although the reviewed implementation employed uniform excitation, the architecture is well suited to non-uniform array synthesis for sidelobe reduction and beam shaping. This flexibility is advantageous for shaping the elevation pattern and reducing sidelobes. In comparison, the amplitude and phase distributions of series-fed and comb-line arrays are coupled to the sequential extraction of power, element loading, and electrical spacing along the feed line. The matching-in-step series feed improves impedance matching and demonstrates sidelobe suppression through its tapered excitation distribution; however, the matching sections introduce additional dimensions that must be adjusted. The aperture-coupled series feed with branches also permits amplitude and phase control through its coupling branches and electrical path lengths. However, the publication did not report sufficient radiation-pattern metrics, such as sidelobe level and beamwidth, to enable a complete comparison with the other candidate architectures.

All candidate feed networks use radiating elements with relatively simple geometries that can be dimensionally scaled to meet the target frequency of 5.75 GHz. However, retuning the radiating elements alone is insufficient because the feed network, element spacing, and impedance-matching sections must also be adjusted as part of the complete array to improve the antenna's bandwidth and impedance matching to the radar requirements,

Since the subarray antenna must be integrated into a 2D planar MIMO array, feed-network width is a critical design constraint. Series-fed, series-fed with coupling branches, and comb-line architectures generally provide the smallest feed-network widths because power is distributed along a single main transmission line, resulting in narrow structures that facilitate integration into

a planar array. Corporate-feed networks typically require a larger feed-network width because additional routing space is needed for the power dividers, feed branches, and feed transitions.

Based on the preceding comparison, the series-fed network with coupling branches was selected because it combines a narrow feed-network width with sufficient flexibility to tailor the excitation amplitudes and phases through the coupling branches, transformer sections, and electrical path lengths. Conventional series-fed, matching-in-step, and comb-line designs were not retained because their excitation and matching characteristics are more closely coupled to the radiating-element and main-feed geometries, limiting their adaptability to the required subarray configuration. Although the corporate-feed architecture offers greater excitation control, its wider power-divider network and probe placement complicate integration into the planar MIMO array and increase fabrication complexity.

3 Proximity-Coupled Series-Fed Circular Patch Subarray Antenna

This chapter presents the design process of a 3-element proximity-coupled series-fed circular patch antenna for the intended MIMO radar applications. The antenna design was developed by integrating various antenna techniques and full-wave electromagnetic simulations. The antenna was designed around a center frequency of 5.75 GHz, which lies within the $5.25 - 5.925$ GHz frequency range allocated for radar operation. Within this range, the antenna must provide an impedance bandwidth of approximately 200 MHz, corresponding to a fractional bandwidth of 3.5% at 5.75 GHz. Section 3.1 presents the antenna geometry and dimensions. The design process included selecting the substrate material in Section 3.2, determining the initial circular patch dimensions in Section 3.3, and designing the series-fed network in Section 3.4. The full-wave simulation process and the challenges associated with improving the integrated proximity-coupled series-fed antenna are presented in Section 3.5. Finally, Section 3.6 presents the resulting antenna and evaluates its performance against the design requirements, including operating frequency, impedance bandwidth, radiation pattern, beamwidth, sidelobe level, and gain.

3.1 Subarray Antenna Geometry and Dimensions

The antenna consists of three radiating elements arranged in a linear array. Fig. 3.1 shows an exploded view. Three radiating patches are printed on the upper surface of the upper substrate. The feed network lies between the two substrates and couples energy electromagnetically to the patches through proximity coupling. A continuous copper ground plane forms the bottom layer.

Both substrates are Rogers RO3003™ laminate with a height of 0.762 mm

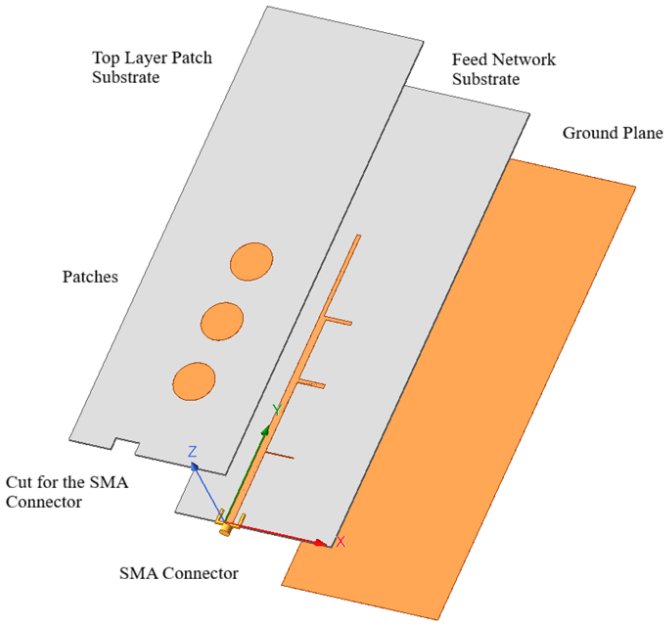


Figure 3.1: TX antenna model exploded view

and relative permittivity $\varepsilon_r = 3.0$. Section 3.2 discusses the material properties and substrate selection. The milling equipment at RMC constrained the overall antenna dimensions. The substrate dimensions are $L = 190$ mm and $W = 65$ mm, making the antenna compatible with the fabrication-area constraints of the LPKF milling machine.

The top layer contains the radiating elements and is shown in Fig. 3.2(a). To accommodate the edge-mount coaxial connector, a 5 mm long by 10 mm wide cut was made on the top substrate. The feed network array is shown in Fig. 3.2(b). Part of each coupling branch is positioned beneath its corresponding patch to control electromagnetic coupling, power distribution and phase excitation of the three elements. The patch, array-spacing, feed-network, and coupling-branch parameters are identified in Fig. 3.2(b), with the corresponding dimensions listed in Table 3.1.

3.2 Substrates

The substrate's electrical and physical properties strongly influence the performance of a microstrip patch antenna. Important parameters include the

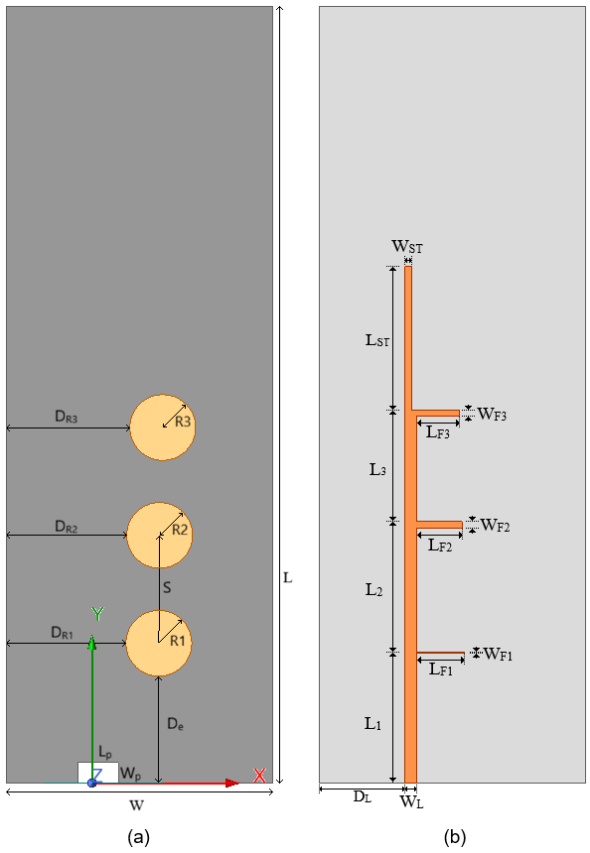


Figure 3.2: Antenna dimensions (a) top patches layer (b) feed network layer

relative permittivity ε_r, substrate thickness h, and dielectric loss tangent. These parameters influence the antenna impedance bandwidth, radiation efficiency, physical dimensions, and stored electromagnetic energy.

A resonant microstrip patch antenna inherently exhibits a narrow impedance bandwidth. Increasing the substrate thickness generally enhances bandwidth by reducing the antenna quality factor Q, but reduces radiation efficiency, as shown in Fig. 3.3. Conversely, reducing the substrate thickness generally results in a narrower impedance bandwidth. The relative permittivity also plays an important role in determining the antenna impedance bandwidth and radiation efficiency. Higher-permittivity substrates confine more of the electromagnetic field within the dielectric, increasing stored energy and, consequently, the antenna's quality factor. Increasing substrate permittivity generally re-

Table 3.1: Final antenna dimensions

Parameter	Dimension (mm)	Parameter	Dimension (mm)
Top patch layer, Fig. 3.2(a)			
L	190	W	65
R_1	8.075	D_{R1}	29.238
R_2	8.075	D_{R2}	29.438
R_3	8.075	D_{R3}	30.188
D_e	26.468	S	26.468
L_p	5	W_p	10
Feed network layer, Fig. 3.2(b)			
W_L	2.929	D_L	20.947
L_1	32.1305	L_2	32.0135
L_3	27.263		
L_{ST}	35.4	W_{ST}	1.614
L_{f1}	11.7	W_{F1}	0.325
L_{F2}	11	W_{F2}	1.68
L_{F3}	10.35	W_{F3}	1.37

duces impedance bandwidth and radiation efficiency, as illustrated in Fig. 3.3. Furthermore, high-permittivity substrates tend to reduce radiation efficiency because a greater fraction of the electromagnetic energy is stored within the dielectric rather than radiated into free space [30]. Therefore, substrate selection requires a compromise between relative permittivity, antenna thickness, impedance bandwidth, and radiation efficiency. The relative permittivity of laminates typically ranges from 2 to 12 [5].

Based on these considerations, Rogers RO3003™ laminate was selected as the substrate material. RO3003™ is a ceramic-filled PTFE composite with a relative permittivity $\varepsilon_r = 3.0$ and a dissipation factor of $\tan\delta = 0.0010$ at 10 GHz [31]. The selected substrate thickness is 0.762 mm with 35 µm (1 oz) copper cladding on both sides. The combination of its moderate relative permittivity and thickness was selected to achieve a suitable balance between impedance bandwidth and radiation efficiency. Compared with commonly used FR-4 substrates, RO3003™ offers significantly lower dielectric losses,

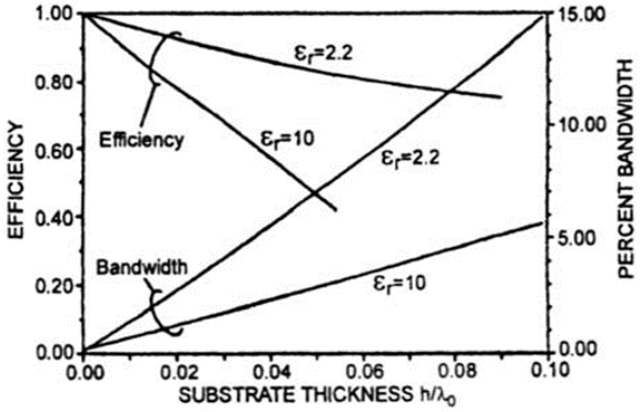


Figure 3.3: Effect of substrate thickness and dielectric constant on the impedance bandwidth ($VSWR < 2$) and radiation efficiency [30]

improving radiation efficiency and reducing insertion loss. Furthermore, to reduce fabrication costs associated with the antenna prototypes, a lower-cost Rogers RO3003™ laminate was selected instead of more expensive reinforced laminates.

The antenna structure employs two RO3003™ substrate layers separated by a Rogers 2929 bondply adhesive film. The bondply has a thickness of 0.038 mm, a relative permittivity of approximately $\varepsilon_r = 2.94$, and a loss tangent below 0.003 [32]. Its dielectric properties closely match those of the RO3003™ substrates, while its very small thickness minimizes its influence on the antenna's electromagnetic behaviour. Full-wave simulations performed in ANSYS HFSS showed negligible changes in antenna performance when the bondply layer was included.

3.3 Circular Patch

The initial radius a of the circular patch was determined using the cavity-model formulation and is expressed as [5, 21]:

$$a = \frac{F}{\left\{1 + \frac{2h}{\pi\epsilon_r F}\left[\ln\left(\frac{\pi F}{2h}\right) + 1.7726\right]\right\}^{\frac{1}{2}}} \tag{3.1}$$

where the factor F is defined as:

$$F = \frac{8.791 \times 10^9}{f_r\sqrt{\epsilon_r}}. \tag{3.2}$$

In (3.1), the parameters h and ϵ_r denote the substrate thickness and relative permittivity, respectively, and the radius a yields results in centimetres. In (3.2), the resonant frequency f_r is expressed in Hz. Since proximity-coupled feeding is used, h is the sum of both substrates' heights, so 1.524 mm. Because the electromagnetic fields fringe outward beyond the physical edge of the patch, the patch appears electrically larger than its physical dimensions. This effect is represented by an effective radius a_e, which is greater than the physical radius a. The effective radius accounts for the fringing-field extension and depends on the substrate thickness and relative permittivity [5].

$$a_e = a\left\{1 + \frac{2h}{\pi a \epsilon_r}\left[\ln\left(\frac{\pi a}{2h}\right) + 1.7726\right]\right\}^{\frac{1}{2}} \tag{3.3}$$

The resulting a is 8.81 mm and a_e is 8.83 mm, and is used as the initial patch radius for the full-wave simulations improvement in ANSYS HFSS. The resulting subarray physical radius is 8.075 mm, which is closer to a, reflecting the electromagnetic behavior of the complete antenna structure, coupling to the proximity-fed network, and the effects of the surrounding geometry.

3.4 Series-Fed Array Topology and Design

As discussed in Section 2.6.3.6, the three patch elements are excited using a series-feed with a coupling-branch array configuration. In this array, the elements are coupled sequentially through open-ended feed lines branching perpendicular from the main line and running parallel under the patches, as shown in Fig. 3.4. Proximity coupling was used instead of aperture coupling because of its ability to reduce back radiation, and fabrication simplicity [30, 33]. An open-ended stub located at the end of the feed network was used to achieve impedance matching and minimize reflections.

The radiation characteristics of an antenna array are determined by the superposition of the fields radiated by each array element, weighted by excitation amplitudes and phases. In equally spaced broadside arrays, the excitation distribution is typically symmetric about the array center [34], and all elements must maintain the same phase to ensure constructive interference in the broadside radiation direction.

To control the trade-off between main-beam width and sidelobe level, appropriate amplitude tapers can be applied to the array elements while maintaining the required phase distribution. Low sidelobe levels are particularly important for radar applications because radiation outside the main beam can contribute to unwanted responses from off-axis targets, clutter, and reflections. Therefore,



Figure 3.4: Series-fed with coupling branches

sidelobe suppression can reduce unwanted detections and help mitigate false target identification and ghost responses caused by strong reflected signals arriving through sidelobe directions. However, a low sidelobe level increases main beam width which decreases angular resolution. Consequently, a trade-off must be established between sidelobe suppression and main-beam width, with the desired excitation taper selected to provide sufficient sidelobe reduction while maintaining the angular resolution required by the radar system. For this reason, a Dolph–Chebyshev taper was chosen since for a specified sidelobe level, this distribution minimizes the main-beam width while preserving controlled sidelobe behaviour, providing an optimal compromise between beamwidth reduction and sidelobe suppression [34–37]. The Dolph–Chebyshev taper, introduced by Charles Dolph in 1946, employs Chebyshev polynomials to determine the element excitation weights such that all sidelobes are equal in magnitude, producing an equal-ripple sidelobe response [36].

A three-element ($N = 3$) Dolph–Chebyshev amplitude taper was implemented to satisfy the radar sidelobe requirements while maintaining a narrow main beam. The choice of three elements represents a practical compromise

between radiation-pattern control and the complexity of the feeding network. The branching feed is a highly coupled electromagnetic structure in which changes to the overlap, branch width, branch position, and feed dimensions can simultaneously affect the excitation amplitude and phase of multiple patches, as well as the input impedance and operating bandwidth. Increasing the number of array elements would introduce additional coupled branches and design variables, substantially increasing the number of electromagnetic interactions and the number of simulations required for iterative tuning steps. A three-element configuration therefore provides sufficient degrees of freedom to realize a symmetric amplitude taper while keeping the feed-network adjustment computationally manageable.

The excitation coefficients were determined using the MATLAB chebwin function for a three-element array [38]. For the radar application, a major-to-minor sidelobe ratio of at least 15 dB was specified, resulting in normalized excitation coefficients of approximately $0.72 : 1 : 0.72$, as shown in Table 3.2. As the sidelobe ratio approaches infinity, the Dolph–Chebyshev distribution converges toward a binomial distribution, producing normalized excitation coefficients of $0.5 : 1 : 0.5$ [5]. Consequently, any excitation taper within this range may be acceptable provided the resulting radiation pattern meets the beamwidth and sidelobe-level requirements of the radar system. Unlike larger arrays, where a specific amplitude distribution may be required to achieve a desired sidelobe level, a three-element array possesses limited degrees of freedom and can achieve similar radiation characteristics using a range of symmetric excitation tapers. Although the binomial distribution eliminates sidelobes entirely, it produces a broader main beamwidth, as shown in Fig. 3.5 for $R = 100$ dB. In contrast, the Dolph–Chebyshev taper, shown in Fig. 3.5 for $R = 15, 20, 30$ and 50 dB, provides controlled sidelobe suppression while preserving a narrower beamwidth suitable for radar applications.

To achieve a symmetric amplitude distribution while maintaining equal phase across the 3 elements, the coupling overlap, branch widths, and branch positions were varied in ANSYS HFSS. Section 3.5 further discusses the tuning steps and the final excitation taper.

3.5 Overall Subarray Tuning Steps

Although the circular patches, substrate configuration, feed network, coupling branches, and impedance-matching stub were initially designed separately, their electromagnetic interaction required determining the final dimensions through iterative full-wave simulations in ANSYS HFSS. The subarray geometry

Table 3.2: Normalized excitation coefficients for a 3-element array at different sidelobe ratios

Major-to-Minor Sidelobe Ratio (dB)	**Element 1**	**Element 2**	**Element 3**
15	0.7163	1	0.7163
20	0.6111	1	0.6111
30	0.5327	1	0.5327
50	0.5032	1	0.5032
100	0.5000	1	0.5000

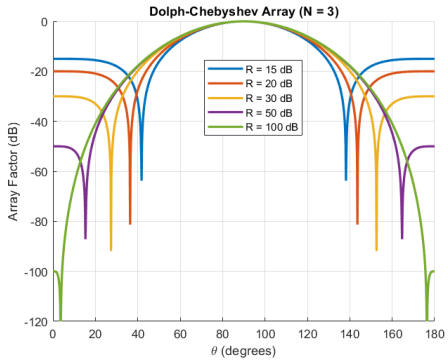


Figure 3.5: Array factor for 3-elements with different major-to-minor sidelobe ratio

parameters were adjusted as an integrated electromagnetic structure rather than as a set of independent components. The primary improvement objectives were to achieve the required operating frequency and impedance bandwidth, ensure adequate input impedance matching, and produce the desired radiation-pattern coverage through amplitude and phase excitation across the three radiating elements.

The improvement process began by adjusting the substrate, circular-patch, and feed-network dimensions to establish the initial resonant behaviour of the radiating elements. First, the antenna parameters were set up for screening and optimization, using an adaptive single objective function, to search for results with impedance matching below -20 dB at the desired frequency. Using the parameters of all results that met this criterion, the surface current was

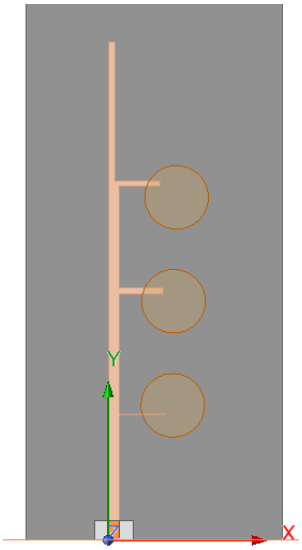


Figure 3.6: Feed network and patch alignment

evaluated at the center of each of the three circular patches. The magnitude and phase of the surface current were extracted and considered in phase when within 5°. The parameters of the best result were then used as the initial antenna design for parametric analysis of each antenna parameter.

The branch geometries and positions control impedance matching, coupled power and phase of each element. Figure 3.6 shows the alignment between the feed network and the circular patches. In particular, the overlap between a branch and its corresponding patch primarily influenced coupling strength and, consequently, excitation amplitude, while branch width affected both excitation amplitude and feed-line impedance. The feed-branch position and geometry also influenced the phase of the coupled excitation. Because the proximity-coupled branches simultaneously controlled power distribution and formed part of the impedance-matching network, these parameters could not be adjusted independently. A change intended to adjust the amplitude or phase taper could simultaneously alter the feed-network impedance, resonant frequency, bandwidth, and excitation of the other elements. Consequently, the patch radius was retained as an improvement parameter because it provides a direct means of controlling the resonant frequency, as described by (3.1). Therefore, it was used to compensate for frequency shifts introduced by modifications to the feed network during the tuning process.

The feed-network geometry, including the coupling branches and impedance-

matching stub, was then adjusted to achieve the desired excitation distribution while maintaining adequate impedance matching. The branch dimensions and positions were adjusted to control the excitation amplitude and phase of each radiating element, whereas the stub dimensions were used to fine-tune the antenna input impedance. This stub provided an additional degree of freedom for controlling the overall impedance of the array without requiring each feed branch to be individually impedance matched. The improved stub length remained approximately constant during the later stages of the tuning steps, whereas the stub width was adjusted as required to recover the desired input impedance. At the operating frequency of 5.75 GHz, the improved open-ended stub was 35.4 mm long by 1.614 mm wide.

Because the proximity-coupled feed network and radiating elements form a strongly coupled electromagnetic structure, changes to a single parameter often affected multiple antenna characteristics simultaneously. As a result, the tuning process was iterative rather than sequential. Parametric analyses were repeated until the excitation amplitudes and phases satisfied the desired taper, while the antenna simultaneously met the required operating frequency, impedance bandwidth, and input matching requirements.

3.6 Antenna Simulation Result and Discussion

At 5.736 GHz, the subarray has overall dimensions of approximately 2.43λ long by 0.47λ wide. The relatively compact width of 0.47λ allows the subarrays to be placed side by side along their width to form the 2D planar antenna array. The final coefficients are in phase, with amplitudes of approximately $0.61 : 1 : 0.61$, corresponding to a Dolph–Chebyshev major-to-minor sidelobe ratio of 20 dB, which lies between the Dolph–Chebyshev and binomial distributions. This excitation provided a suitable compromise between sidelobe suppression, beamwidth, and implementation through proximity coupling.

The simulated reflection coefficient $|S_{11}|$ is shown in Fig. 3.7. The results show that the antenna resonates at 5.74 GHz with a $|S_{11}|$ of -23.1 dB. The simulated resonant frequency is 10 MHz below the 5.75 GHz design target, indicating close agreement with the intended operating frequency. The -10 dB impedance bandwidth extends from 5.66 to 5.84 GHz, corresponding to 180 MHz, or 3.14% relative to the center frequency. Although the simulated impedance bandwidth is slightly narrower than the 200 MHz SDR bandwidth, it covers the majority of the intended operating band and provides good impedance matching over the simulated frequency range. The reduced bandwidth prevents full utilization of the available radar spectrum and results in a

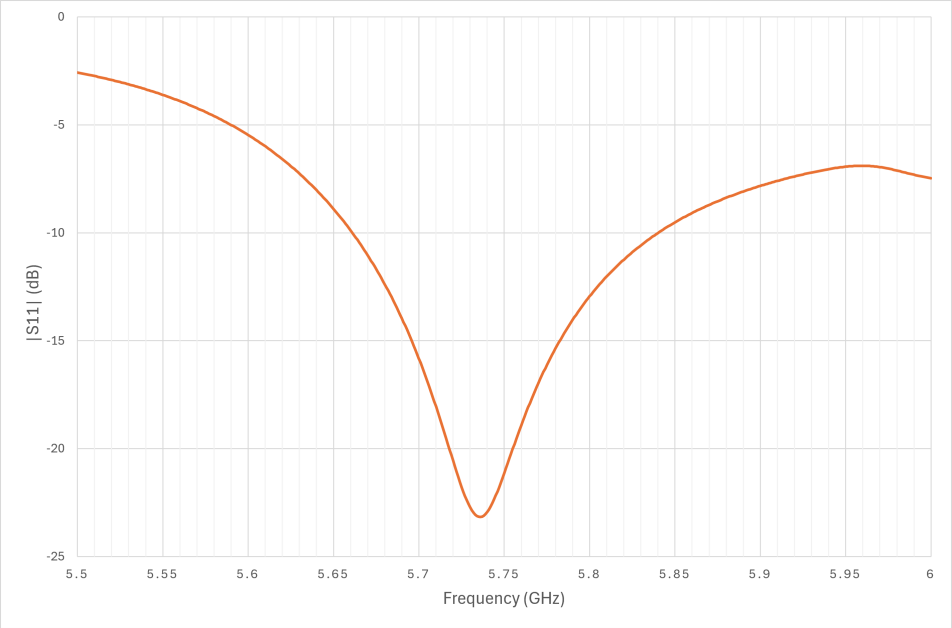


Figure 3.7: Simulated $|S_{11}|$ of the TX antenna

small reduction in range resolution from 75 cm to 83 cm.

Table 3.3 summarizes the simulated $|S_{11}|$ response in comparison with the design requirements.

Table 3.3: Comparison of simulated $|S_{11}|$ with design requirements

Parameter	**Design Spec.**	**Simulated**
f_0	5.75 GHz	5.736 GHz
Frequency range	$5.65 - 5.85$ GHz	$5.66 - 5.84$ GHz
f_0 and frequency range within radar band	Yes	Yes
BW	200 MHz	180 MHz
FBW	3.5%	3.14%

Fig. 3.8 shows the simulated co-polarized radiation patterns of the TX antenna in the E-plane (azimuth) and H-plane (elevation). Table 3.4 summarizes the simulated radiation pattern results in comparison with the design

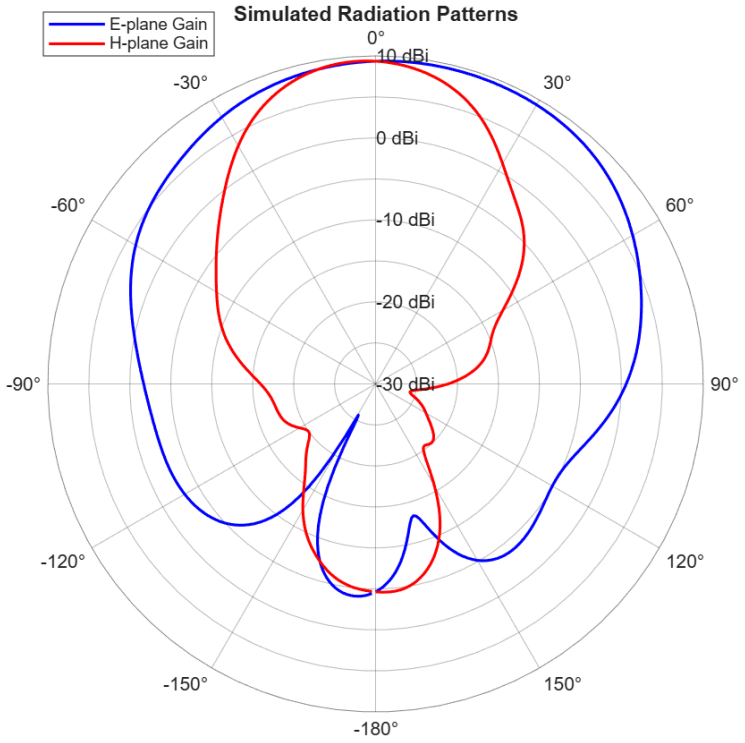


Figure 3.8: Simulated co-polarization of the TX antenna

requirements. The E-plane pattern provides broad forward radiation, with a peak gain of approximately 9.5 dBi occurring at 13°, with an $HPBW$ of approximately 97.4°. Although this 97.4° $HPBW$ result does not fall within the stated E-plane $HPBW$ requirement of $40° - 80°$, the broader main beam provides increased angular coverage within the forward 180° field of view. The H-plane pattern is relatively narrower than the E-plane. The simulated H-plane pattern has a peak gain of approximately 9.4 dBi near boresight with an $HPBW$ of approximately 40°. This value falls within the specified comparison range of $15° - 60°$. However, some radiation is also present in the backward direction for both principal planes. The F/B ratio for the E-plane is 14.7 dB and H-plane is 14 dB. The design specification requires minimizing back radiation with an optimal ratio ≥ 10 dB. In the final radar implementation, absorbing material or other hardware can be placed behind the antenna to reduce the effect of the backward radiation.

Table 3.4: Comparison of simulated radiation pattern parameters with design requirements

Parameter	**Design Spec.**		**Simulated**	
	E-plane	**H-plane**	**E-plane**	**H-plane**
Peak Gain (dBi)	–	–	9.5	9.4
Peak Angle °	–	–	13	−3
$HPBW$ (°)	$40-80$	$15-60$	97.4	40
Sidelobe level (dB)	≤ -15	≤ -15	None	None
F/B ratio (dB)	maximize	maximize	14.7 dB	14.0 dB

3.7 Comparison of the subarray with the Taoglas antenna

The improved subarray provides several improvements over the existing Taoglas UWB antenna while also exhibiting some limitations relative to the desired radiation-pattern requirements and bandwidth. Table 3.5 summarizes the principal differences between the two antenna designs. Overall, compared with the existing Taoglas antenna used in the RMC MIMO radar, the subarray provides substantially higher gain, directional radiation characteristics, improved front-to-back performance, and reduced susceptibility to clutter originating from the rear hemisphere. These improvements directly address several shortcomings of the current antenna configuration identified in Section 2.5.

Furthermore, the improved subarray antenna is specifically designed to operate at 5.75 GHz, whereas the existing Taoglas antenna exhibits a rejection band around 5.8 GHz intended to suppress WiFi signals. As a result, the Taoglas antenna cannot efficiently support radar operation around 5.75 GHz. Even at their respective center frequencies, the subarray shows a better impedance matching of -23.17 dB at 5.75 GHz, while the Taoglas reports an impedance of -12.92 dB at 5 GHz.

The most significant improvement is the increase in peak gain of the radiation pattern. The simulated subarray achieves peak gains of 9.5 dBi and 9.4 dBi in the E-plane and H-plane, respectively, compared with the $4-5$ dBi gain of the Taoglas antenna. This gain enhancement can increase the effective radiated power and improve radar detection range. In addition, the

Table 3.5: Comparison between the existing Taoglas FXUWB20 antenna and the improved subarray antenna

Parameter	**Taoglas FXUWB20**	**Improved Subarray**
Center Frequency	5 GHz	5.75 GHz
$\|S_{11}\|$	-12.92 dB @ 5 GHz	-23.17 dB @ 5.75 GHz
Bandwidth	Supports full 200 MHz radar channel	180 MHz
Peak Gain	$4 - 5$ dBi	$9.4 - 9.5$ dBi
Radiation Pattern	Omnidirectional	Directional
$HPBW$ (E-plane)	Omnidirectional	97.4°
$HPBW$ (H-plane)	Omnidirectional	40.0°
Forward Sidelobes	Not specified	No sidelobes observed
Front-to-Back Ratio	Low due to omnidirectional pattern	$14.0 - 14.7$ dB

improved subarray exhibits a directional radiation pattern, with no sidelobe in the forward coverage rather than the omnidirectional response of the Taoglas antenna. Having no sidelobes is beneficial for radar operation because it reduces the reception and transmission of energy in undesired directions, thereby limiting false detections and improving angular discrimination.

The subarray exhibits front-to-back ratios of 14.7 dB and 14.0 dB in the E-plane and H-plane, respectively, representing a significant improvement over the omnidirectional radiation characteristics of the currently employed Taoglas antenna. This reduction in back radiation reducing the likelihood of clutter and target ambiguities caused by signals arriving from behind the radar.

The principal disadvantage of the subarray is its reduced impedance bandwidth. The simulated bandwidth of approximately 180 MHz is slightly below the radar channel BW of 200 MHz and is narrower than the ultra-wideband response of the Taoglas antenna, which covers the full radar channel BW. Nevertheless, compared with the existing Taoglas antenna used in the RMC MIMO radar, the improved subarray antenna provides substantially higher gain, directional radiation characteristics, improved front-to-back performance, and reduced susceptibility to clutter originating from the rear hemisphere. These improvements directly address several shortcomings of the current antenna

configuration identified in Section 2.5.

4 2D Planar Array Antenna

First, to reduce computational time during the tuning steps, a 4-subarray planar antenna was designed. Then, four subarrays were added to form the 8-subarray planar array and simulated. The 4- and 8-subarray planar geometry and dimensions are specified in Section 4.1.

4.1 Planar Antenna Geometry and Dimensions

The 2D planar antenna consists of eight subarray antennas arranged in a planar configuration, providing eight independent RX channels and 24 radiating elements. Fig. 4.1 shows an exploded view of the antenna structure. The radiating patches are on the top layer, the feed network array is between the two substrate layers, and the ground plane is on the bottom layer. The 8-subarray planar array antenna comprises an 8×3-element planar antenna, where each 3-element subarray is excited through a single coaxial probe.

The geometry and dimensions of the subarray antenna are detailed in Section 3.1. Both substrates are the same Rogers RO3003™ laminate as the subarray, with a height of 0.762 mm and $\varepsilon_r = 3.0$. To accommodate the antenna within the available area of the LPKF milling machine, the overall antenna dimensions must not exceed 203 mm in length and 279 mm in width. The 8-subarray planar antenna dimensions are $L = 190$ mm and $W = 259$ mm, which are within the fabrication-area limits of the LPKF milling machine.

The spacing and locations of the subarrays are identified in Fig. 4.2, and Table 4.1 lists the corresponding dimensions. The parameter S controls the separation between adjacent subarrays, D_{R1} defines the clearance between the substrate edge and the first subarray, while W controls the overall substrate width and consequently the clearance between the last subarray and the substrate edge. These subarray spacing and distances are maintained from the corresponding 4-subarray configuration to the 8-subarray planar antenna.

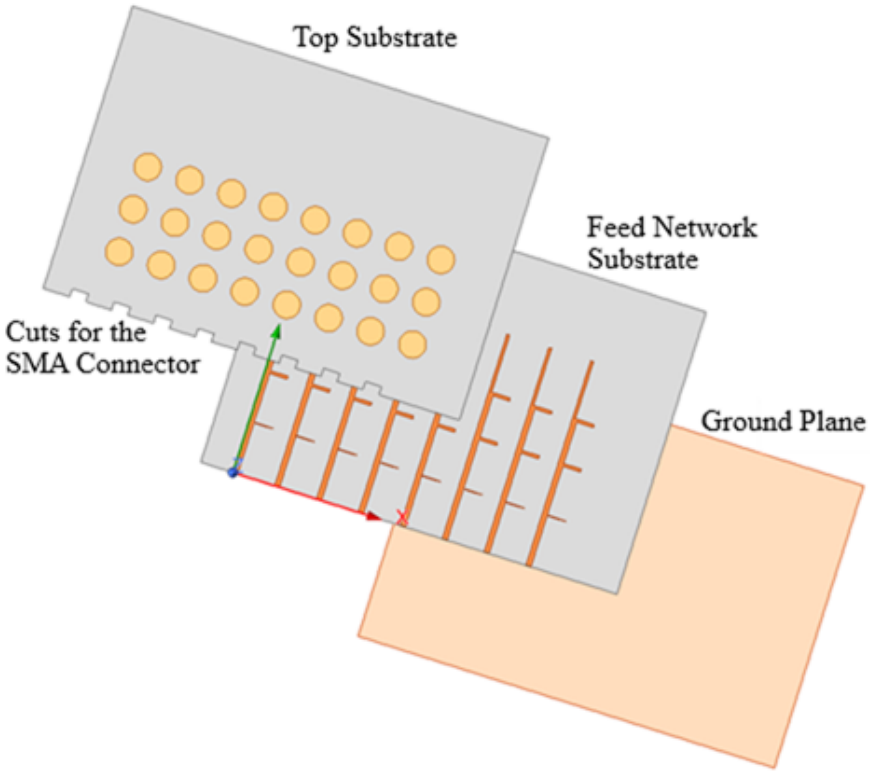


Figure 4.1: 8-array planar network feed layer

Table 4.1: Array planar antenna dimensions

Parameter	**Dimension (mm)**	**Parameter**	**Dimension (mm)**
D_{R1}	31.238	D_E	29.312
S	26.1	L	190

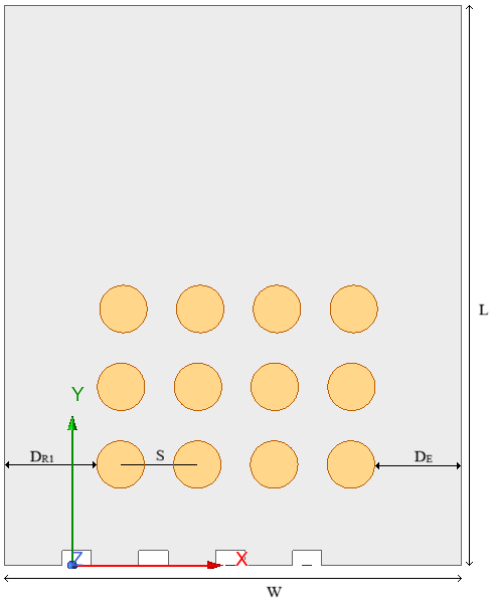


Figure 4.2: 4-subarray planar array top layer

4.2 4-Subarray Antenna Tuning Steps

Fig. 4.2 shows the three design parameters that were investigated. The parameters S, D_{R1} and W were varied to satisfy the design requirements listed in Section 2.6. Fig. 4.3 shows the resulting planar configuration, with the antenna displayed in transparency mode to show the relative positions of each subarray.

A $S = 26.1$ mm inter-element spacing of the planar antenna array was selected, corresponding to approximately 0.5λ at the design frequency of 5.75 GHz. This spacing matches the $\lambda/2$ inter-element spacing in the MIMO radar discussed in Section 2.6.1.3. Together with the $4d$ TX antenna spacing, this configuration forms all 64 unique virtual antennas.

A parametric investigation was conducted to determine suitable geometrical dimensions for the 2D planar array. The investigation focused primarily on the edge clearance D_{R1} and the width W dimension, while the inter-element spacing was maintained at 26.1 mm. The edge clearance was modified based on observations from the fabricated antenna. In the initial design, the available clearance around the antenna was relatively limited. During measurement of the fabricated antenna, fringing fields and edge diffraction

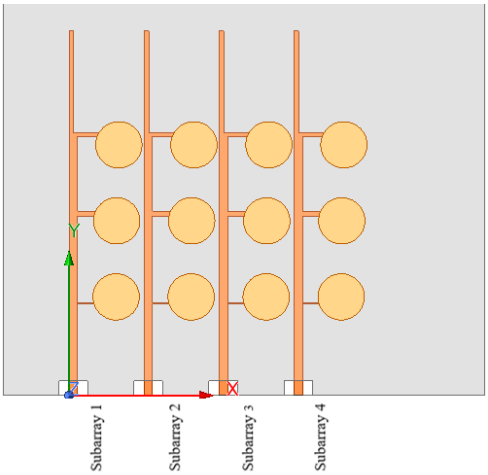


Figure 4.3: Planar array transparency

distortions were observed in the radiation pattern near the antenna boundary. This effect was not reproduced in the simulation model and, therefore, cannot be used in the parametric study. The edge clearance was increased to provide additional margin against fabrication-related edge effects. With $W = 155$ mm, $D_{R1} = 31.238$ mm provides an additional clearance of 2 mm between the edge and the subarray 1, and 9.697 mm between the subarray 4 and the edge. Furthermore, parametric study on D_{R1} was done by comparing $D_{R1} = 31.238$ and 33.238. This increase in edge clearance does not produce a substantial change in the impedance characteristics and radiation pattern characteristics within the investigated range. Therefore, the selection of 31.238 mm is primarily motivated by the fabrication observations and the need to provide additional radiation-pattern robustness, rather than by a significant improvement in simulated impedance performance.

The effect of the Width dimension was subsequently investigated by increasing W from 155 mm to 162.5 mm while maintaining the edge clearance at 31.238 mm and the inter-element spacing at 26.1 mm. Cases A and C were therefore compared to isolate the effect of increasing W from 155 mm to 162.5 mm. A slight decrease of approximately 5 MHz in BW was observed. The mutual coupling for all configurations remained below the design requirements of ≤ -15 dB. Increasing W improves the mutual coupling by an average of approximately 0.5 dB at 5.75 GHz. However, the E-plane and H-plane peak gain decreases by ≈ 0.1 dB. The F/B ratio improves slightly with the larger W, but the improvement is not sufficiently large to compensate for the

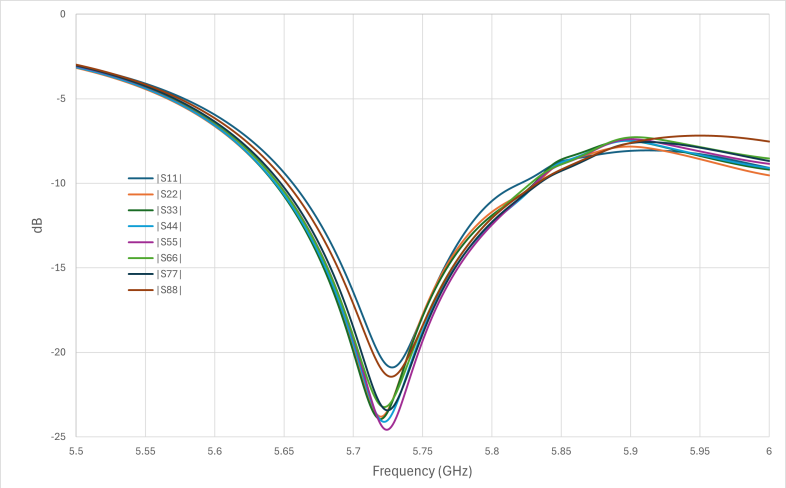


Figure 4.4: Input reflection coefficients

reduction in bandwidth and gain. Therefore, $W = 155$ mm was selected for the primary design because it provides a suitable compromise between impedance bandwidth, mutual coupling, gain, and radiation characteristics.

4.3 Simulated Result of the 8-Subarray Planar Antenna

Fig. 4.4 shows the simulated reflection coefficient $|S_{ii}|$ responses versus frequency for all eight subarrays of the planar antenna. Table 4.2 compares the resulting resonant frequencies, -10 dB frequency ranges, bandwidths, and fractional bandwidths with the design specification and the previously simulated 1×3-subarray. The resonant frequencies of the eight subarrays of the planar antenna remain closely grouped, ranging from 5.719 to 5.728 GHz, corresponding to a maximum variation of only 9 MHz. Compared with the standalone 1×3-subarray, the planar-antenna subarrays' resonant frequencies shifted downward by about $10 - 17$ MHz. Compared with the standalone subarray, the frequency ranges of the eight RX subarrays within the planar antenna shift downward by up to 20 MHz for both f_1 and f_2. This relatively small variation in impedance characteristics therefore indicates that the planar antenna maintains suitable frequency-overlap compatibility with the standalone subarray.

The simulated coefficient $|S_{ij}|$ responses versus frequency for all eight

Table 4.2: Comparison of simulated $|S_{11}|$ for all subarrays of the planar antenna with the design spec and the simulated subarray

Subarray i	f_0 **(GHz)**	**Frequency range (GHz)**	BW **(MHz)**	FBW (%)
Design spec.	5.75	$5.65 - 5.85$	200	3.5
1×3-element subarray	5.736	$5.66 - 5.84$	180	3.14
Subarray 1	5.728	$5.656 - 5.821$	164.4	2.87
Subarray 2	5.720	$5.643 - 5.832$	189.0	3.30
Subarray 3	5.719	$5.643 - 5.831$	187.6	3.28
Subarray 4	5.722	$5.644 - 5.832$	188.3	3.29
Subarray 5	5.724	$5.646 - 5.831$	185.7	3.24
Subarray 6	5.722	$5.646 - 5.828$	182.4	3.19
Subarray 7	5.725	$5.648 - 5.834$	186.6	3.26
Subarray 8	5.727	$5.652 - 5.833$	180.8	3.16

subarrays of the planar antenna are shown in Fig. 4.5. The mutual coupling between adjacent subarrays was evaluated at three reference frequencies: $f_0 = 5.72$ GHz, $f_1 = 5.6473$ GHz and $f_2 = 5.83$ GHz. Across these reference frequencies for all seven pairs, the coupling levels range from -18.19 to -22.57 dB. All adjacent subarray pairs satisfy the design requirement of a mutual-coupling level ≤ -15 dB.

Fig. 4.6 shows the radiation characteristics of the resulting 8-subarray planar array when all ports are uniformly excited in-phase to produce a broadside pattern. The polar representation shows the angular distribution of the radiated field in the principal planes, while the corresponding Cartesian representation in Fig. 4.7 provides a more convenient view for evaluating beamwidth and relative sidelobe levels. Table 4.4 summarizes the simulated radiation-pattern parameters. The simulated peak gains are approximately 17.80 dBi in the E-plane and 18.05 dBi in the H-plane. The main beam is directed at 0° in the E-plane and approximately -6° in the H-plane, indicating a small pointing offset in the latter plane. The simulated $HPBW$ is approximately 13.6° in the E-plane and 39.3° in the H-plane. The H-plane beamwidth should provide the required angular coverage while limiting floor and ceiling clutter.

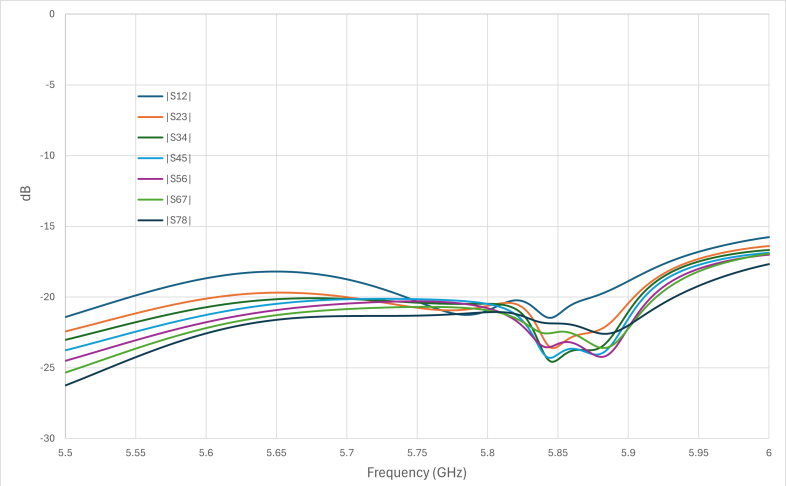


Figure 4.5: Simulated mutual coupling of each subarray of the planar antenna

Table 4.3: Comparison of simulated mutual coupling of each subarrays of the planar antenna

Subarray ij	$\|S_{ij}\|$ **at** f_0 **(dB)**	$\|S_{ij}\|$ **at** f_1 **(dB)**	$\|S_{ij}\|$ **at** f_2 **(dB)**
Design spec.	≤ -15	≤ -15	≤ -15
12	-19.35	-18.19	-20.53
23	-20.33	-19.69	-21.23
34	-20.25	-20.18	-21.89
45	-20.12	-20.51	-22.34
56	-20.35	-20.96	-22.57
67	-20.75	-21.32	-22.07
78	-21.34	-21.65	-21.54

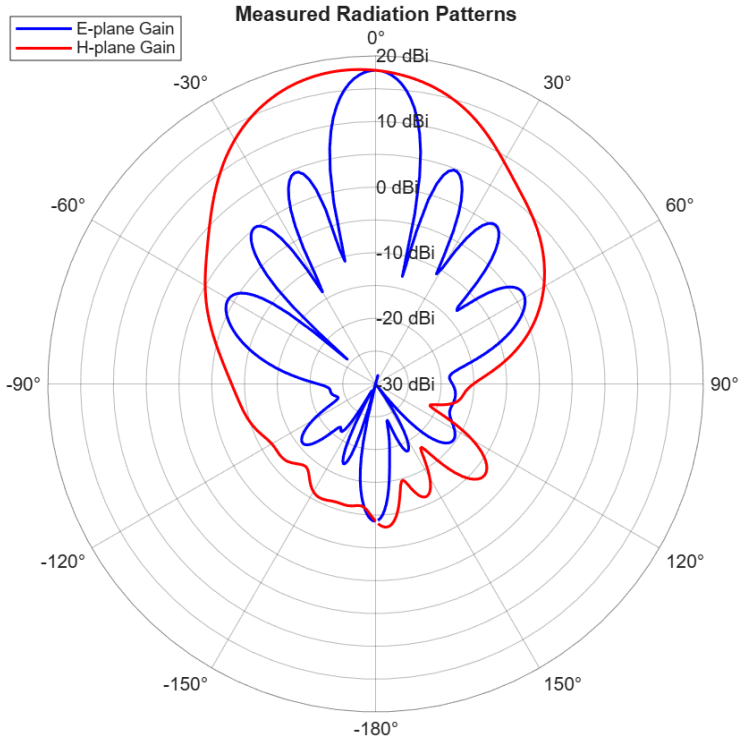


Figure 4.6: Polar radiation pattern of the 8-subarray planar array antenna

The F/B ratios are approximately 26.9 dB and 27.1 dB in the E- and H-planes, respectively. Both values exceed the 20 dB design specification, indicating effective suppression of radiation toward the rear of the array. The E-plane exhibits a maximum sidelobe level of approximately −13.1 dB in the forward radiation coverage, which is consistent with the sidelobe level of a uniformly excited, in-phase linear array. Its far-field radiation pattern is the Fourier transform of a rectangular aperture distribution and exhibits a first sidelobe at approximately −13 dB [5].

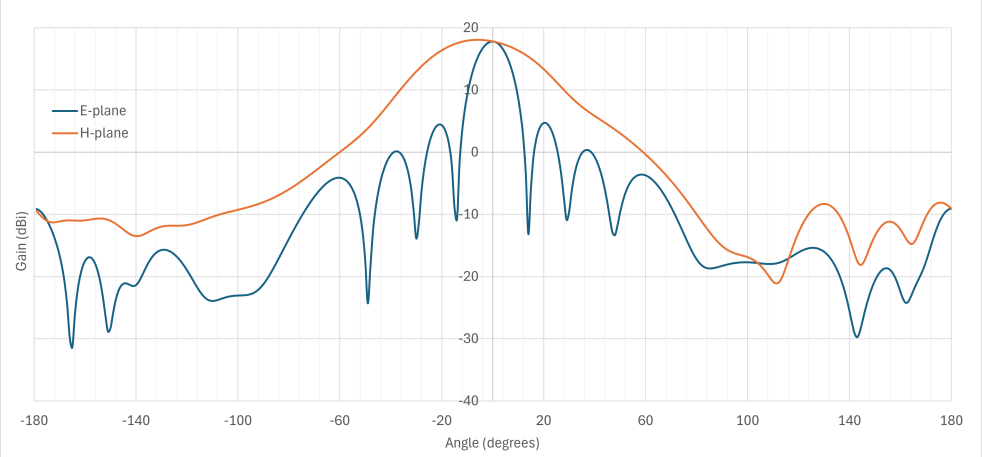


Figure 4.7: Cartesian radiation pattern of the 8-subarray planar array antenna

Table 4.4: Comparison of the simulated radiation pattern parameters of the 8-subarray planar array antenna with the design specifications

Parameter	**Design Spec. Both Plane**	**E-plane**	**H-plane**
Peak Gain (dBi)	-	17.80	18.05
Peak Angle (°)	-	0	-6
$HPBW$ (°)	-	≈ 13.6	≈ 39.3
Forward Sidelobe Level (dB)	-	≈ -13.1	none
F/B Ratio (dB)	maximize, ≥ 20	26.9	27.1

5 Experimental results

This chapter presents the experimental results and their analysis, and consists of three sections. Section 5.1 describes the subarray antenna fabrication procedure. Section 5.2 details the experimental setup. Section 5.3 presents and analyzes the measurement results.

5.1 Fabrication Procedure

The subarray antenna was fabricated using Rogers RO3003™ laminates, that have copper cladding on both sides [31]. An LPKF ProtoMat S104 PCB prototyping machine was used to remove the unwanted copper. A width of 10-mm-wide by 5-mm-long opening was then cut in the upper laminate to provide access for soldering the probe connector. A Rogers 2929 bondply layer was subsequently cut to match the laminate dimensions, with the same cut for the probe. A bondply layer was placed between the two RO3003™ laminates to form the proximity-coupled structure. Following the manufacturer's recommendations, pressure was applied during the curing and cooling processes [39]. Since a 400-PSI vacuum-assisted press was not available at RMC, the laminate stack was clamped between two steel plates with bolts to provide compression. The assembly was placed in an oven and heated from room temperature to 200°C; the temperature was maintained for $60 - 90$ minutes, then the assembly was left to cool overnight. After curing, the clamping plates were removed, and a 50 Ω end-launch SMA connector was soldered to the antenna edge at the cutout location. Fig. 5.1 shows the (a) top and (b) bottom views of the fabricated subarrays.

Several fabrication challenges were encountered during the milling process. Due to the relatively soft PTFE-based substrate, multiple milling passes were often required to completely remove the unwanted copper, as shown in Fig. 5.2(a). Consequently, approximately 40% of the fabricated laminates were rejected due to inadvertent removal of portions of the feed network or radiating



Figure 5.1: Fabricated subarrays

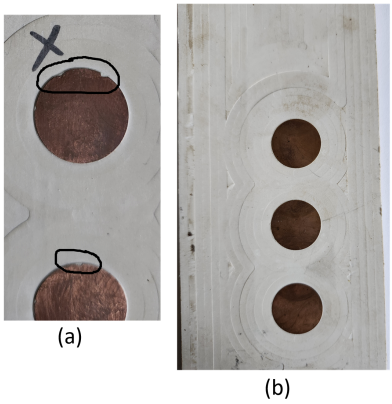


Figure 5.2: Milling issues during fabrication

patch. In some of the accepted laminates, small amounts of substrate material were also inadvertently removed during milling as shown in Fig. 5.2(b). For future designs fabricated on this machine, substrates with woven fibreglass reinforcement are recommended to improve milling during machining.

Additional difficulties arose during the bonding process. The uncured thin bondply film is fragile and occasionally tore when its protective backing was removed. Furthermore, a non-uniform pressure distribution during curing led to inconsistent bonding quality, resulting in a few antennas being rejected.

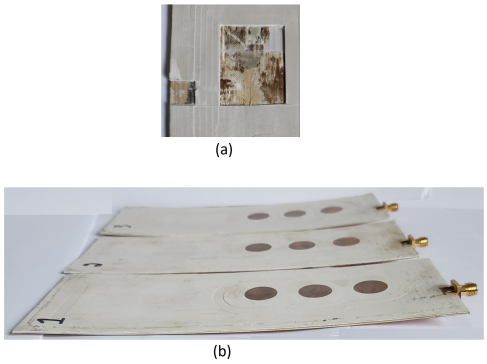


Figure 5.3: Bonding issues during fabrication

Fig. 5.3(a) shows a rejected antenna with a section of the substrate removed, revealing non-uniform bondply distribution after curing. The fabricated prototypes were not completely planar and exhibited a few degrees of out-of-plane curvature, as shown in Fig. 5.3(b). In some cases, misalignment between the bonded laminates was up to 1 mm. These issues were likely caused by the custom clamping arrangement, which could neither guarantee uniform pressure distribution nor verify that the manufacturer's recommended curing pressure had been achieved.

Since all subarrays were designed to be geometrically identical and fabricated using the same process, their electromagnetic characteristics, $|S_{11}|$ responses versus frequency and radiation patterns, are expected to be similar. However, fabrication tolerances and variations in bonding and layer alignment may have introduced unit-to-unit variation, altering the fabricated antennas' electrical properties. In the intended fabrication process, eight subarrays and one eight-subarray planar-array antennas were to be fabricated for the MIMO radar. However, fabrication difficulties resulted in a high prototype rejection rate, making additional antenna production prohibitively costly. Consequently, only three antennas were successfully fabricated and experimentally measured. Measuring multiple identical antennas provides an assessment of fabrication repeatability, since they all share the same geometry and substrate. For the anechoic chamber, only Antennas 1 and 2 were tested.

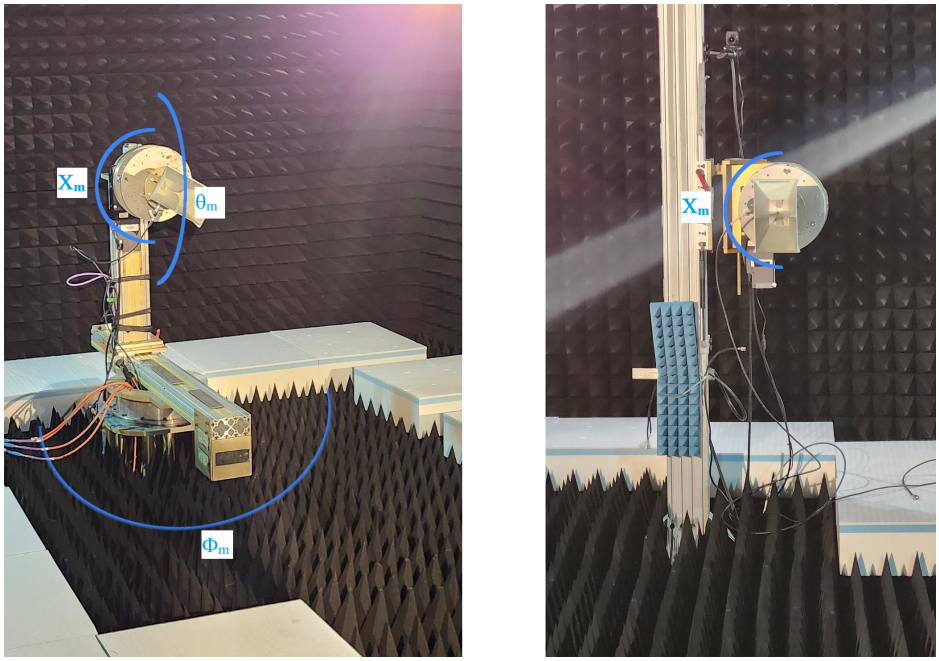
5.2 Experimental Set-up

The $|S_{11}|$ of the antennas was measured using an Agilent N5244A PNA-X Performance Network Analyzer (PNA). The PNA was electronically calibrated across the $5-6$ GHz frequency range. Afterward, the $|S_{11}|$ measurements for all three fabricated antennas were taken in the calibrated frequency range, with a precision of 0.001 Hz. Those measurement results were then incorporated with the ANSYS HFSS simulation results in Microsoft Excel.

The anechoic chamber was calibrated using a pair of standard gain horns (SGHs) covering the frequency range from 1 to 18 GHz, together with the gain-transfer method [40]. The Antenna under Test (AUT) positioner measurement system uses the mechanical coordinate system as shown in Fig. 5.4(a), consisting of the azimuth axis ϕ_m, the elevation axis θ_m, and the polarization roll axis χ_m. The subscript $_m$ denotes the mechanical positioner coordinates and is used to distinguish them from the corresponding angles used to describe the radiation pattern. The source positioner measurement system is shown in Fig. 5.4(b) and consists of the polarization roll axis χ_m.

After the SGHs were installed, the SGH on the AUT positioner was mechanically aligned with respect to the mechanical elevation axis $\theta_m = 0°$, the polarization roll axis $\chi_m = 0°$, and the SGH on the source positioner can only be rotated along the polarization roll axis and was also levelled to $\chi_m = 0°$. Both horns were then boresight-aligned by physically adjusting them until their electrical boresights coincided, corresponding to the reference direction $\phi_m = 0°$. This ensured that the radiation pattern was centered at the origin of the coordinate system. Next, the received power between the SGHs at 5.75 GHz was measured, and a normalization factor was obtained by subtracting the SGHs' calibrated gain from the measured value. Since both SGHs use the same measurement path, this normalization factor accounts for unknown factors in the RF path such as cable losses, free-space path loss, and reflections.

The antenna under test (AUT) was then used to replace one of the SGHs. Using a MATLAB function, the AUT was mechanically aligned to $\theta_m = 0°$ and $\chi_m = 0°$ to maintain co-polarization with the source SGH. The AUT was rotated about the mechanical azimuth axis over the range $-90° \leq \phi_m \leq 90°$, while the co-polarized E-plane radiation pattern was recorded in MATLAB. To measure the co-polarization H-plane radiation pattern, the polarization roll of both antennas was rotated 90°, and the same azimuth sweep was repeated. For cross-polarization E-plane measurements, only the AUT was rotated 90° about its polarization roll axis, and the azimuth sweep was repeated. To measure the H-plane cross-polarization radiation pattern, both antennas were subsequently



(a) (b)

Figure 5.4: AUT and source positioners' coordinates

rotated by 90° about their polarization roll axis, and the azimuth sweep was repeated. Finally, the normalization factor was applied to the measured data to obtain the AUT's absolute gain for the plane radiation pattern cuts. The measured data was transferred into Excel and MATLAB to apply the normalization factor and draw the polar radiation patterns, respectively.

5.3 Measurement Results and Discussion

The $|S_{11}|$ responses versus frequency for all three fabricated subarray TX antennas are shown in Fig. 5.5. Overall, the measured $|S_{11}|$ response of Antenna 1 exhibits excellent agreement with the simulated results across the frequency band of interest. Antennas 2 and 3 show larger deviations from the simulated response; however, their measured performance remains within the specified design requirements. Furthermore, all subarrays achieve reflection coefficient minima below -18 dB at resonance, indicating excellent impedance matching and low reflected power.

Table 5.1 summarizes $|S_{11}|$ design requirements, measured and simulated

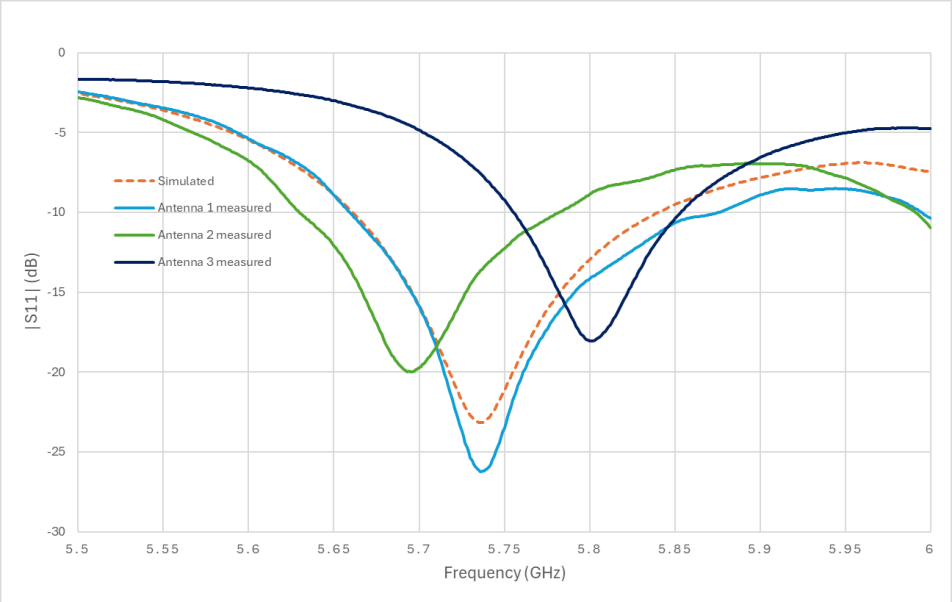


Figure 5.5: Simulated and measured $|S_{11}|$ of the subarrays

values across the frequency range, impedance BW, and operational frequency. Antenna 1 achieves a BW of 215 MHz, while Antenna 2 exhibits an increased BW of 361 MHz and Antenna 3, a reduced BW of 97 MHz. All three prototypes, Antennas 1, 2, and 3, exhibit resonance close to the intended operating frequency of 5.75 GHz, at 5.736 GHz, 5.695 GHz, and 5.801 GHz, respectively. These results demonstrate the improved subarray antenna design's suitability for MIMO radar applications, where adequate impedance bandwidth and consistent element performance are required to support reliable array operation. Consequently, Antenna 1 most closely represents the intended design objective, while Antenna 2 and Antenna 3 illustrate the effect of fabrication variability. During manufacturing, tolerances and assembly variations were introduced, as discussed in Section 5.1. This may have contributed to deviations in the measured impedance bandwidth and resonant frequency from the simulated results.

The radiation characteristics of the fabricated antennas were experimentally evaluated through E-plane and H-plane pattern measurements in the anechoic chamber. Only the forward radiation pattern, $-90°$ to $90°$, can be measured in the anechoic chamber. The measured co-polarized radiation patterns are presented in Fig. 5.6 and Fig. 5.7 for Antennas 1 and 2, respectively.

Table 5.1: Comparison of simulated, measured antennas and design requirements

Antenna Case	**Frequency Range (GHz)**	**BW (MHz)**	**FBW (%)**	f_0 **(GHz)**
Design Spec.	$5.65 - 5.85$	≈ 200	3.5	5.75
Simulated	$5.66 - 5.84$	180	3.14	5.736
1 Measured	$5.66 - 5.875$	215	3.75	5.736
2 Measured	$5.63 - 5.991$	361	6.34	5.695
3 Measured	$5.756 - 5.853$	97	1.67	5.801

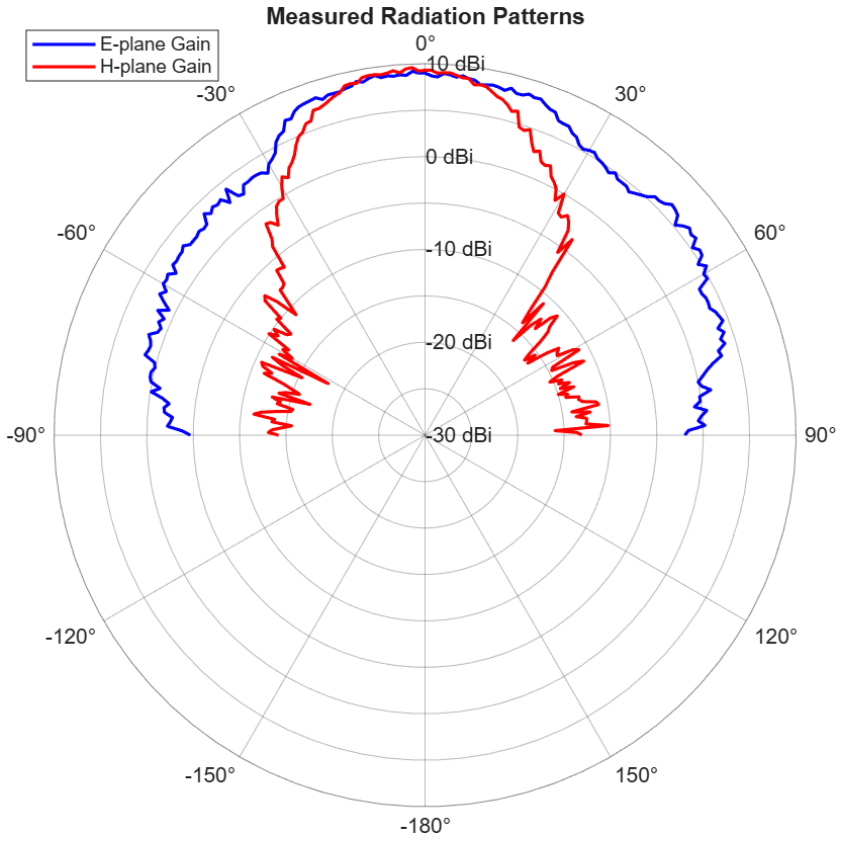


Figure 5.6: Measured co-polarization of antenna 1

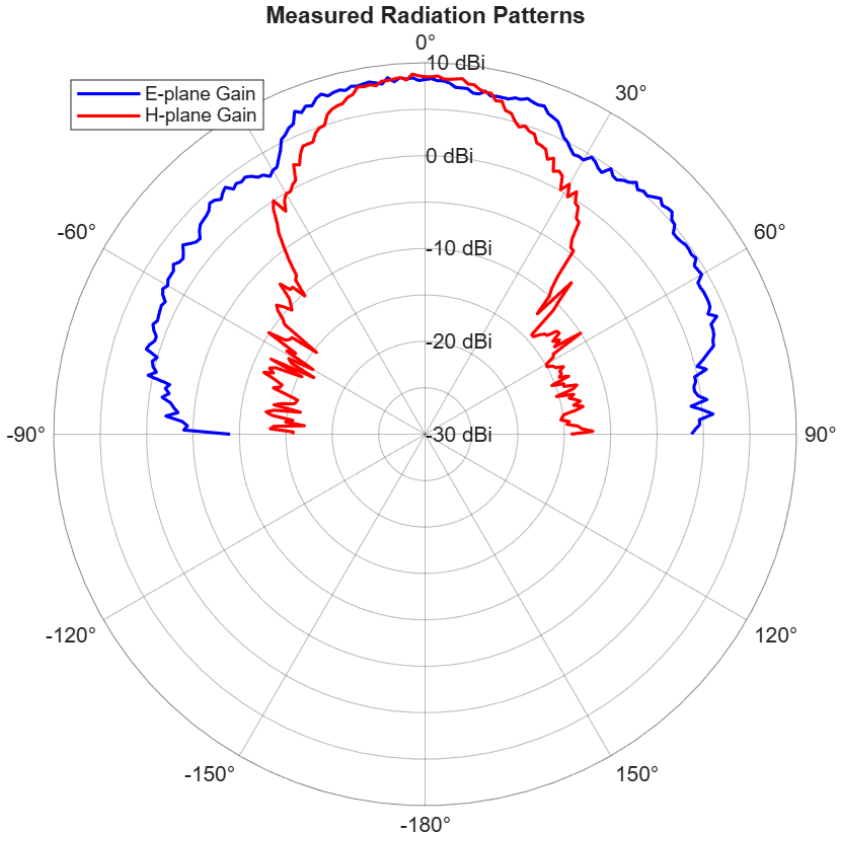


Figure 5.7: Measured co-polarization of antenna 2

Both fabricated antennas exhibit a broad azimuthal response and a more directive elevation response, consistent with the intended coverage for the radar application as specified in Section 2.6.1. Furthermore, the measured polar patterns also show noticeable ripples of ≈ -1 to -2 dB in both planes throughout the measured patterns. Although deviations of approximately -5 dB from the simulated pattern are observed near $\pm 30°$, no distinct sidelobe is identified, as these variations are not separated from the main beam by a well-defined null. These variations indicate additional radiation in undesired directions and likely result from a combination of edge diffraction (finite-ground plane and finite-substrate effects), fringing field effects, and imperfections in the fabricated antennas. Such effects can modify the current distribution and allow electromagnetic fields to radiate from regions outside the intended aperture. Despite these ripples, both fabricated antennas maintain the required broad

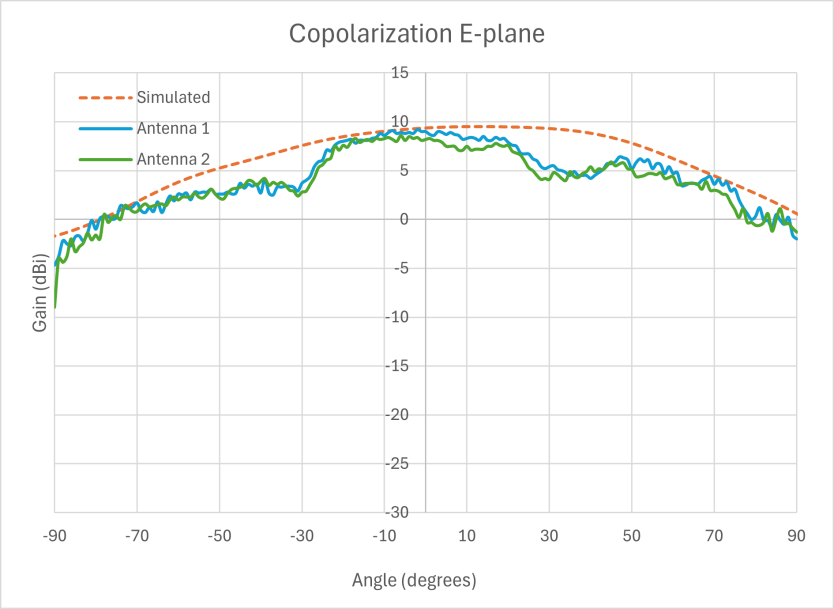


Figure 5.8: Simulated vs Measured co-polarization E-plane

azimuth coverage and narrower elevation response. Attempts to reproduce the observed edge-diffraction effects in the simulated radiation patterns did not yield comparable results.

The simulated and measured co-polarized radiation patterns are presented in Cartesian coordinates in Fig. 5.8 and Fig. 5.9 for the E-plane and H-plane, respectively. These plots compare the simulated antenna with the two fabricated antennas, making differences in beamwidth and sidelobe behaviour easier to identify. The measured E-plane and H-plane beamwidths are similar for Antennas 1 and 2, indicating good consistency between the two fabricated samples. However, the simulated antenna exhibits a broader coverage than the two measured antennas.

Table 5.2 compares the measured antenna characteristics with the design objectives and the simulated performance. The measured peak radiation directions are slightly offset from $\theta = 0°$. For Antenna 1, the peak gain is 9.2 dBi at an angle of $\theta = -2°$ and 9.6 dBi at an angle of $\theta = -2°$ in the E-plane and H-plane, respectively. For Antenna 2, the peak gain is 8.6 dBi at an angle of $\theta = -6°$ and 8.8 dBi at $\theta = -2°$ in the E-plane and H-plane, respectively. Antenna 1's measured gain is similar to the simulated values; however, antenna 2 has the lowest gain. The small peak angular offsets primarily result from

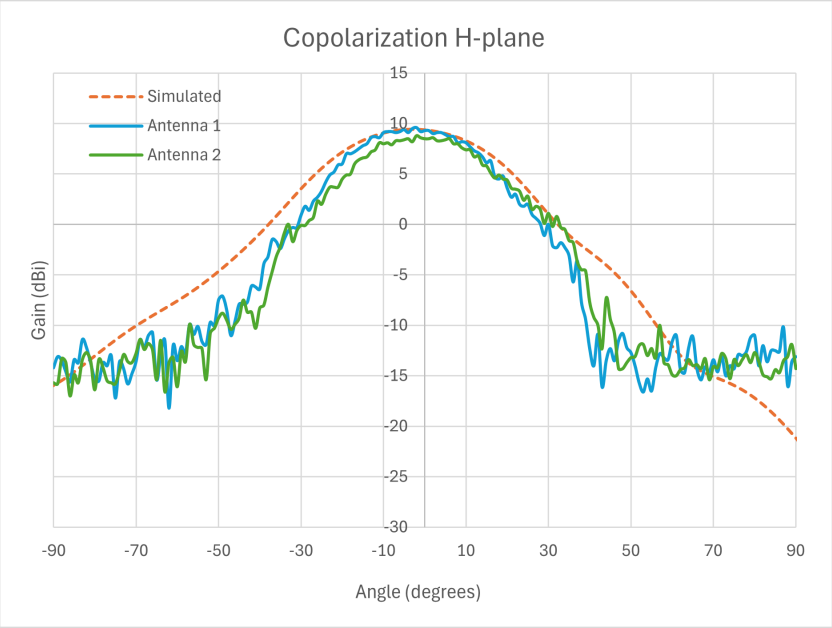


Figure 5.9: Simulated vs Measured co-polarization H-plane

measurement alignment tolerances and fabrication variations. They do not significantly affect the overall radiation characteristics or the radar antenna's intended field of view.

The Antenna 1's $HPBWs$ are approximately 50.9° and 33.6° for the E-plane and H-plane, respectively. The Antenna 2's $HPBWs$ are approximately 49.6° and 32.2° for the E-plane and H-plane, respectively. The measured E-plane $HPBWs$ of Antennas 1 and 2 are approximately 50% smaller than the corresponding simulated values, indicating a narrower azimuthal region than predicted. Nevertheless, the measured radiation patterns maintain significant forward radiation over the same angular range as the simulation. Overall, the close agreement between Antennas 1 and 2 demonstrates good fabrication repeatability. Both samples provide comparable peak gain, azimuth and elevation beamwidth, and overall radiation characteristics. However, the ripples in the radiation pattern need to be removed. Further improvements to the substrate and ground-plane size could smooth the radiation pattern and remove the edge diffraction. The fabricated antennas successfully maintain the required directional characteristics for integration into the MIMO radar system.

Several practical effects can account for the difference between the simulated

Table 5.2: Comparison of the design specifications, simulated results, and measured radiation characteristics of the fabricated antennas.

Parameter	Design Spec.	Simulated	Antenna 1 Measured	Antenna 2 Measured
Peak Gain (dBi)				
E-plane	–	9.5	9.2	8.6
H-plane	–	9.4	9.6	8.8
Peak Angle (°)				
E-plane	–	13	-2	-6
H-plane	–	-3	-2	-2
$HPBW$ (°)				
E-plane	–	≈ 97.4	≈ 50.9	≈ 49.6
H-plane	–	≈ 40	≈ 33.6	≈ 32.2
Sidelobes (dB)				
E-plane	≤ -15	None	None, but showing edge diffraction	None, but showing edge diffraction
H-plane	≤ -15	None	None, but showing edge diffraction	None, but showing edge diffraction

and measured $|S_{11}|$ and radiation patterns. Diffraction from the finite ground plane and surface-wave excitation could have contributed to the observed pattern distortion. Rogers RO3003™ substrates and Rogers 2929 bonding layer have tolerances such as thickness and relative permittivity. Also, fabrication tolerances, including small variations in patch dimensions, feed-line geometry, substrate alignment, and bonding-layer thickness, can perturb the current distribution and produce additional ripple. These fabrication issues can introduce tolerance deviations in the linear-branching feed network and patch coupling. This adds small amplitude and phase imbalances and increases mutual coupling between adjacent circular patches, which may further alter element currents and their relative phases.

6 Conclusion

This thesis presented the design, simulation, fabrication, and experimental validation of an improved microstrip antenna array developed for the RMC monostatic MIMO radar operating below 6 GHz. The motivation for this work originated from the limitations of the existing ultra-wideband omnidirectional antennas used by the radar system, which produced excessive back radiation, clutter, and limited control over the radiation coverage required for controlled laboratory radar experiments. The research addressed the need for an antenna solution tailored to the electromagnetic and radar-processing requirements of the existing laboratory platform. The objective was therefore to develop an improved subarray capable of providing directional radiation characteristics, 200 MHz impedance bandwidth, low sidelobe levels, low back radiation, and dimensions suitable for integration into a MIMO radar array operating within the $5.25 - 5.925$ GHz radar band.

A proximity-coupled series-fed network and a circular patch were selected from the literature review, combined and improved through systematic parametric studies to satisfy the targeted design requirements. The subarray successfully achieved a simulated resonance frequency of 5.736 GHz and an impedance bandwidth of 180 MHz while meeting the requirement of broad azimuth coverage with an $HPBW$ of 97.4°, a narrower elevation beam with an $HPBW$ of 40°, F/B ratios of 14 dB, and no distinct sidelobes in either principal plane. This subarray was subsequently fabricated and experimentally characterized. The measured results agreed well with the simulated results. The measured antenna 1 produced a f_0 of 5.736 GHz with a BW of 215 MHz, peak gains of 9.2 dBi and 9.6 dBi in the E-plane and the H-plane, respectively. $HPBWs$ were approximately 50.9° in the E-plane and 33.6° in the H-plane. Due to the experimental set-up, the back radiation could not be measured. The measured results demonstrated good agreement with the simulations despite fabrication tolerances and bonding imperfections. However, ripples and distortions were observed in the measured radiation patterns, which are believed to be caused primarily by edge-field diffraction from the finite substrate and

ground-plane dimensions. Further adjustment will be required to remove the patterns distortions.

Table 6.1 compares the antennas reviewed in Sections 2.6.2 and 2.6.3 with the improved three-element circular-patch subarray. Although several literature designs achieve superior performance in individual metrics such as bandwidth, gain, front-to-back ratio, or sidelobe level, they often operate outside the target radar band or employ feed architectures that are not compact for 2D planar-array integration. The three-element subarray directly addresses the requirements of the RMC MIMO radar platform by operating at 5.74 GHz while achieving a simulated impedance bandwidth of 180 MHz and a measured bandwidth of 215 MHz. Its proximity-coupled series-fed network with coupling branches combines the compactness of series-fed architectures with the ability to control excitation amplitudes and phases, enabling low-profile integration into a planar MIMO array. Consequently, the principal contribution of the design is not the maximization of a single antenna performance metric, but the achievement of a practical balance between operating frequency, bandwidth, radiation coverage, feed-network simplicity, and array-integration requirements for the intended radar application.

The improved subarray was subsequently integrated into a 2D planar array for the RX antenna design. Parametric studies were performed to investigate the effects of subarray spacing, edge clearance, and substrate dimensions on impedance matching, mutual coupling, and radiation performance. Resonant frequencies remained closely grouped across all eight subarrays at 5.72 GHz with BWs between 164 and 189 MHz, and adjacent-element coupling remaining below -18 dB. When all subarrays are illuminated in-phase at to form a broadside beam, the resulting pattern array achieved simulated peak gains exceeding 17.8 dB, front-to-back ratios greater than 26 dB, and radiation characteristics suitable for MIMO radar operation. The selected element spacing of $\lambda/2$ preserves the full set of 64 unique virtual array elements. The simulated planar array achieved an E-plane forward sidelobe level of approximately -13.1 dB, which closely matches the theoretical first sidelobe level of a uniformly illuminated in-phase array.

Compared with the Taoglas FXUWB20 antenna currently employed by the RMC MIMO radar, the proposed subarray provides approximately 5 dB higher gain, directional radiation characteristics, improved front-to-back ratio, and operation at the desired 5.75 GHz center frequency without the limitations imposed by the Taoglas 5.8 GHz rejection band. These improvements are achieved at the expense of a modest reduction in impedance bandwidth relative to the radar's full 200 MHz channel. Overall, this work establishes a design methodology that connects antenna-level electromagnetic requirements with

array-level and radar-processing considerations. It further demonstrates how antenna bandwidth, radiation characteristics, mutual coupling, and physical dimensions can be improved while simultaneously satisfying practical radar-system requirements. This approach is particularly relevant for MIMO radar systems, where antenna characteristics such as radiation pattern, impedance bandwidth, element spacing, and mutual coupling directly influence the quality of the resulting array response and radar measurements. Future work could focus on the following:

- Identify the source of the measured radiation pattern distortion in the fabricated subarrays and investigate ways to remove it.
- Investigate ways of reducing the back radiation of the subarray antenna while maintaining the desired azimuth and elevation coverage.
- Investigate and simulate the use of absorbing materials or other hardware solutions behind the antennas to reduce back radiation.
- Perform a tolerance sensitivity analysis on the subarray to identify which parameters most influence resonant frequency and bandwidth.
- Export the simulated radiation patterns and S-parameters into MATLAB to simulate a complete MIMO radar system to assess target detection, angular resolution, and spatial ambiguity.
- Future validation should include fabricating and measuring the 2D planar array and integrating it into the RMC radar platform.
- Experimental radar testing, using the UWB Taoglas and improved antennas, could then quantify improvements in clutter suppression, angular discrimination, target detection performance, and virtual-array beamforming capability.

Table 6.1: Comparison of the Subarray with Antenna Designs from the literature

Antenna Design	f_0 **(GHz)**	BW **(MHz)**	**Radiation Pattern**	**Integration Considerations**
Circular MPA with fan-shaped cells [19]	4.0	125	Directional; broad forward coverage	Probe location needs to change to allow feed network
Circular patch with directional pattern [20]	28.6	2100	Broadside radiation;	Requires redesign for $f_0 = 5.75$ Ghz
Rectangular MPA [21]	10.1	453	$HPBW \approx 74^\circ$ SLL $= -16.3$ dB	Microstrip feed
Circular MPA [21]	10.2	488	$HPBW = 75.8^\circ$ SLL $= -18.4$ dB	Footprint of $0.33\lambda \times 0.35\lambda$; conventional Microstrip feed
Series-fed array with patch-width tapering [23]	62	6000	Radiation pattern not reported	Series-fed; width tapering
Matching-in-step series-fed array [25]	5	140	Low-sidelobe level	Stepped feed-width tapering
Series-fed array with coupling branches [14]	26	4000	Low-sidelobe level	Coupling branches; phase/amplitude control
Comb-line array [26]	24	> 250	Directional; tapered excitation	Narrow feed network
Corporate-fed array [29]	8.22	1200	Wideband array	Large divider network
Improved 3-element subarray, simulated results	5.74	180	E-plane $HPBW = 97.4^\circ$ H-plane $HPBW = 40^\circ$ F/B ratio = 14 dB	Series-fed coupling branches;

Bibliography

[1] Muhammad Umar et al. "Possibilities and Challenges for a Phased Array Antenna System in ISAC: A Hardware Perspective". In: *IEEE Access* 13 (2025), pp. 146032–146051. ISSN: 2169-3536. DOI: 10.1109/ACCESS.2025.3599680.

[2] Muhammad Imran Nawaz et al. "A Review on Wideband Microstrip Patch Antenna Design Techniques". In: *2013 International Conference on Aerospace Science & Engineering (ICASE)*. Islamabad, Pakistan, 2013, pp. 1–8. DOI: 10.1109/ICASE.2013.6785554.

[3] M. A. Matin, B. S. Sharif, and C. C. Tsimenidis. "Probe Fed Stacked Patch Antenna for Wideband Applications". In: *IEEE Transactions on Antennas and Propagation* 55.8 (Aug. 2007), pp. 2385–2388. ISSN: 1558-2221. DOI: 10.1109/TAP.2007.901924.

[4] Mohammad S. Sharawi. *Printed Mimo Antenna Engineering*. Boston: Artech house, 2014. ISBN: 978-1-60807-681-9.

[5] Constantine A Balanis. *Antenna Theory Analysis and Design*. 4th ed. Hoboken, New Jersey: John Wiley & Sons, Inc., 2016. ISBN: 978-1-118-64206-1.

[6] Robert Gilpin. "Real-Time Multiple Input Multiple Output (MIMO) Radar Using Software Defined Radio". MASc thesis. Kingston, ON: Division of Graduate Studies, Royal Military College of Canada, 2021.

[7] Taoglas. *Taoglas AccuraUWB Datasheet*. Nov. 14, 2023. URL: www.taoglas.com/product/fxuwb20-07-35-610ghz-ultra-wideband-uwb-flex-antenna-100mm-1-37mm-ipex-mhfht/.

[8] Segun Akinola, Iddi Hashimu, and Ghanshyam Singh. "Gain and Bandwidth Enhancement Techniques of Microstrip Antenna: A Technical Review". In: *2019 International Conference on Computational Intelligence and Knowledge Economy (ICCIKE)*. 2019 International Conference

on Computational Intelligence and Knowledge Economy (ICCIKE). Dec. 2019, pp. 175–180. DOI: 10.1109/ICCIKE47802.2019.9004278.

[9] Srijita Chakraborty et al. "Frequency Tuning Characteristics & Bandwidth Enhancement for Circular Microstrip Antenna by Integrating L-Shaped DGS". In: *2020 IEEE International IOT, Electronics and Mechatronics Conference (IEMTRONICS)*. 2020 IEEE International IOT, Electronics and Mechatronics Conference (IEMTRONICS). Sept. 2020, pp. 1–7. DOI: 10.1109/IEMTRONICS51293.2020.9216423.

[10] Institute of Electrical and Electronics Engineers. *IEEE Standard for Definitions of Terms for Antennas*. New York, NY, USA, Mar. 6, 2014. DOI: 10.1109/IEEESTD.2014.6758443.

[11] George W. Stimson et al. *Introduction to Airborne Radar*. 3rd ed. Raleigh: SciTech publ, 2014. ISBN: 978-1-61353-022-1.

[12] Muhammad Umar Khan, Mohammad Said Sharawi, and Raj Mittra. "Microstrip Patch Antenna Miniaturisation Techniques: A Review". In: *IET Microwaves, Antennas & Propagation* 9.9 (2015), pp. 913–922. ISSN: 1751-8733. DOI: 10.1049/iet-map.2014.0602. URL: https://onlinelibrary.wiley.com/doi/abs/10.1049/iet-map.2014.0602 (visited on 05/29/2026).

[13] Hattan F. Abutarboush et al. "A Reconfigurable Wideband and Multiband Antenna Using Dual-Patch Elements for Compact Wireless Devices". In: *IEEE Transactions on Antennas and Propagation* 60.1 (Jan. 2012), pp. 36–43. ISSN: 1558-2221. DOI: 10.1109/TAP.2011.2167925.

[14] E. A. Soliman et al. "Series-Fed Microstrip Antenna Arrays Operating at 26 GHz". In: *2010 IEEE Antennas and Propagation Society International Symposium*. 2010 IEEE Antennas and Propagation Society International Symposium. July 2010, pp. 1–4. DOI: 10.1109/APS.2010.5561286.

[15] Eric Pitre. "MIMO Radar Hardware Acceleration with Enhanced Resolution". MASc thesis. Kingston, ON: Division of Graduate Studies, Royal Military College of Canada, 2022.

[16] Jamie Bergin and J. R. Guerci. *MIMO Radar: Theory and Application*. Boston: Artech House, 2018. 229 pp. ISBN: 978-1-63081-342-0.

[17] Merrill Ivan Skolnik. *Radar Handbook*. 3rd ed. New York: McGraw-Hill, 2008. ISBN: 978-0-07-148547-0.

[18] Innovation Government of Canada. *Canadian Table of Frequency Allocations (2022)*. Apr. 30, 2014. URL: https://ised-isde.canada.ca/site/spectrum-management-telecommunications/en/learn-more/key-documents/consultations/canadian-table-frequency-allocations-sf10759 (visited on 07/07/2025).

[19] W. D. Ma et al. "Compact Microstrip Antenna with Pattern-Reconfigurable Characteristic". In: *Radioengineering* 26.3 (Sept. 15, 2017), 662–667. ISSN: 1210-2512. DOI: 10.13164/re.2017.0662.

[20] Nabila Sultana Anonnya and Md. Mostafizur Rahman. "A Proposed Microstrip Patch Antenna Design For 5G Applications". In: *2022 13th International Conference on Computing Communication and Networking Technologies (ICCCNT)*. Oct. 2022, pp. 1–6. DOI: 10.1109/ICCCNT54827.2022.9984217.

[21] Tahsin Ferdous Ara Nayna, A. K. M. Baki, and Feroz Ahmed. "Comparative Study of Rectangular and Circular Microstrip Patch Antennas in X Band". In: *2014 International Conference on Electrical Engineering and Information & Communication Technology*. 2014 International Conference on Electrical Engineering and Information & Communication Technology. Apr. 2014, pp. 1–5. DOI: 10.1109/ICEEICT.2014.6919142.

[22] Hao Yi et al. "Traveling-Wave Series-Fed Patch Array Antenna Using Novel Reflection-Canceling Elements for Flexible Beam". In: *IEEE Access* 7 (2019), pp. 111466–111476. ISSN: 2169-3536. DOI: 10.1109/ACCESS.2019.2934652.

[23] Yi-Jie Ye et al. "A Series-Fed Patch Antenna Array for Biomedical Radar Applications". In: *2021 International Symposium on Antennas and Propagation (ISAP)*. 2021 International Symposium on Antennas and Propagation (ISAP). Oct. 2021, pp. 1–2. DOI: 10.23919/ISAP47258.2021.9614542.

[24] R. Priya et al. "Integrated Design Framework for Scalable Series-Fed Microstrip Patch Antenna Arrays With Machine Learning Assistance". In: *IEEE Access* 14 (2026), pp. 48478–48486. ISSN: 2169-3536. DOI: 10.1109/ACCESS.2026.3678079.

[25] Tao Yuan, Ning Yuan, and Le-Wei Li. "A Novel Series-Fed Taper Antenna Array Design". In: *IEEE Antennas and Wireless Propagation Letters* 7 (2008), pp. 362–365. ISSN: 1548-5757. DOI: 10.1109/LAWP.2008.928487.

[26] Jiawei Qian et al. “A 24 GHz Microstrip Comb Array Antenna With High Sidelobe Suppression for Radar Sensor”. In: *IEEE Antennas and Wireless Propagation Letters* 20.7 (July 2021), pp. 1220–1224. ISSN: 1548-5757. DOI: 10.1109/LAWP.2021.3075887.

[27] Ajith Kumar D et al. “Design of a Two Element Microstrip Antenna with Improved Bandwidth for Wireless Applications”. In: *2025 3rd International Conference on Advancements in Electrical, Electronics, Communication, Computing and Automation (ICAECA)*. 2025 3rd International Conference on Advancements in Electrical, Electronics, Communication, Computing and Automation (ICAECA). Apr. 2025, pp. 1–6. DOI: 10.1109/ICAECA63854.2025.11012443.

[28] Ajith Kumar D et al. “Design of a Four Element Microstrip Patch Array Antenna with Improved Bandwidth for Medical Applications”. In: *2025 3rd International Conference on Advancements in Electrical, Electronics, Communication, Computing and Automation (ICAECA)*. 2025 3rd International Conference on Advancements in Electrical, Electronics, Communication, Computing and Automation (ICAECA). Apr. 2025, pp. 1–6. DOI: 10.1109/ICAECA63854.2025.11012489.

[29] Tannmay Gupta. “Bandwidth Enhancement of MIMO Array Antenna Using Novel Four Element Array Configuration”. In: *2023 International Conference on Power Energy, Environment & Intelligent Control (PEEIC)*. 2023 International Conference on Power Energy, Environment & Intelligent Control (PEEIC). Dec. 2023, pp. 110–115. DOI: 10.1109/PEEIC59336.2023.10451946.

[30] John Leonidas Volakis, ed. *Antenna Engineering Handbook*. 4th ed. New York: McGraw-Hill, 2007. 1755 pp. ISBN: 978-0-07-147574-7.

[31] Rogers Coorpration. *RO3000® Series Circuit Materials*. URL: https://www.rogerscorp.com/advanced-electronics-solutions/ro3000-series-laminates/ro3003-laminates (visited on 08/03/2026).

[32] Rogers Coorpration. *2929 Bondply Data Sheet*. URL: www.rogerscorp.com/advanced-electronics-solutions/2929-bondply (visited on 08/03/2026).

[33] Sourabh Bisht et al. “Study the Various Feeding Techniques of Microstrip Antenna Using Design and Simulation Using CST Microwave Studio.” In: 2014. URL: https://api.semanticscholar.org/CorpusID:16064132.

[34] Muhammad Riza Darmawan et al. "Development A Microstrip Antenna Array with 8 Elements and Dolph-Chebyshev Distribution for Capturing Signals from the Himawari-8 Satellite". In: *2024 IEEE 2nd International Conference on Electrical Engineering, Computer and Information Technology (ICEECIT)*. 2024 IEEE 2nd International Conference on Electrical Engineering, Computer and Information Technology (ICEECIT). Nov. 2024, pp. 141–146. DOI: 10.1109/ICEECIT63698.2024.10860221.

[35] K. Priethamje Vithya and L.M. Varalakshmi. "Amplitude Excitation Analysis of Uniform and Non-Uniform Structured Microstrip Patch Antenna for High Frequency ISM Band at 24 GHz for Surveillance Applications". In: *2024 First International Conference on Innovations in Communications, Electrical and Computer Engineering (ICICEC)*. 2024 First International Conference on Innovations in Communications, Electrical and Computer Engineering (ICICEC). Oct. 2024, pp. 1–5. DOI: 10.1109/ICICEC62498.2024.10808297.

[36] Muhammad Riza Darmawan and Catur Apriono. "A 4x4 Microstrip Feeder Antenna Design Using Dolph-Chebyshev for Receiving Himawari-8 Satellite Data". In: *2022 IEEE International Conference on Communication, Networks and Satellite (COMNETSAT)*. 2022 IEEE International Conference on Communication, Networks and Satellite (COMNETSAT). Nov. 2022, pp. 270–276. DOI: 10.1109/COMNETSAT56033.2022.9994393.

[37] Nurul Fahmi Arief Hakim et al. "Microstrip Array Antenna Using Proximity Coupled and Dolph Chebyshev Distribution for Wi-Fi 6E". In: *2024 10th International Conference on Wireless and Telematics (ICWT)*. 2024 10th International Conference on Wireless and Telematics (ICWT). July 2024, pp. 1–5. DOI: 10.1109/ICWT62080.2024.10674729.

[38] *Chebwin - Chebyshev Window - MATLAB*. URL: www.mathworks.com/help/signal/ref/chebwin.html (visited on 05/15/2026).

[39] Rogers Coorpration. *2929 Bondply Multi-Layer Board Processing Guidelines*. URL: www.rogerscorp.com/advanced-electronics-solutions/2929-bondply (visited on 08/03/2026).

[40] Institute of Electrical and Electronics Engineers. *IEEE Recommended Practice for Antenna Measurements*. Version IEEE Std 149-2021 (Revision of IEEE Std 149-1977). New York, NY, USA, Feb. 2022. DOI: 10.1109/IEEESTD.2022.9714428.

Appendices

A Matlab Code for Virtual Array Beam Pattern and HPBW Calculation

The following MATLAB script was used to compute the virtual array position, plot the beam pattern and calculate the $HPBW$ of the virtual array:

```
clear; clc;
% Input Parameters
n_tx = 8; d_tx = 4;     % No of Transmitters and Spacing
n_rx = 8; d_rx_cases = [0.5 0.8];  % No of Receivers and
    Spacing

HPBW_all = zeros(size(d_rx_cases)); %Store HPBW for All
    Config
figure; hold on; grid on;

for config = 1:length(d_rx_cases)
    d_rx = d_rx_cases(config);

    % Angle grid 30 degrees around broadside
    theta = linspace(-30,30,36001);  % High resolution

    % TX Array Factor
    denum_AF_tx = n_tx*sin(pi*d_tx*sind(theta));
    AF_tx = (sin(n_tx*pi*d_tx*sind(theta))) ./ denum_AF_tx
        ;

    % RX Array Factor
    denum_AF_rx = n_rx*sin(pi*d_rx*sind(theta));
    AF_rx = sin(n_rx*pi*d_rx*sind(theta)) ./ denum_AF_rx;

    % Replace NaN (0/0) With 1
```

```
    AF_tx(abs(denum_AF_tx) < 1e-12) = 1;
    AF_rx(abs(denum_AF_rx) < 1e-12) = 1;

    % Create the Virtual Array Factor
    AFv = abs(AF_tx .* AF_rx);
    AFv = AFv/max(AFv); % Normalize the Array Factor
    AFv_dB = 20*log10(AFv); % Convert From Linear
        Amplitude to dB

    %% HPBW Calculation
    hp_level = 1/sqrt(2);       % -3 dB Amplitude Point
    idx = find(AFv >= hp_level);

    % Left and Right Edge Interpolations
    left_idx  = idx(1);
    right_idx = idx(end);
    theta_left  = theta(left_idx);
    theta_right = theta(right_idx);

    HPBW_deg = theta_right - theta_left;
    HPBW_all(config) = HPBW_deg;

    %% First Sidelobe Level and Angle
    [peaks,angles] = findpeaks(AFv_dB, theta);

    % Separate peaks on right side of broadside
    right_idx = find(angles > 0);
    peaks_right = peaks(right_idx);
    angles_right = angles(right_idx);

    % First sidelobe on the right: closest peak to 0
        degrees
    if length(right_idx)>= 2
        SLL_p_right = peaks_right(1);
        SLL_a_right = angles_right(1);
    else
        SLL_p_right = NaN;
        SLL_a_right = NaN;
    end

    %% Highest Sidelobe Level and Angle
    % Sort peaks and angles in descending order of
        amplitude
    [peaks_descending, sort_idx] = sort(peaks,'descend');
    angles_descending = angles(sort_idx);
```

```
66
67      if length(peaks_descending) >= 2 % 2nd peak is highest
            SLL
68          SLL_High_p = peaks_descending(2);
69          SLL_High_a = angles_descending(2);
70      else
71          SLL_High_p = NaN;
72          SLL_High_a = NaN;
73      end
74
75
76      %% Number of virtual elements
77      %Physical positions
78      tx_pos = (0:n_tx-1)*d_tx;
79      rx_pos = (0:n_rx-1)*d_rx;
80
81      % Virtual antenna positions
82      virtual_array = tx_pos(:) + rx_pos;
83
84      % Unique virtual antenna positions
85      unique_virtual_array = unique(round(virtual_array(:),
            10));
86
87
88      %% Display Results
89      fprintf('\n====================================\n');
90      fprintf('d_tx = %d lambda\n',d_tx);
91      fprintf('d_rx = %.1f lambda\n',d_rx);
92      fprintf('Virtual channels = %d\n',length(virtual_array
            (:)));
93      fprintf('Unique positions = %d\n',length(
            unique_virtual_array));
94      fprintf('HPBW = %.4f deg\n',HPBW_deg);
95      fprintf('First SLL peak = %.2f dB\n',SLL_p_right);
96      fprintf('First SLL angle = %.4f degrees\n',
            SLL_a_right);
97      fprintf('Highest SLL peak = %.2f dB\n',SLL_High_p);
98      fprintf('Highest SLL angle = %.4f degrees\n',
            SLL_High_a);
99
100
101     %% Plot broadside beam pattern
102     if config == 2
103         lineStyle = '--';    % Dashed line for the second
                configuration
```

```
104     else
105         lineStyle = '-';    % Solid line for the first
                configuration
106     end
107
108     plot(theta, AFv_dB, lineStyle, 'LineWidth', 1,'
            DisplayName', ...
109         sprintf('d_{rx}=%.1f\\lambda, %d unique positions'
                ,d_rx,length(unique_virtual_array)));
110
111     title('Beam Pattern (Broadside Steering)');
112     xlabel('Angle (degrees)'); ylabel('Normalized array
            factor (dB)');
113     ylim([-60 0]); legend('Location','best');
114 end
```

Listing A.1: Beam Pattern and $HPBW$ Calculation in MATLAB